Title

Uncertainty quantification in vibration-based structural health monitoring for enhanced decision-making capability

Author

Mao, Zhu

Publication Date

2012

UNIVERSITY OF CALIFORNIA, SAN DIEGO

Uncertainty Quantification in Vibration-Based Structural Health Monitoring for Enhanced Decision-Making Capability

A dissertation submitted in partial satisfaction of the requirements for the degree Doctor of Philosophy

in

Structural Engineering

by

Zhu Mao

Committee in charge:

Professor Michael D. Todd, Chair
Professor Joel P. Conte
Professor Charles R. Farrar
Professor Rajesh K. Gupta
Professor William S. Hodgkiss

2012

The Dissertation of Zhu Mao is approved, and it is acceptable in quality and form for publication on microfilm:

Chair

University of California, San Diego
2012

DEDICATION

To my dearest wife and upcoming daughter.

TABLE OF CONTENTS

LIST OF ABBREVIATIONS

AUC	Area Under Curve
DPD	Dot Product Difference
FE	Finite Element
FFT	Fast Fourier Transform
FRF	Frequency Response Function
IP	Interest Point
MIMO	Multiple-Input/Multiple-Output
NSR	Noise-to-Signal
OP	Outlier Percentage
PDF	Probability Density Function
RMSD	Root-Mean-Square Distance
RMSE	Root-Mean-Square Error
ROC	Receiver Operating Characteristics
SHM/DP	Structural Health Monitoring/Damage Prognosis
SIMO	Single-Input/Multiple-Output
SISO	Single-Input/Single-Output
SNR	Signal-to-Noise
UQ	Uncertainty Quantification

LIST OF SYMBOLS

$u(t)$ and $v(t)$	ideal input and output time series
$m(t)$ and $n(t)$	noise on input and output side
$x(t)$ and $y(t)$	contaminated measurements
$\mathcal{F}$	Fourier Transform operator
$\tilde{\ }$	raw estimation of quantity
$\hat{\ }$	smooth estimation of quantity
*	complex conjugate
γ_{xy}^{2}	coherence function between x and y
ω	radial frequency
Ω	natural frequency
G	power density spectrum
H	frequency response function (FRF)
T	transmissibility
$\lvert\ \rvert$	magnitude
$\measuredangle$	phase
$\mathcal{N}$	normal distribution
$\mathbf{J}$	Jacobian determinant
n_d	number of average
n_t	number of trials in Monte-Carlo test
ρ	correlation coefficient
ε	normalized error

$p_{\lvert\hat{H}\rvert}$, $p_{\lvert\hat{T}\rvert}$	probability density function of H and T magnitude via Gaussian bivariate approach
p_t	probability density function of T magnitude via Chi-square bivariate approach
$p_{\measuredangle\hat{H}}$, $p_{\measuredangle\hat{T}}$	probability density function of H and T phase via Gaussian bivariate approach
$\overline{pct}$	average outlier percentage
Λ_u, Λ_d	probability parameters for undamaged and damaged data set
$\mathcal{H}_0, \mathcal{H}_1$	null and alternative hypothesis
P_{D}	probability of detection
P_{FA}	probability of false alarm
α	significance level

LIST OF FIGURES

LIST OF TABLES

ACKNOWLEDGEMENTS

I always feel lucky of coming to UCSD, pursuing my M.S. and Ph.D. degrees in the past six years, and this dedicated period has been of the most significant importance to my life.

First of all, many thanks to my advisor, Professor Michael Todd, for giving me this fantastic opportunity and sparing no effort to provide me guidance along my journey. I still remember the scene when I knocked his door for the first time and nervously had a chat with him. In the following years, Mike kept encouraging me with any success I achieved, no matter how small it is, and led me to become a mature graduate student and someday independent researcher. I learned from him how to critically think and explore, how to tell a smooth story when conveying research ideas, and how to find more questions to answer. Just as the analogy we made, I was not only being trained as a good soldier, but more than that is, I need to become a captain. Mike is such a great person that in the meantime he is also my mentor and friend, there is too much I want to speak to Mike and I owe him a lot.

I would like to thank all my committee members, Professors Charles Farrar, William Hodgkiss, Joel Conte, and Rajesh Gupta, for their personal commitments and technical guidance.

Thanks to my UCSD friends and student colleagues, Colin Olson, Luke Overbey, David Mascareñas, Eric Flynn, Greg Jarmer, Erik Moro, Colin Haynes, Scott Ouellette, and Dustin Harvey, for both technical discussions and friendships. I will never forget the margarita,

mechanical bull and chancellor's 5k that we all suffered.

Last but most importantly, I would like to thank my wife, Ling, for her endless love, support and confidence to me.

The research presented in this dissertation was funded by Air Force Research Lab, Army Research Lab and Air Force Office of Scientific Research.

A portion of Chapter 2 has been published in *Proc. SPIE 7650*, Zhu Mao and Michael Todd, 2010. The title of this paper is “A structural transmissibility measurements-based approach for system damage detection”. The dissertation author was the primary investigator and author of this paper. The fourth section of Chapter 2, in part, has been published in *Mechanical Systems and Signal Processing*, Zhu Mao and Michael Todd, 2012. The title of this paper is “A model for quantifying uncertainty in the estimation of noise-contaminated measurements of transmissibility”. The dissertation author was the primary investigator and author of this paper.

Chapter 3, in part, has been published in *Proc. SPIE 7650*, Zhu Mao and Michael Todd, 2010. The title of this paper is “A structural transmissibility measurements-based approach for system damage detection”. The dissertation author was the primary investigator and author of this paper. A portion of Chapter 3 has been published in *Mechanical Systems and Signal Processing*, Zhu Mao and Michael Todd, 2012. The title of this paper is “A model for quantifying uncertainty in the estimation of noise-contaminated measurements of transmissibility”. The dissertation author was the primary investigator and author of this paper. A portion of Chapter 3 has been submitted to *Mechanical Systems and Signal Processing*, by Zhu Mao and Michael Todd. The title of this paper is “Statistical modeling of frequency response function estimation for uncertainty quantification”. The dissertation author was the primary investigator and author of this paper.

Chapter 4, in part, has been published in *Proc. SPIE 7650*, Zhu Mao and Michael Todd, 2010. The title of this paper is “A structural transmissibility measurements-based approach for system damage detection”. The dissertation author was the primary investigator and author of this paper. A portion of Chapter 4 has been published in *Mechanical Systems and Signal Processing*, Zhu Mao and Michael Todd, 2012. The title of this paper is “A model for quantifying uncertainty in the estimation of noise-contaminated measurements of transmissibility”. The dissertation author was the primary investigator and author of this paper. A portion of Chapter 4 has been submitted to *Mechanical Systems and Signal Processing*, by Zhu Mao and Michael Todd. The title of this paper is “Statistical modeling of frequency response function estimation for uncertainty quantification”. The dissertation author was the primary investigator and author of this paper. A portion of Chapter 4 has been published in *Proc. SPIE 8348*, Zhu Mao and Michael Todd, 2012. The title of this paper is “Uncertainty propagation of transmissibility-based structural health monitoring features”. The dissertation author was the primary investigator and author of this paper. A portion of Chapter 4 has been submitted for publication in *Proceedings of the ASME 2012 Conference on Smart Materials, Adaptive Structures and Intelligent Systems, SMASIS 2012-7935*, Zhu Mao and Michael Todd, 2012. The title of this paper is "The quantification of uncertainty in SHM features derived from frequency response estimation". The dissertation author was the primary investigator and author of this paper.

Chapter 5, in part, has been published in *Proc. SPIE 7984*, Zhu Mao and Michael Todd, 2011. The title of this paper is "Statistical quantification of the uncertainty in transmissibility feature for structural condition binary classification". The dissertation author was the primary investigator and author of this paper. A portion of Chapter 5 has been published in *Proceedings of the 8th International Workshop on Structural Health Monitoring*, Zhu Mao and Michael Todd, 2011. The title of this paper is "Uncertainty Quantification in Transmissibility-Derived Features Used for Fault Detection". The dissertation author was the primary investigator and author of this paper. A portion of Chapter 5 has been published in *Proceedings of IMAC, Society for Experimental Mechanics Series, Volume 29*, Zhu Mao and Michael Todd, 2012. The title of this paper is "Rapid Structural Condition Assessment Using Transmissibilities with Quantified Confidence for Decision Making". The dissertation author was the primary investigator and author of this paper. A portion of Chapter 5 has been submitted for publication in *The Proceedings of the ASME 2012 Conference on Smart Materials, Adaptive Structures and Intelligent Systems, SMASIS 2012-7935*, Zhu Mao and Michael Todd, 2012. The title of this paper is “The quantification of uncertainty in SHM features derived from frequency response estimation”. The dissertation author was the primary investigator and author of this paper.

VITA

2002	B.S.	Tsinghua University
2008	M.S.	University of California, San Diego
2012	Ph.D.	University of California, San Diego

PUBLICATIONS

Zhu Mao and Michael Todd, The quantification of uncertainty in SHM features derived from frequency response estimation, to appear in Proceedings of the ASME 2012 Conference on Smart Materials, Adaptive Structures and Intelligent Systems, SMASIS 2012-7935 (2012)

Zhu Mao and Michael Todd, Statistical modeling of frequency response function estimation for uncertainty quantification, submitted to Mechanical Systems and Signal Processing

Zhu Mao and Michael Todd, A model for quantifying uncertainty in the estimation of noise-contaminated measurements of transmissibility, Mechanical Systems and Signal Processing, Volume 28, p. 470-481. (2012)

Zhu Mao and Michael Todd, Uncertainty propagation of transmissibility-based structural health monitoring features, Proc. SPIE 8348, 834811 (2012)

Zhu Mao and Michael Todd, Rapid Structural Condition Assessment Using Transmissibilities with Quantified Confidence for Decision Making, Proceedings of the Society for Experimental Mechanics Series, Volume 29, 133-140, (2012)

Z.Q. Lang, G. Park, C.R. Farrar, M.D. Todd, Z. Mao, L. Zhao, K. Worden, Transmissibility of non-linear output frequency response functions with application in detection and location of damage in MDOF structural systems, International Journal of Non-Linear Mechanics, Volume 46, Issue 6, Pages 841-853, (2011) Zhu Mao and Michael Todd, Uncertainty Quantification in Transmissibility-Derived Features Used for Fault Detection, Proceedings of the 8th International Workshop on Structural Health Monitoring (2011)

Zhu Mao and Michael Todd, Statistical quantification of the uncertainty in transmissibility feature for structural condition binary classification, Proc. SPIE 7984, 79842H (2011)

Zhu Mao and Michael Todd, A Model of Uncertainty Quantification in the Estimation of Noise-Contaminated Transmissibility Measurements for System Identification, Proceedings of the Society for Experimental Mechanics Series, Volume8, 389-398, (2011)

Zhu Mao and Michael Todd, A structural transmissibility measurements-based approach for system damage detection, Proc. SPIE 7650, 76500G (2010)

Zhu Mao and Michael Todd, Comparison of shape reconstruction strategies in a complex flexible structure, Proc. SPIE 6932, 69320H (2008)

Zhu Mao, Liangjin Gui and Zijie Fan, Research and development of free-fall drop tower impact facility, Experimental Technology and Management, Vol. 20. No.5. P22-29, (2003) in Chinese

Chinese Patent: A kind of hook with the function of releasing, ZL-02-1-48869.X (B66C 1/26), issued on December 7 2005

ABSTRACT OF THE DISSERTATION

Uncertainty Quantification in Vibration-Based Structural Health Monitoring for Enhanced Decision-Making Capability

by

Zhu Mao

Doctor of Philosophy in Structural Engineering

University of California, San Diego, 2012

Professor Michael D. Todd, Chair

This dissertation aims to augment current structural health monitoring (SHM) practice with an approach to model and quantify uncertainty to enable confidence-based decision-making. The SHM application domain is vibration data-based system identification, and more specifically, transmissibility and frequency response function (FRF) estimations are considered, as these are the primary forms of transfer function estimation in the frequency domain. A finite element (FE) model is established in order to supply a benchmark of transmissibility evaluations, and by tuning the FE model, structural damages can be simulated. Two SHM features are proposed to detect and localize defects by analyzing the features calculated at certain interest point arrays.

Considering a realistic test condition, all of the model parameters and data are subject to uncertainty from various sources leading to ambiguous system identification results that cause false alarms (Type-I error) when evaluating hypothesis testing for damage. Based upon stationary Gaussian random process, this dissertation statistically establishes uncertainty quantification (UQ) models for different estimators, and uncertainties of transmissibility and FRF are therefore quantified. A perturbation approach is implemented ending up with standard deviation and bias coefficient of transmissibility magnitude estimations. Probability density functions (PDFs) of transmissibility and FRF estimation are derived, for both magnitude and phase, via different methods, namely Chi-square and Gaussian bivariate approach.

The proposed statistical models are validated by Monte-Carlo test on both FE simulation model and real lab-scale structure. To obtain a more stringent validation condition, extraneous artificial noise is added onto the raw measurements. Compared to the pre-set confidence interval, validation results are illustrated via outlier percentage, which is the observed outlier amount, at each frequency line, normalized by the number of total test cases. Comparison of the UQ results among different statistical models, estimators, and noise contamination levels is presented, for the purpose of guiding users towards using optimal estimators under certain circumstance.

Hypothesis tests are implemented, with statistical models available, and the detection

performance is compared for different detectors, damage levels, and noise contaminations. Receiver operating characteristic curves are used for quantitative visualization of the abovementioned performance qualities. Using area under curve (*AUC*) metric, it is concluded how detection rates trend as damage level and signal-to-noise condition changes, suggesting optimal frequency bands for implementing detection. For example, even for heavily-contaminated cases, there is still acceptable detectability at resonances.

As a decision-making problem, SHM probabilistically involves making correct decisions with acceptable (application-dependent) type-I errors. In the end of this dissertation, probability of detection for different cases and test conditions are optimized and compared, as given certain false alarm tolerance thresholds. By having optimal detections, the damage identification problems have a clearer outline with respect to different hypothesis designs.

1. Introduction

1.1. Background of Structural Health Monitoring

1.1.1. Definition of Structural Health Monitoring

Structure health monitoring (SHM) is the process of implementing a damage assessment strategy for any system, including detection, localization, and classification, via measured in-situ structural performance data. In the context of SHM, damage is typically defined in a performance sense, in that there is change in material and/or geometric properties adversely affecting structural functionality [1, 2]. Usually SHM applications are organized into four steps including: (i) operational evaluation (which includes target damage identification and specification of implementation constraints), (ii) data acquisition and processing, (iii) extraction of relevant features from measured data that will be used for assessment, and (iv) decision making based on appropriate detection/classification of the features. The fundamental assumption is that that damage will alter certain characteristics of a system, which will manifest themselves in some observation of measured data, ideally enhanced by the feature extraction process. The primary goals of such an SHM strategy are typically some form of structural ownership cost reduction, usually through maintenance optimization (or automation), performance optimization during operation, and minimization of unscheduled downtime, and/or life cycle advantage through catastrophic failure mitigation [1]. Damage prognosis (DP) is regarded as the future of SHM, which predicts system performance by assessing the current status, prior experience and model simulation. Extending damage identification, DP integrates other technologies such as predictive structural modeling, probability evolution and uncertainty propagation and quantification. Because of its potential for structural safety, DP is regarded as a 'grand challenge' in the 21st century [8].

Since damage defined as above is not directly measurable and thus indirectly affects observable properties, many SHM strategies have partially or wholly enveloped paradigms in statistical pattern recognition. Pattern recognition is divided into three general categories: group classification, regression analysis, and identification of outliers [1, 2]. Other than this fundamental challenge of indirect observability, other challenges in SHM include the optimization of sensor count and location, damage-sensitive feature extraction, elimination of operational variability and environmental effects that lead to false positives, and quantifying the uncertainty present in any SHM assessment. Despite these challenges, there is a significant body of literature describing current developments in methods for implementing the paradigm across a wide array of different applications [3-7].

Any SHM/DP strategy ultimately requires a decision-making process, which inherently requires, as listed above in the primary challenges of SHM/DP, quantification of uncertainty. Decision-making performance is gaged by metrics such as detection/localization/classification rate, rate of false positives, and/or the optimal trade-off of these properties. This area forms the central intellectual core of this dissertation for a certain type of application.

1.1.2. Survey of SHM applications and methodologies

There has been tremendous applications of SHM to mechanical, aerospace, and civil structures over the last twenty or so years, and some excellent review articles are available in References [9-11]. As examples, some represented works will be introduced from different aspects of the overall SHM picture. SHM features based on some form of modal analysis are the most traditional damage indicators, and for situations involving nonlinearities or output-only data, novel methods are proposed to identify the damage, such as transmissibility and nonlinear output frequency response functions [12-16]. Modal analysis is one form of system identification, which generally forms a basis for what classes of features are proposed to be used for implementation of the SHM strategy. Besides purely data-based approaches for structural diagnosis, finite element model updating is also considered or hybridized with data-based methods [17, 18]. Different sensing techniques are adopted to acquire the needed data such as fiber optic sensors [19], piezoelectric sensors [20], and MEMS sensors [21]. Novel sensor networks [22, 23] are also adopted to enhance SHM practicality, and a review of wireless sensors and sensor networks is available in [24]. Techniques and topics relevant to the scope of this dissertation will be introduced and reviewed in more detail next.

1.1.3. Scope of this dissertation

As defined, SHM aims to provide a current assessment of structures based upon measurements and appropriate feature analysis, in a way that facilitates some hierarchy of decision-making with regard to operations, maintenance, or performance. DP aims to extend the process by integrating probabilistic future load models and failure mode models, with the SHM assessment in order to forecast performance-level metrics, such as remaining useful life [25]. As such, a DP-enabling SHM framework is shown in Figure 1-1, which including four tandem parts: (i) data acquisition and processing, (ii) statistical modeling and uncertainty quantification of detection process, (iii) hypothesis testing for current decision-making, and (iv) probabilistic prediction for potential future actions. From the stand point of damage detection, a decision threshold is obtained after optimal trade-off between detection significance and costs, while for DP, loading and failure models are included into a new stage of probabilistic decision-making with regard to future action.

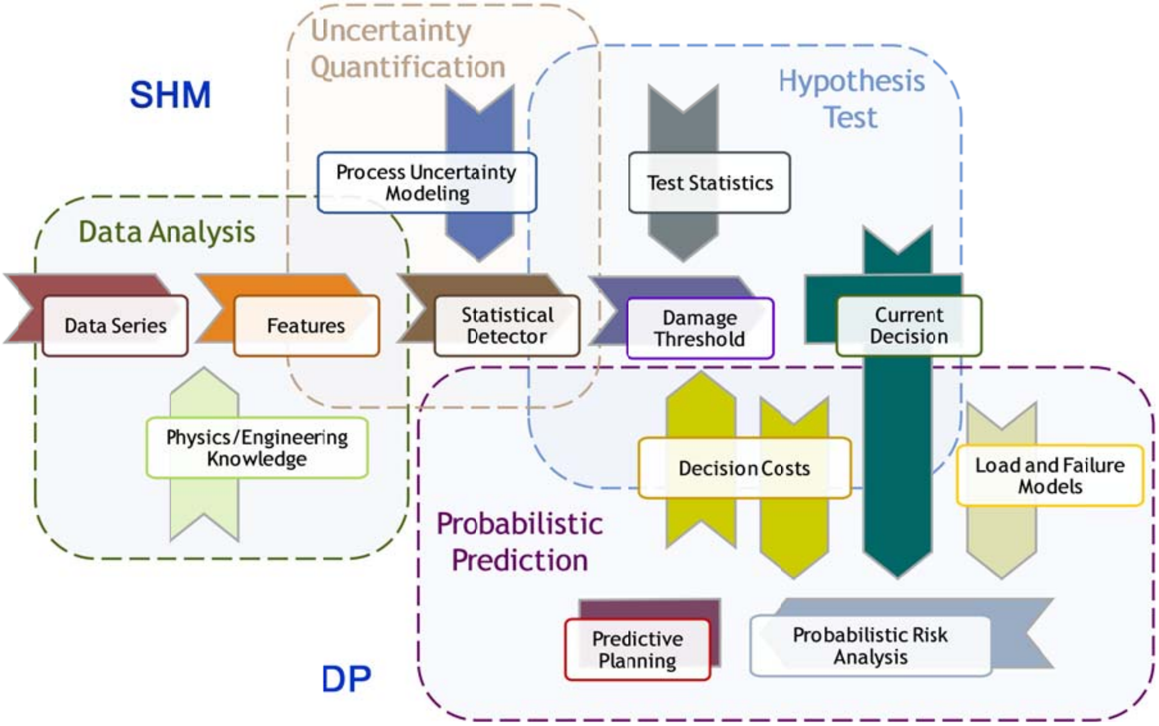

Figure 1-1: Strategy considered in this dissertation

1.2. Background and motivation of project

1.2.1. System identification and vibration-based inspection

System identification technologies are widely applied to every branch of engineering, including but not limited to, system design, control, behavior prediction, and damage detection. For SHM purposes, multiple conditions are compared and for each of them, there is a system identification process involved which builds models (linear, nonlinear, hybrid, nonparametric, time/frequency domain etc.) to identify the cases [26, 27].

Mathematical approaches describing various input/output or output/output relationships have been applied in both the time and frequency domains in order to identify, characterize, or control aspects of global system behavior [27]. Frequency domain approaches, which typically involve estimation of the frequency response function (FRF) in a way that supports modal parameter estimation, are among the most common due to their clear physical interpretation and well-defined computational algorithms, which most commonly involve the Fast Fourier Transform (FFT). Brincker et al. compared the classical frequency-domain modal analysis with other time domain identification approaches and concluded the frequency approach to be more user-friendly and computationally efficient to use [28]. Other system identification applications are reviewed in [29, 30], where specific nonlinear modeling and stochastic system identification for operational modal analysis are surveyed.

For mechanical/structural system identification processes, the frequency domain approach often involves vibration-based testing (e.g., experimental modal analysis via the FRF) to obtain the relationship between structural parameters (mass, stiffness, and damping), the characteristic eigenstate (resonant frequencies, mode shapes, and sometimes damping), and measured vibration responses [31]. In this situation, vibration inspection is often helpful for damage identification. Cawley in early years proposed using measurements of changes in the lower structural natural frequencies, where identification of damage is accomplished combining with dynamic FE structural analysis [32]. A comprehensive review of modal parameter vibration-based damage identifications is presented in [33], emphasizing signal processing techniques. Based upon vibration features, four categories are summarized as natural frequency-based methods, mode shape-based methods, curvature mode shape-based methods and mode shapes frequencies combined methods, with thorough comparison, and implementation-wisely, five often-used damage detection algorithms are studied, namely, frequency-based single damage indicator (SDI) method, mode shape-based generalized fractal dimension (GFD) method, mode shape curvature (MSC) method, gapped smoothing method (GSM), and damage index method (DIM). Pros and cons of each vibration feature and detection algorithm are reviewed [33].

1.2.2. Motivation of rapid state awareness

The US Air Force Research Laboratory aims to develop modular plug-and-play (PnP) satellite architectures in support of the their Operationally Responsive Space (ORS) initiative, in which rapid (~days) assembly, integration, and test (AI&T) of the satellite, with sufficient strength, stiffness, and alignment accuracy is required [34]. A multifunctional PnP satellite structure is shown in Figures 2-2 and 2-3:

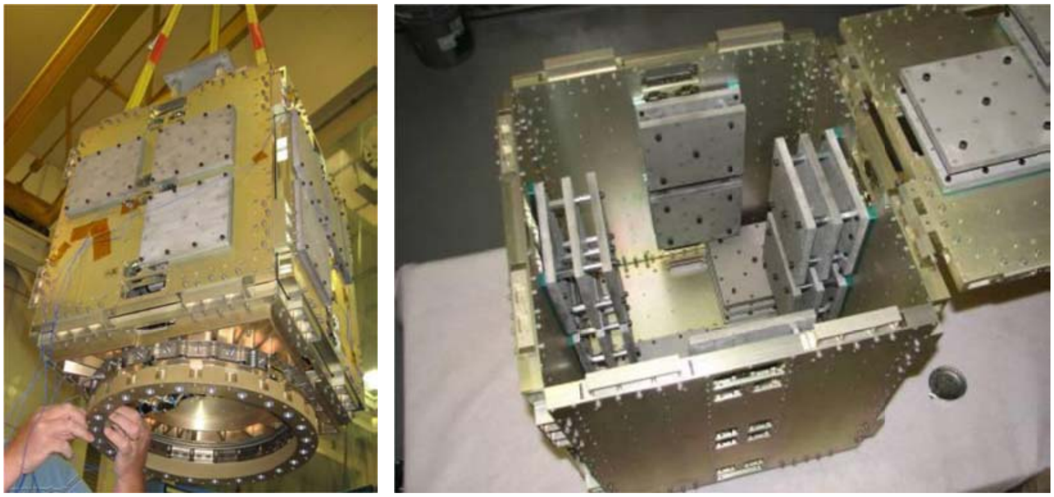

Figure 2-2: Plug-and-Play Satellite (PnPSat) structure and multifunctional panels [34]

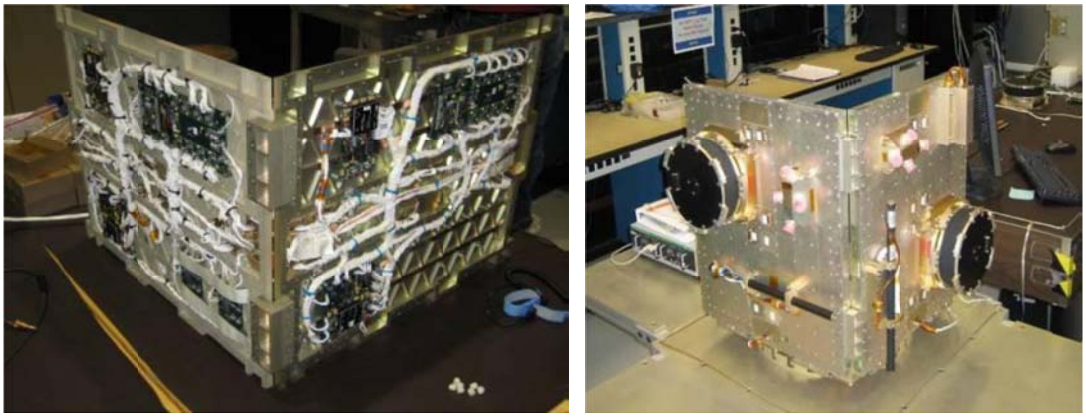

Figure 2-3: electronics embedded within structure (*outer surface is removed*) and components integrated for sub-system testing [34]

Time required for complete AI&T on a satellite ready for launch and on-orbit operations is to be reduced from, currently, months to less than a week. In order to meet this goal, the pre-launch qualification and system integration process of this type of bolt-connected satellite needs to be dramatically truncated, especially the inspection duration [35-38]. Advanced techniques for fastener loosening detection have been deployed via chaotic guided ultrasonic waves (CGUW) tests, and state space reconstruction to identify preload loss [39, 40]. However, traditional vibration-based SHM, which is more compliant with current testing capabilities and qualification regulations, is considered as another possible candidate and forms application domain for work in this dissertation.

1.2.3. Transmissibility and FRF

As mentioned in section 1.2.1, frequency domain based system identification and SHM applications are widely used. But any frequency domain approach that relies on frequency response function (FRF) estimation, however, requires either direct measurement of or an assumption of the input excitations to the system [28]. It is well-known that for some applications such measurements are impossible or difficult to obtain, and/or such assumptions would be poor or inappropriate; for these situations, estimation of a transmissibility function is possible. Similar to a traditional input-output transfer function such as the FRF, the transmissibility function is defined as the frequency-domain ratio between two outputs, and it describes the relative admittance between the two measurements. Devriendt et al. interpret the transmissibility concept versus transfer function as response data normalized by a reference response instead of by the input excitation [41]. The transmissibility also contains less general but more specific (local) information compared to the FRF, because the characteristic polynomial, which contains all the system poles (resonances), will be cancelled in calculating transmissibilities, and only the system zeros (anti-resonances) will remain. Therefore, transmissibility-derived features are entirely independent of system poles but solely dependent on zeros. Unlike the system resonances, which are influenced by structural parameters globally, system anti-resonances are more affected by local properties and are more sensitive to detailed structural modeling and change detection (such as for damage identification). As a result, transmissibility appears to be a useful characteristic in identification with more sensitivity to local structural details and effects [16, 42].

A generalization of the transmissibility concept is introduced by Ribeiro et al. [42]. For a multi-DOF structure, the transmissibility can be derived from the FRF matrix, where the FRF matrix is obtained from either testing or analytical/numerical modeling. This relates the set of measureable coordinates and the set of interest coordinates together and makes the identification process more convenient. Mottershead [44] suggests a useful alternative for modal analysis and demonstrated that the sensitivity of the zeros estimated from response measurements and FRF estimations may be expressed as linear combinations of the sensitivities of natural frequencies and mode shapes, where the closer modes contribute more to the sum. He et al. [45] study the sensitivity about local mass and stiffness with respect to the anti-resonance locations when applying relocation of zeros for vibration reduction purposes.

One application area receiving lots of attention is using transmissibility estimation for better quality modal parameter evaluation. Considering the operational modal analysis context with output-only measurements available, Devriendt et al. [42] successfully generalize the modal identification process where the excitation can be any type of input, not constrained to be a white noise sequence. By combining transmissibility data under different loading conditions, they show a good consistency between the modal parameters estimated from transmissibility measurements and the actual system poles. They report that by considering two different transmissibility estimations corresponding to the same positions but with different input excitation, the estimations cross each other at the system resonances, which means different estimations are exactly the same value at system poles. This value is directly related to scalar mode shapes and is used for modal parameter extraction in a multiple-input/multiple-output (MIMO) procedure and for accurate system poles localization [41, 46].

Transmissibility-based system identification, for many of the reasons described above, is also getting increased attention in the area of damage detection and structural health monitoring [47-49]. Johnson et al. apply transmissibility-based diagnostic technology to reduce the dimension of response measurements and demonstrated analytically and experimentally the sensitivity of transmissibility to both linear and nonlinear system changes [16 47], as well as significantly enhanced localization capability since the system zeros are only sensitive to the parameters in certain localized region, and anti-resonance frequencies show significant variations with different measurement positions [16, 50]. Worden et al. [15, 49] implement system damage/fault detection via neural network training and outlier analysis, demonstrating that the system transmissibility provides a sensitive feature for the detection of small stiffness variation. Therefore, with the transmissibility-based technique, it is straightforward to identify the appearance and location of the system parameter changes. System identification results have shown that the localization is effective on both discrete [16] and continuous [50] system applications. Worden et al. [51-53] go through the entire process of experimental validation of a SHM methodology, based upon the measured transmissibilities and novelty detection. The investigation expands from simple laboratory structures to complex and realistic structures such as aircraft wing, and both the results from detection and localization are validated.

1.3. Uncertainty Quantification

In reality, there is uncertainty existed, which compromises any engineering problems at different levels, and uncertainty quantification (UQ) technique is demanding in order to minimize the influence from uncertainties.

In system identification application, frequency domain estimations are compared to FE model prediction, but both modeling and testing involve a number of different sources of uncertainty, and model updating techniques are used to drive model/test correlation to convergence [55]. Therefore, quantifying the uncertainty associated with both model and experimental data, and studying the propagation of uncertainties through FE simulation and signal processing are critical [56].

For vibration-based practices, inherent to any quality assessment is the quantification of uncertainty, as it is well known the sensitivity of any feature derived from transmissibility (or any other system identification quantity such as FRF) is compromised by noise, generally categorized into four classes: operational, environmental, measurement, and computational [54]; these compromised estimates may lead to significant false-positive (Type-I) errors in the interpretation of system identification results, regardless of specific application.

For applications of risk/reliability analysis, and SHM where decision-making is directly involved via some form of hypothesis testing, the field of UQ is used to reduce corresponding costs and provide robust decision-making information [57]. Mace et al. point out that generally the application of UQ with any degree of comprehensiveness is a formidable task which has three major aspects: quantification of variability in current theories, fusion of descriptions by different theories, and propagation of uncertainty through various processes [58].

There are a lot of research been done in the past decades. For general UQ methodologies in different research areas, there is a brief review in section 1.3.1. For specific statistical modeling of vibration-based SHM feature uncertainties, which is central core part of this dissertation, and probabilistic SHM/DP, which is the a further step beyond the scope of this dissertation, state-of-art is reviewed in section 1.3.2 and 1.3.3.

1.3.1. A review of uncertainty quantification

The most traditional UQ method in many engineering disciplines is to carry out a Monte-Carlo simulation, starting from a given/assumed probability distribution of inputs or model parameters, and ultimately specifying probabilistically the distribution of any characteristics of interest. For example, Reference [56] compares the statistics of FRFs of an Euler-Bernoulli beam and a thin plate obtained from both FE models and experimental modal analysis on one hundred nominally identical specimens. However, for FE models with large degrees of freedom and likely a relatively large number of uncertain parameters, a very large number of simulations are required to cover the entire random variate domain before reaching sufficient statistics to quantify the model uncertainty [57-60]. More sophisticated statistical models have been proposed to quantify the imprecision in structural dynamics and spectral analysis in a less computation-expensive way, but the Monte-Carlo approach remains the benchmark because of its universality and stability [55, 58].

Uncertainty in transfer function estimations has been classified into aleatory and epistemic types; aleatory uncertainty is from the inherent baseline randomness and imperfection in the simulation/experiment, and epistemic uncertainty is caused by lack of information/knowledge. Accordingly, the UQ processes are divided into two types. The aforementioned Monte-Carlo method is of the probabilistic approach, which considers the aleatory uncertainty and quantifies the uncertainties in acquired data. On the other hand, the possibilistic approach only characterizes the bounds in which all parameters lie without knowing the actual distribution, and therefore it considers the epistemic uncertainty and applies well in FE model updating [58, 60, 61]. The possibilistic approach deals with, but is not limited to, evidence theory (also known as Dempster–Shafer Theory), interval analysis, fuzzy theory, Bayesian Theory, Convex Model Theory, and information gap decision theory for severe uncertainty [62].

No matter what type of uncertainty is being quantified, reducing computation complexity is one of the core parts of UQ research. Manson et al. proposed interval analysis and affine analysis to assess the parametric uncertainties on the FRF, which, compared to the traditional Monte-Carlo approach, give conservative bounds that are much faster to obtain [63]. A nondeterministic identification method is proposed to quantify the uncertainty of modal parameters with experimental data by [55], and a fuzzy formalism is used to provide confidence level because of its compatibility with data imprecision and incompleteness. Other possibilistic UQ analysis such as evidence theory is developed with both epistemic and aleatory uncertainties approximately taken into account. The algorithm has a flexible framework for imprecise information and is more cost effective compared to traditional approaches [60].

The Monte-Carlo method samples output distribution accordingly based upon distributions of inputs and parameters, ending up ultimately with probabilistic models. A lot of research has been done by approximating the original model with a lower-order transformation with less computational expense. Reference [64] describes an efficient technique to probabilistically quantify the parameter uncertainty by maximizing the likelihood of experimental measurements, in which polynomial perturbation is adopted to simplify the original model and compute likelihood. The perturbation approximation shows sufficient accuracy if the response is not a highly nonlinear function of parameters. Dealing with system response Probability Density Function (PDF) with acceptable computation consumptions, Polynomial Chaos Expansion (PCE) is another replacement model considering the sparsity-of-effect principle, and PCE with points of monomial cubature rules is constructed. Different from a perturbation method, PCE uses a set of multi-dimensional Hermite polynomials as orthogonal bases to expand the probability space and is convergent in the mean-square sense [65]. A non-intrusive PCE model is developed to predict uncertainty of FE model-derived FRFs with PDF given [62]. By using a Bayesian metamodel, Reference [61] also focuses on analyzing the uncertainty of FRFs obtained via FE model, and the emulator reduces the number of FE evaluations. Point-wise uncertainty intervals and uncertainty envelope function are developed by considering, respectively, the uncertainty at discrete frequency lines and continuous frequency range. Response surface and first-order reliability method (FORM) are also good surrogates to expedite the evaluation of the original FE model [57, 59]. A general symbolic regression using genetic programming is deployed in [59], in which the improvement has been demonstrated on both univariate and multivariate problems with both computational and experimental data.

The same ideas of UQ may be applied to other models and applications. With probability preservation, the probability density evolution equation of nonlinear dynamic response for stochastic structures can be uncoupled from the dynamics, and the instantaneous PDF for any system response is obtained as the system is evolving in time; and research about parametric sensitivity of the importance measure based upon the corresponding cumulative distribution function (CDF) is also developed [66, 67]. Reference [68] quantifies the uncertainty of a neural network regression model via interval set techniques, in which the multi-layer perceptron network with Bayesian evidence training is adopted for experimental fatigue life measurements in glass fiber composites. UQ is also applied to investigating a plant model for robust control oriented identification, in which perturbation method is used for quantification of corrupted plant frequency responses [69].

The counter part of FE model-based transfer functions computation is data-based estimation, in which the FRF is often obtained by calculating the input-output transfer spectrum through time series measurements from vibration-based experiments. Besides of the modal parameter extraction, those frequency domain transfer functions, including FRF and other spectral forms, are often selected as indicators of (especially online) assessment of structural state of health [70, 71]. However, the uncertainty in FRF estimations will cause misidentification of test results, and induce non-damage-caused change, i.e. false positives. This motivates a UQ model to filter out those Type-I errors to support more robust decision-making, and section 1.3.2 specifically reviews the vibration-based feature UQ via statistical modeling.

1.3.2. Current statistical modeling

Some research has been done to statistically model the uncertainty and variation of estimations of transfer functions, e.g. transmissibility and FRF. Doebling and Hemez give an overview of a project at Los Alamos National Laboratory that aims at UQ methodology and assessing the total predictability of structural dynamics simulations, and the uncertainty propagation through numerical simulations is also discussed [72].

Other related research proposed various ways to quantify variation of transfer functions [73-75]: an asymptotic variance is proposed of the transfer function estimated via a frequency-domain Gaussian maximum-likelihood estimator; by using a mixed probabilistic-worst-case approach, Reference [74] identifies error bound of a linear nominal model which is made up of a deterministic component due to unmodeled dynamics, and a probabilistic component due to noise; and variance is derived through perturbations of true power spectrum in [75]. In addition, time-variant coherent causality-based analysis is implemented by Trethewey [76], where nonstationary time variant excitation sources are separated via Short Time Fourier Transform (STFT), in which noise effects in the vibration can be distinguished. Goodman formulates the confidence bands for all elements in the FRF matrix approximately using an F-distribution, and the confidence bands are given as functions of coherence [77, 78]. With a Gaussian input and optimized channel assumption, Bendat and Piersol apply perturbation analysis and derive the standard deviation of FRF estimations with respect to coherence function between input and output, through which the uncertainty bounds for different confidence levels could be expressed approximately in a Gaussian way [79-81]. Reference [82] applies multivariate uncertainty analysis and extends Bendat's model in [79-81] getting the sample covariance matrices for FRF of a linear system. With zero input noise, the model characterizes the same situation as Bendat's model does, and the derived expressions are identical to those from Reference [79-81]. But for the cases that noise existed on both input and output side, the model does not explicitly give a closed-form.

In this dissertation, the distribution of data-based transmissibility and FRF estimations, both magnitude and phase, by deriving order statistics and PDFs, is characterized, which outperforms the existing models mentioned above.

1.3.3. Probabilistic SHM/DP

Adopting current statistical models, SHM process can be enhanced and extended to DP, among which, Bayesian probabilistic SHM approach is one of the most active areas [25, 83, 84]. An improvement in fatigue diagnosis and prognosis of structures is achieved using Bayesian probabilistic techniques by [85-87], and frequency-wave-number migration technique, image-segmentation technique, Bayesian autoregressive integrated moving average (ARIMA) model and probability of detection methodologies are developed. Probabilistic SHM and damage identification are also implemented by [88-91], by means of stochastic subspace-based covariance-driven identification method, design of detection algorithms, Bayesian inference and imprecise probabilities with fuzzy parameters. Considering the statistical model established in this dissertation, this filed is suggest as future work.

1.4. Contributions of the dissertation

Motivated by the demanding of rapid structural state assessment, transmissibility-related features are adopted in the SHM framework. Statistical modeling process is deployed fulfilling the need of SHM application, in which features are evaluated subject to uncertainties and decision boundaries of state assessment are desired in statistical sense. Itemized contributions are list below:

1) Development of two metrics of transmissibility change for the purpose of damage

detection;

2) Case study of damage localization via proposed two metrics;

3) Analysis uncertainty sources in data based transmissibility estimations and comparing different estimators of transmissibility and FRF;

4) Uncertainty quantification of different estimators via different statistical modeling approaches;

5) Validate statistical models via Monte-Carlo test, designed outlier percentage and other quantitative metrics;

6) For UQ models with full characterization of PDFs, implement hypothesis tests regarding different paradigms of SHM and damage identification problems;

7) Quantify the sensitivity and specificity of different features in the decision-making process established in (6);

8) Quantify the trade-off between probability of false alarms and probability of detection, for different features, including FRF and transmissibility, magnitude and phase.

2. Vibration-based inspection and SHM features

Based upon the structural state awareness motivation addressed in Chapter 1, vibration-based inspection is deployed onto a surrogate satellite FE model to initiate the transmissibility-related SHM process. Transmissibility definition will be introduced in this chapter and evaluated on this specific structure as a benchmark, comparing which to the evaluations from damaged case with fastener loosening simulated in FE model. For damage identification purpose, features of transmissibility change are presented, leading to a damage detection and localization capability. For real structural test, transmissibility are usually not assessable through well-performed FE model, but through experimental data instead. Therefore, the end of this chapter will review and compare different data-based estimation algorithms (often called estimators) and give an overview of their accuracies.

2.1. Simple satellite model

2.1.1. FE model

In this work, the problem is investigated on a simplified representative PnPSat structure (e.g. CubeSat) within a finite element computational model. A cubic shell (plate)-frame assembly is designed in ABAQUS, shown in Figure 2-1(a), to present a simplified satellite structure. Six plates, whose dimension is 1m×1m and 2mm thick each, are connected onto the cubic frame, whose thickness is 50mm, with fixed-base boundary conditions as shown in Figure 2-1(b). The material is chosen as linear elastic aluminum and specific finite element details are given in Table 2-1. In the finite element model built in ABAQUS, 19,922 elements are used and the physical size of each element varies from 0.025 to 0.04 m, deemed sufficient by a model convergence investigation. This model places tunable (in stiffness) linear elastic connections along all sections of the frames, mounting the plate to the frame to simulate the displacement-dependent load transfer property of bolt connections. For specific damage behavior-learning purposes, the edges of plates were divided into small blocks first, so that the contact stiffness is tunable at each localized area, as Figure 2-1(c) shows. The original (undamaged) contact stiffness of the updated model is set to be 10^{12} N/m/m^2, which is approximately calculated as the Young's modulus divided by the frame thickness, and damaged contact stiffness is then specified to simulate preload loss, which will be addressed in detail next section.

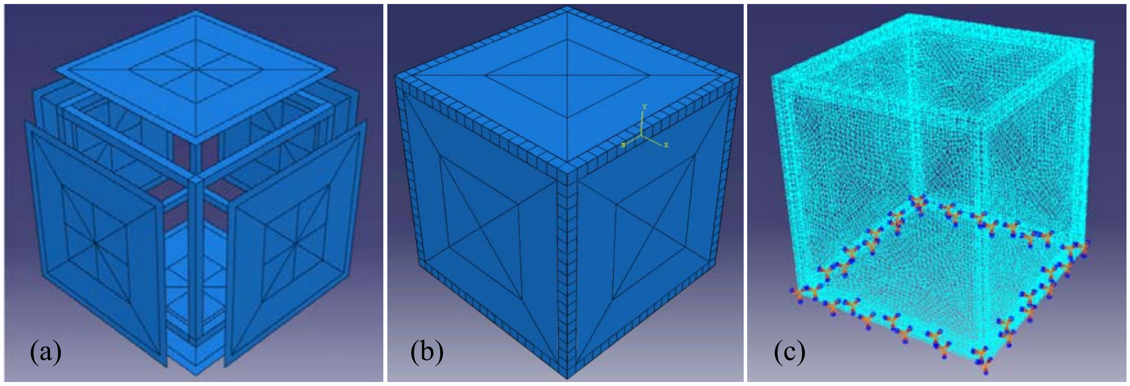

Figure 2-1: (a) geometric model, (b) assembled geometric model, and (c) FE mesh model with fixed boundary at the base

Table 2-1: finite element properties of the model

Component	Number of nodes	Number of elements	Elements	Number of parts
Plate	3119	3042	2994 Linear quadrilateral elements of type S4R 48 Linear triangular elements of type S3	6
Frame	3389	9283	Linear tetrahedral elements of type C3D4	1

The initial thrust was to consider modal analysis to observe possible changes in dynamic behavior between completely fastened and unfastened states. A modal simulation is implemented on this shell-frame assembly in the fully-fastened connection, and natural frequencies and mode shapes are extracted. Because of spatial symmetry, there are repeated modes, and only the first six of the non-repeated mode shapes are shown in Figure 2-2. Superimposed on top of the displacement patterns are the local von Mises strain levels. The corresponding first six (non-repeated) natural frequencies were about 22, 45, 66, 81, 101, and 130 Hz.

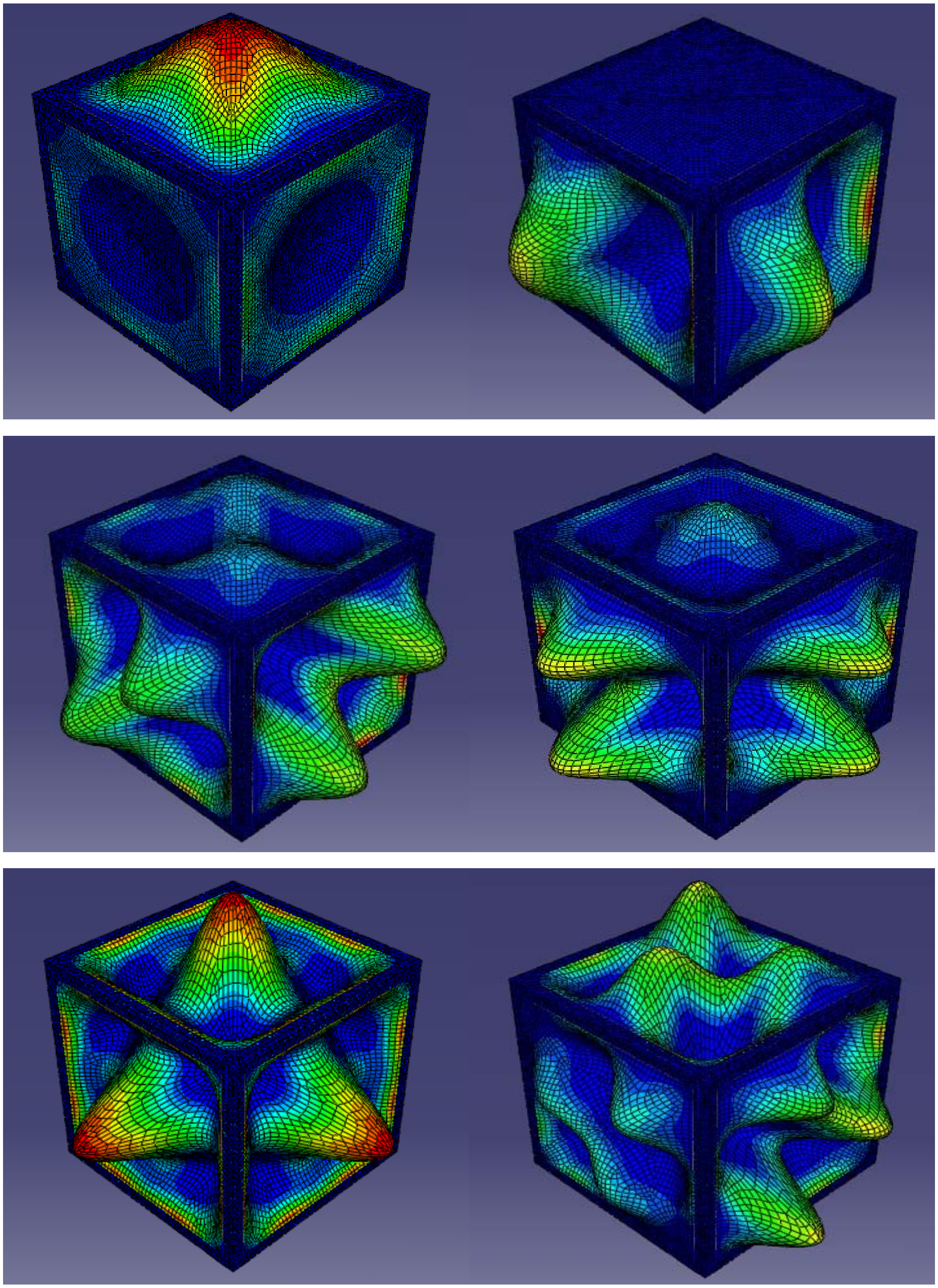

Figure 2-2: first six distinct fully-fastened mode shapes

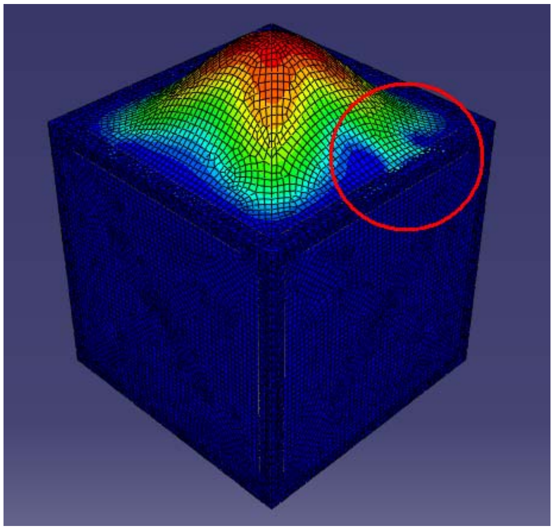

Figure 2-3: mode shape change due to local loosening

When a local region is unfastened, the hypothesis is that modal properties would change. Figure 2-3 shows such a (subtle) change for a particular mode shape, where there is a slight loss in the shape symmetry, as well as local strain concentrations. Not surprisingly, we observed that individual frequencies were fairly insensitive to low damage levels (i.e., only small regions of preload loss, corresponding to 1-2 bolt pressure regions,) but perhaps wide-band frequency information, coupled with mode shape estimations, could provide sufficient evidence to implement a simple, yet robust verification test.

2.1.2. Percussion test and feature extraction

Percussion test is generally the simplest way to excite a structure with (theoretically) broad energy distribution across a band of interest, resulting in multi-mode excitation. This test is simulated in ABAQUS by exciting the structure with a narrow-band pulse and choosing a grid of nodes (interest points) at which to sample the resulting acceleration. The width of the impulse is set to be one millisecond, which is technically not “zero-width” and not exactly “white” in frequency domain, as shown in Figure 2-4(c), but much shorter than the period of the highest mode being interested in. (The highest mode in this analysis has a period of about 0.01 second.)

Further percussion tests (with both center and offset excitation, at point #1 and #9 labeled in Figure 2-5) are implemented under different damage circumstances, and the contact stiffness is varied from 99% to almost 0% of the original stiffness, which is plotted in log-scale in Figure 2-6, while in the undamaged areas (red areas in Figure 2-5), the contact stiffness is 100% (10^{12} N/m/m^2).

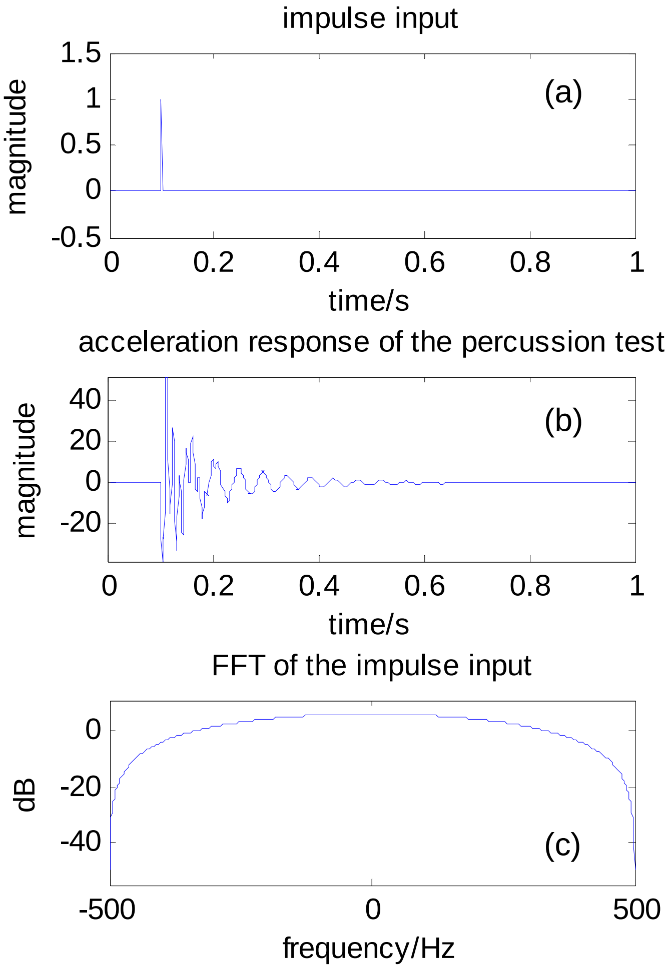

Figure 2-4: (a) impact time history, (b) acceleration response, and (c) Fourier Transform magnitude of the impulse excitation

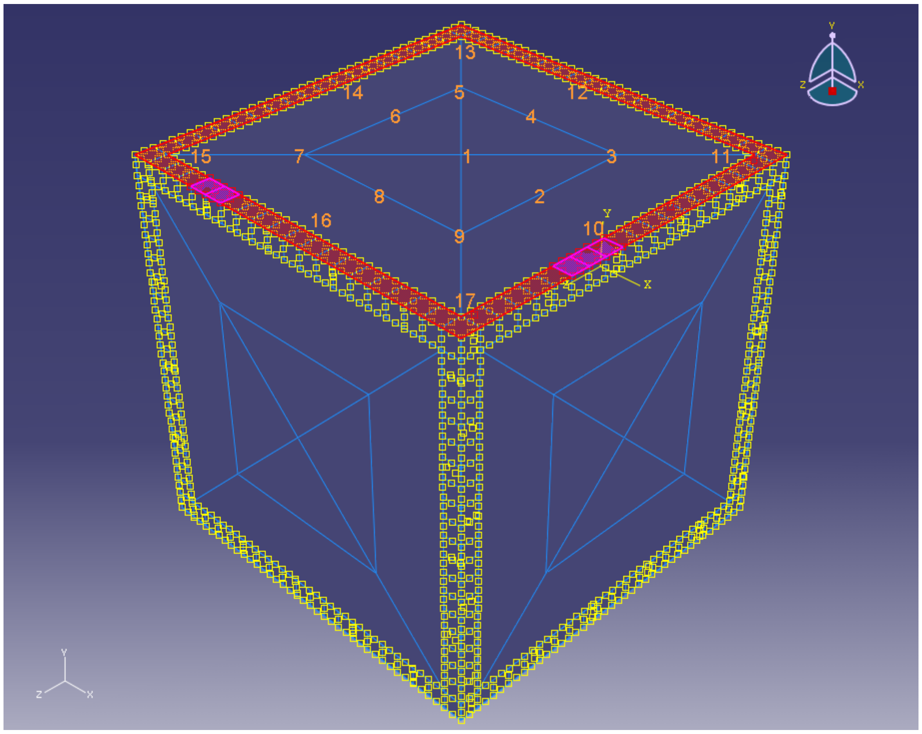

Figure 2-5: interested points and location of damages (purple blocks)

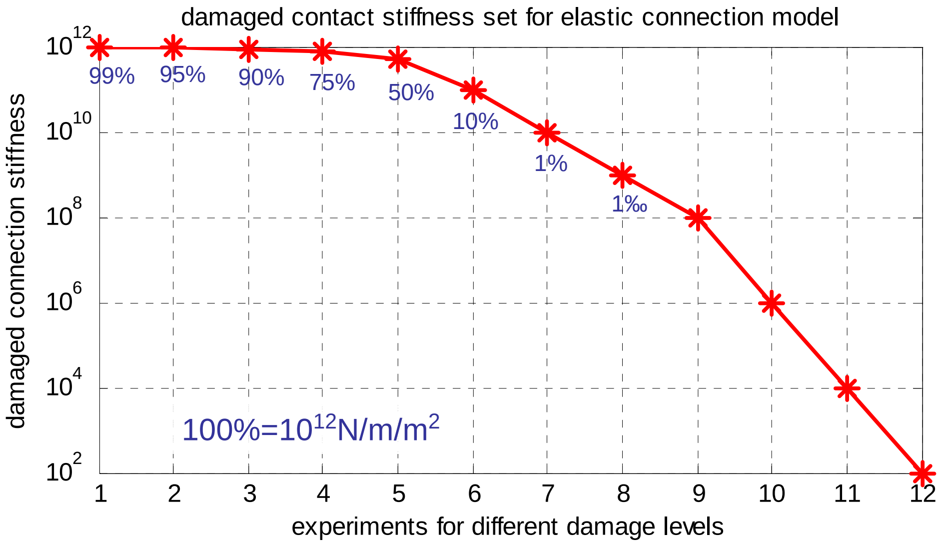

Figure 2-6: specific preload loss levels

According to Figure 2-5, there are seventeen interest points (IPs) in total, marked for convenience, where acceleration responses will be calculated with impulse excitation applied onto point #1 and #9. Hence, the dimension of transmissibility matrix will be 17-by-17 with all pairs of IPs covered, and any off-diagonal term will be reciprocal of its transpose entry. For traditional FRF, there are 2-by-17 evaluations in this test.

2.2. Formulation of transfer functions

Motivated by the specific kind of vibration tests used in system identification process, as the FE structural simulation and percussion test stated in last section, this work will consider a single-input/multiple-output (SIMO) data flow without losing generality of methodology. In Figure 2-8, $u(t)$ denotes the input excitation into a structure, and $v_i(t)$ and $v_j(t)$ represent the output responses at arbitrary degree-of-freedom i and j. Although the above-mentioned input and output signals can be any measurable kinetic/kinematic quantities, such as force, strain, displacement, velocity, acceleration, etc., the most common measurement convention--which will adopted here--is force input and acceleration output.

Figure 2-7: vibration-based inspection illustration

According to the data flow in Figure 2-7, Equations (2-1) and (2-2) give the definition of two transfer functions, FRF with respect to input $u(t)$ and output $v_i(t)$ or $v_j(t)$ and transmissibility between DOF i and j, in the signal sense:

$$H_{i,j}(\omega) = \frac{V_{i,j}(\omega)}{U(\omega)} = \frac{\mathcal{F}\left[v_{i,j}(t)\right]}{\mathcal{F}\left[u(t)\right]}, \tag{2-1}$$

$$\text{and}\quad T_{ij}(\omega) = \frac{V_i(\omega)}{V_j(\omega)} = \frac{\mathcal{F}\left[v_i(t)\right]}{\mathcal{F}\left[v_j(t)\right]}, \tag{2-2}$$

where $U(\omega)$ and $V(\omega)$ denote the associated input and output spectra in frequency domain and $\mathcal{F}$ is the Fourier Transform operator, by which information is mapped from time domain to frequency domain.

2.3. Change of transmissibility

The transmissibility is able to be illustrated on a simplified representative structure (e.g., CubeSat in section 2.1) subject to local fastener loosening within a finite element computational model. This model places a tunable (in stiffness) elastic spring at certain locations connecting the plate to the frame to simulate the displacement-dependent load transfer property. The damaged areas are chosen arbitrarily as shown in pink in Figure 2-5. As mentioned before, the degradation of the specified contact stiffness in the contact areas is regarded as damage (preload loss), thereafter seeing change of transmissibilities induced by this damage is anticipated. For quantitative study, because the amount of change may be highly cohered with the severity of damages, two transmissibility-based features are proposed to quantify this issue.

2.3.1. Features

The working hypothesis is as fastener preload changes, the relative local stiffness of the structure changes, and measured transmissibility paths should be changed. In order to quantify transmissibility changes more compactly, two such evaluation metrics are considered in this section. One is the root-mean-square difference (*RMSD*), defined in Equation (2-3):

$$RMSD_{ij} = \sqrt{\frac{1}{n_{bin}-1}\sum_{l=1}^{n_{bin}}\left(\Delta T_{ij}(\omega_l) - \bar{\Delta} T_{ij}\right)^2} , \tag{2-3}$$

where difference between undamaged and damaged transmissibility set $\Delta T_{ij} = T_{ij,\text{fastened}} - T_{ij,\text{unfastened}}$, $\bar{\Delta} T_{ij}$ is the average difference over entire frequency domain, and n_{bin} is the total amount of bin numbers (frequency lines). The interpretation of *RMSD* is an average Euclidean “distance” between the two feature sets describing how different the two vectors are.

A second metric, dot-product-difference (*DPD*), considers the projection of the baseline (undamaged) and test transmissibilities via the dot product, normalized subsequently by the length of the feature vectors. The result is the cosine of the projection angle, or shown in Equation (2-4):

$$\cos\theta_{ij} = \frac{T_{ij,\text{fastened}} \cdot T_{ij,\text{unfastened}}}{\left|T_{ij,\text{fastened}}\right|\left|T_{ij,\text{unfastened}}\right|}. \tag{2-4}$$

From this definition, we can see that if the two feature vectors are orthogonal, the evaluation will be zero, and if they are parallel, the evaluation is 1 or -1. For normalization, we define the *DPD* metric as $1-\left|\cos\theta_{ij}\right|$:

$$DPD_{ij} = 1 - \left|\frac{T_{ij,\text{fastened}} \cdot T_{ij,\text{unfastened}}}{\left|T_{ij,\text{fastened}}\right|\left|T_{ij,\text{unfastened}}\right|}\right|. \tag{2-5}$$

Compared to the *RMSD* metric, this metric has the advantage of scaling between 0 and 1.

2.3.2. Damage detection

Figure 2-8 and 2-9 show two example sets of transmissibility curves and quantified metrics via above-described percussion tests, which are between IP pairs 10-16 and 11-15, with different damage levels. Upper rows in Figure 2-8 and 2-9 are from center excited percussion and lower rows are from offset excitations. Metrics evaluations are plotted as well, with *RMSD* on the top and *DPD* underneath.

Generally speaking, both of the metrics increase as stiffness loss occurs (increasing damage). For severe damage cases, as an example, the damaged stiffness lower to 1% of the original, it is very easy to capture the raw transmissibility curve shift, but for small damage cases, the metrics are necessary for magnifying and determining the differences. From the two figures, it roughly looks that *DPD* metric is more sensitive for detecting the transmissibility change in center-excited percussion tests, and *RMSD* is more unbiased between the two metrics and could capture very little change of structure. However, this preliminary conclusion is only for these specific IP pairs, and under different circumstances with different IP locations relative to damage positions, there might be a different observation, and this will be addressed in next section.

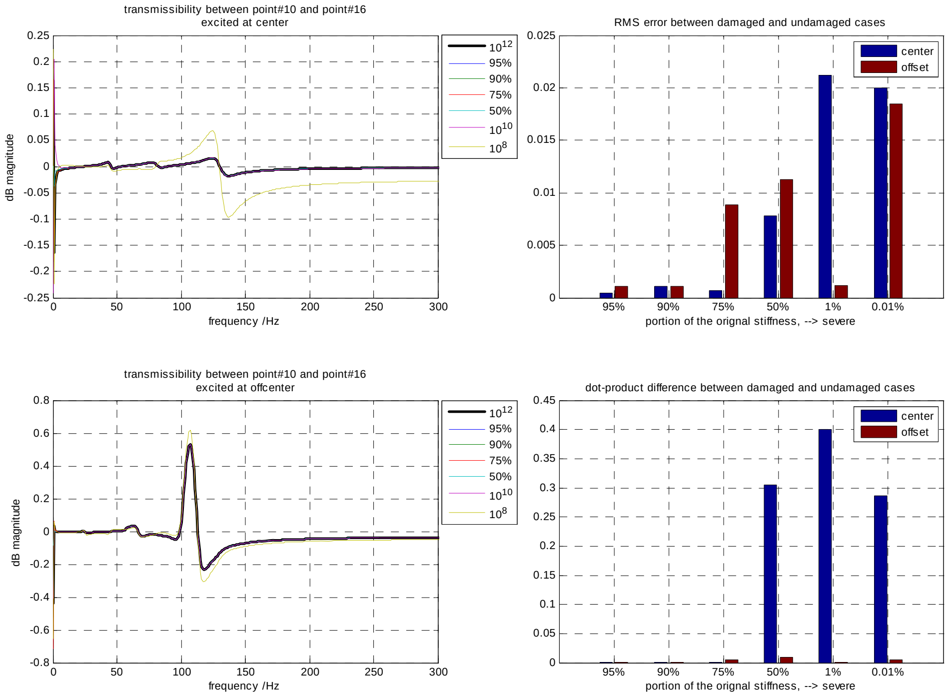

Figure 2-8: transmissibilities and change of metrics for measurement points 10-16

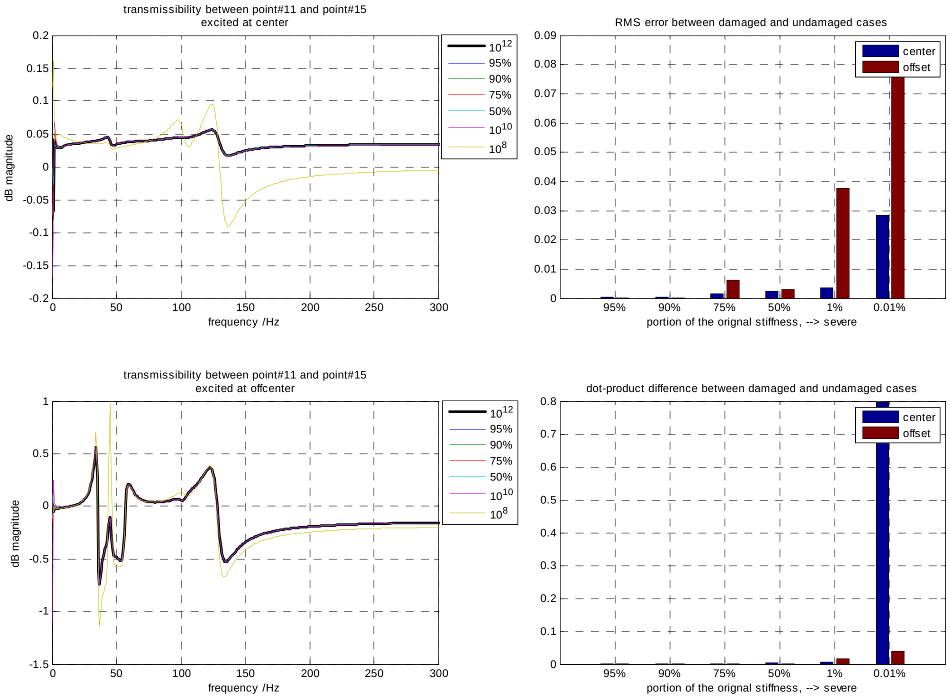

Figure 2-9: transmissibilities and change of metrics for measurement points 11-15

2.3.3. Damage localization

Figure 2-8 and 2-9 just showed that certain metrics can capture change of transmissibility easily with examples at two pairs of IPs and two different percussion locations. One further demand is illustrating the transmissibility feasibility for damage localization. In Figure 2-10 to 2-14, the transmissibility error matrices for selected damage levels with all the combinations between any two IPs are color-plotted, and for each level of the damages, we will have 4 maps of transmissibility errors, for both center (left column) and offset (right column) excitation, and for both *RMSD* (upper row) and *DPD* (lower row) metric. Due to the limited space, only necessary plots from selected damage levels are included for illustrative purposes.

In these color maps, some of the peaks are marked, especially those peaks where the measuring pairs are close to the damage regions, such as points 7, 10, 15, 16 and 17, which are labeled in red. From these error maps, we have the following observations:

- For damage existence recognition, the transmissibility change is quite obvious to be detected, and *DPD* metric is less noisy than *RMSD*, and it is also more sensitive to capture the transmissibility changes.
- For damage localization, which is a higher level of structural health monitoring, some peaked pairs are correlated with damaged areas, such as points #10, #16 and #17, but due to

the coarseness of the interest points array, and the possible coupling and reflecting of structural dynamics, there is no clear determination of damage position correlated with the error peaks, which encourages better detectors in the future.

- On the other hand, some error peaks tend not to correlate with the actual damaged areas, but these peaked pairs are very consistent in different damage levels, such as the dot product metric at pair #12 and #14 for center-excitation at all damage levels. In this case, the relation between error-peak location and fastener loosening area should be investigated for a better localization quality.

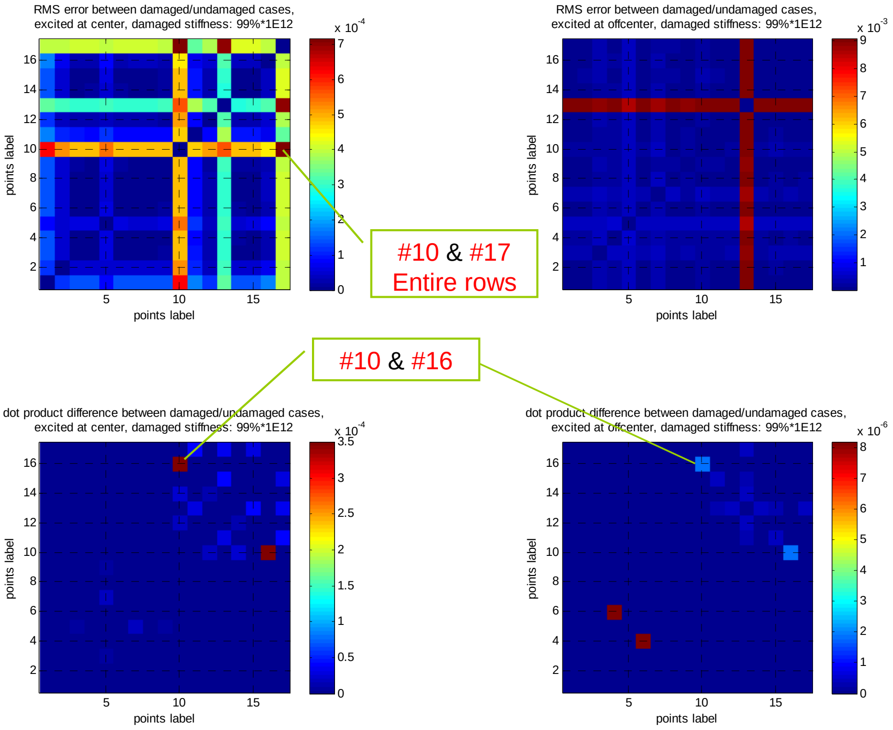
RMS error between damaged/undamaged cases, excited at center, damaged stiffness: 99%*1E12

RMS error between damaged/undamaged cases, excited at offcenter, damaged stiffness: 99%*1E12

#10 & #17 Entire rows

#10 & #16

dot product difference between damaged/undamaged cases, excited at center, damaged stiffness: 99%*1E12

dot product difference between damaged/undamaged cases, excited at offcenter, damaged stiffness: 99%*1E12

Figure 2-10: error maps for 99% stiffness retention

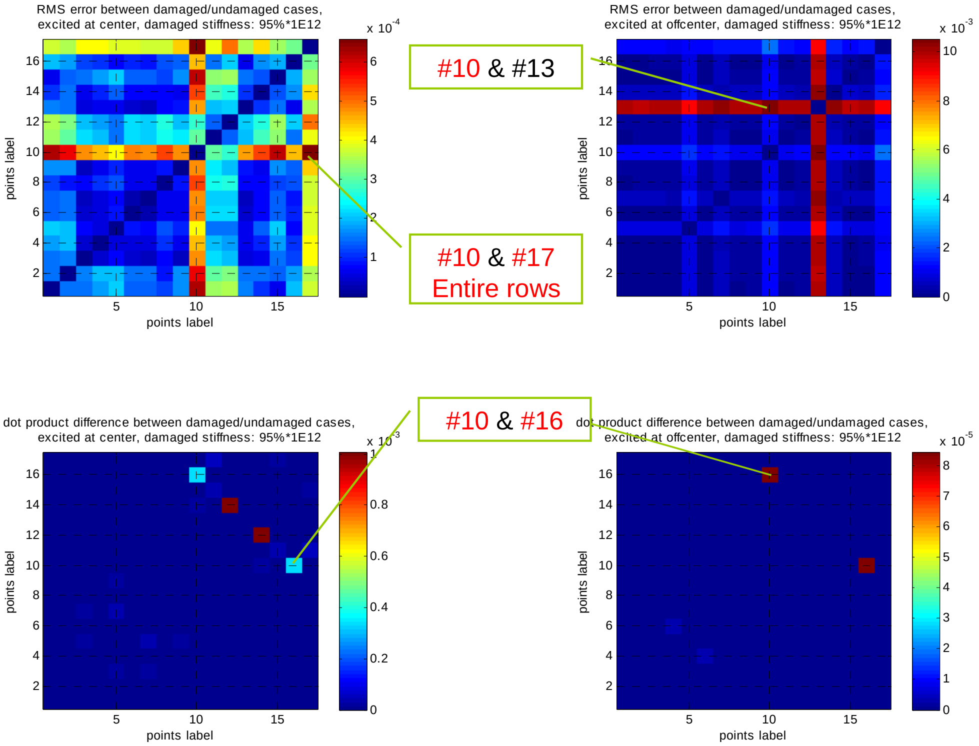

Figure 2-11: error maps for 95% stiffness retention

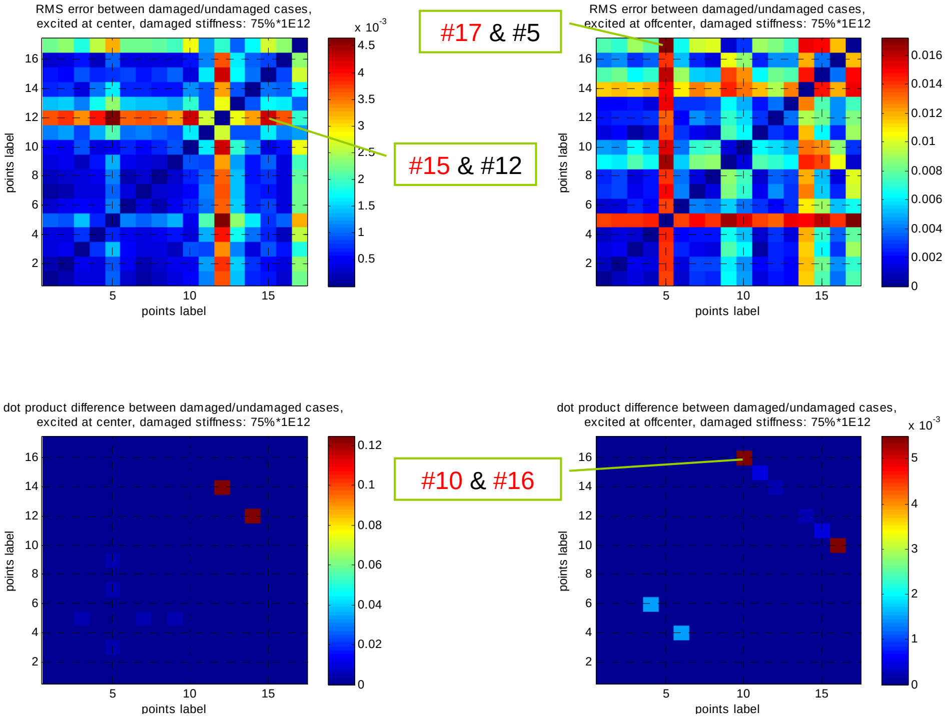

Figure 2-12: error maps for 75% stiffness retention

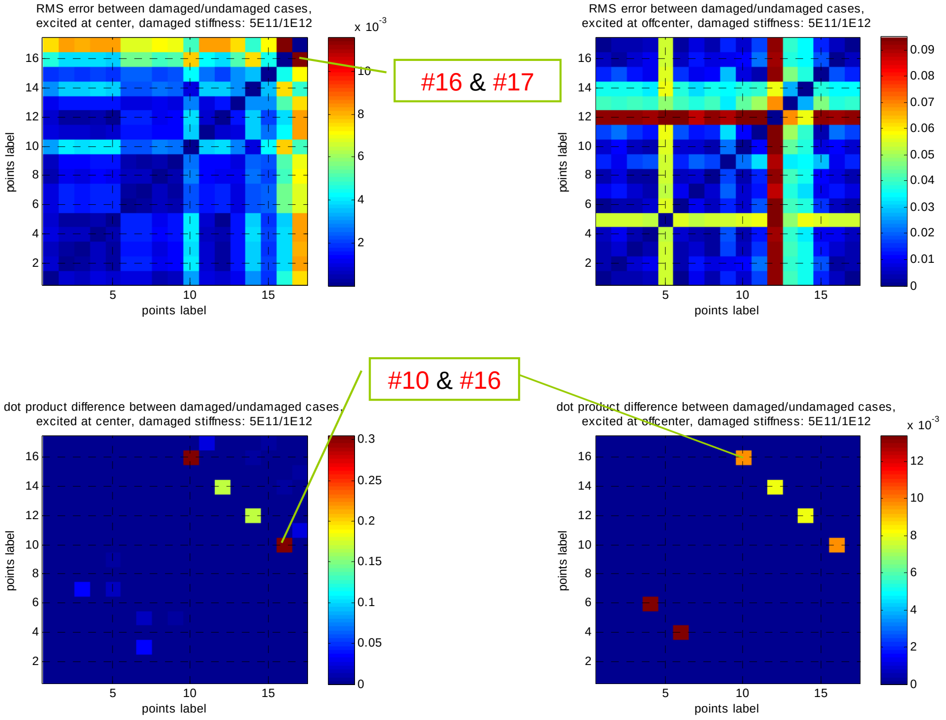

Figure 2-13: error maps for 50% stiffness retention

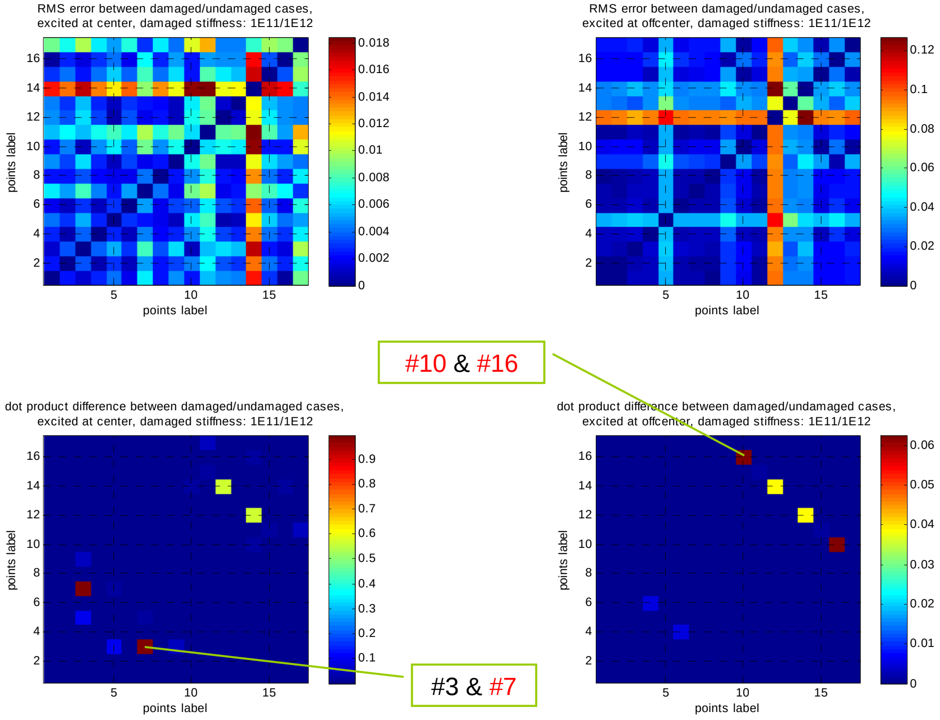

Figure 2-14: error maps for 10% stiffness retention

2.4 Transmissibility and FRF Estimation

2.4.1. Background

In the past section, the feasibility of damage occurence detection and localization has been shown via two transmissibility-based features we defined, namely *RMSD* and *DPD*. The transmissibility evaluations, for illustration purpose, are directly from responses calculated from FE model with ideal impact excitation, in which case all test results can be regarded as "true value".

However, broad-band random excitations are more often used in real experiments, and in this case with stationary implementations, various ways of calculations are used to compute the FRF and transmissibility; while the rigorous definitions given by Equations (2-1) and (2-2) give simple ideas but not practical and accurate evaluations. Those various estimation algorithms, often called estimators, differently reflect all the uncertainties from imperfect experimental conditions, limited-band input, sampled measurement records, and imprecise calculation, and should be accordingly selection based upon the actual implemental conditions.

2.4.2. Formulation of Estimators

Considering a more realistic data flow, compare to Figure 2-8, noise terms are included in a SIMO model shown in Figure 2-15. In this updated model, $m(t)$ and $n_i(t)$, $n_j(t)$ are the external noise contaminated in real measurements $x(t)$ and $y_i(t)$, $y_j(t)$.

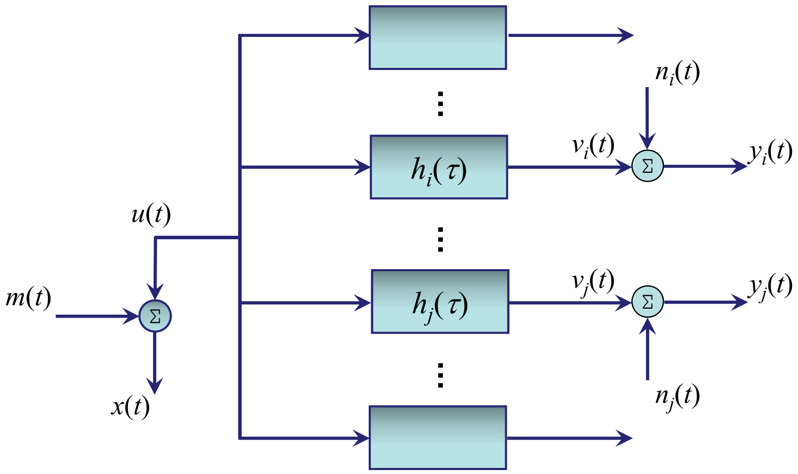

Figure 2-15: SIMO data flow model

According to the more general data flow in Figure 2-15, Equations (2-1) and (2-2) are updated as:

$$H_{i,j}(\omega) = \frac{V_{i,j}(\omega)}{U(\omega)} = \frac{\mathcal{F}\left[y_{i,j}(t) - n_{i,j}(t)\right]}{\mathcal{F}\left[x(t) - m(t)\right]}, \tag{2-6}$$

and $$T_{ij}(\omega) = \frac{V_i(\omega)}{V_j(\omega)} = \frac{\mathcal{F}\left[y_i(t) - n_i(t)\right]}{\mathcal{F}\left[y_j(t) - n_j(t)\right]}. \tag{2-7}$$

Because the true input and output $u(t)$ and $v(t)$ and their Fourier transforms are never approachable, spectral techniques are used to estimate transfer functions more robustly in order to eliminate the uncertainty influence, which has been mentioned in last section.

These estimators include, but not limited to, the H1 and H2 estimators for FRF:

$$\hat{H}(\omega)=\frac{\hat{G}_{xy}(\omega)}{\hat{G}_{xx}(\omega)}=\frac{\hat{G}_{yy}(\omega)}{\hat{G}_{yx}(\omega)}, \tag{2-8}$$

and estimators for transmssibility:

$$\hat{T}_{ij}(\omega)=\frac{\hat{G}_{xy_i}(\omega)}{\hat{G}_{xy_j}(\omega)}, \tag{2-9}$$

$$\hat{T}_{ij}(\omega)=\frac{\hat{G}_{xy_i}(\omega)\big/\hat{G}_{xx}(\omega)}{\hat{G}_{xy_j}(\omega)\big/\hat{G}_{xx}(\omega)}=\frac{\hat{H}_i(\omega)}{\hat{H}_j(\omega)}, \tag{2-10}$$

$$\left|\hat{T}_{ij}(\omega)\right|=\sqrt{\frac{\hat{G}_{y_iy_i}(\omega)}{\hat{G}_{y_jy_j}(\omega)}}, \tag{2-11}$$

$\hat{G}_{xy}$, $\hat{H}$ and $\hat{T}\in\mathbb{C}$, and $\hat{G}_{xx}$, $\hat{G}_{yy}\in\mathbb{R}^+$, $\forall i$ or j. The ˆ sign denotes the spectral estimation instead of the true value itself, and $\hat{G}_{xx}$, $\hat{G}_{xy}$, $\hat{G}_{yx}$ and $\hat{G}_{yy}$ are the auto and cross power density estimations between corresponding input $x(t)$ and output measurement $y(t)$ corrupted by noise.

Welch proposes an averaging algorithm [92], which has become a standard implementation for real applications, to enhance the quality of spectral estimations. In this method, the original time series are split into n_d segments, and the Fourier Transform of each segment is calculated and averaged, therefore a smoother estimation will be achieved. Equation (2-12) illustrates how $\hat{G}_{xy}$ is estimated via Welch's algorithm as an example:

$$\hat{G}_{xy}(\omega) = \frac{1}{n_d} \sum_{k=1}^{n_d} \tilde{X}_k^*(\omega) \cdot \tilde{Y}_k(\omega), \tag{2-12}$$

where the $\tilde{}$ sign denotes the Fourier Transform of each single segment and * indicates the complex conjugate. It is necessary to point out that if noise is independent from either system input or output and nd is sufficiently big, the cross power density function estimations $\hat{G}_{xy}$ and $\hat{G}_{yx}$ will converge to the true value of G_{uv} and G_{vu}, but the auto power densities will not. Equation (2-13) addresses this issue mathematically using $\hat{G}_{xx}$ and $\hat{G}_{xy}$ as example [79]:

$$\begin{gathered} \hat{G}_{xx} = \hat{G}_{uu} + \hat{G}_{mu} + \hat{G}_{um} + \hat{G}_{mm} \rightarrow G_{uu} + G_{mm} \\ \hat{G}_{xy} = \hat{G}_{uv} + \hat{G}_{mv} + \hat{G}_{un} + \hat{G}_{mn} \rightarrow G_{uv} \end{gathered} . \tag{2-13}$$

Reconsidering the data flow in Figure 2-15, noise terms *m* and *n* are independent from each other and also independent from both input *u* and output *v*, therefore the cross power between these corresponding series approach zero if the number of averages is large enough. As a consequence, the H1 and H2 estimators in Equation (2-8) are both biased, and under/overestimate FRF respectively, for which people should find a suitable estimator by comparing the noise conditions on input and output channels to get a more accurate auto power density and subsequently more accurate frequency response estimations.

For transmissibility estimators given by Equations (2-9) and (2-10), they are both unbiased estimations; but for estimator in Equation (2-11), the auto-powers for noise cannot be ignored therefore it is a biased estimator since the expected value of the noise-contaminated form does not converge to the expected value of the noise-free form $\sqrt{G_{v_iv_i}/G_{v_jv_j}}$. However, if the second order series expansion is considered:

$$\frac{\hat{G}_{y_iy_i}}{\hat{G}_{y_jy_j}} = \frac{\hat{G}_{v_iv_i} + \hat{G}_{n_in_i}}{\hat{G}_{v_jv_j} + \hat{G}_{n_jn_j}} = \frac{\hat{G}_{v_iv_i}(1+\epsilon_i)}{\hat{G}_{v_jv_j}(1+\epsilon_j)} \approx \frac{\hat{G}_{v_iv_i}}{\hat{G}_{v_jv_j}}\left(1+\epsilon_i-\epsilon_j-\epsilon_i\epsilon_j+\epsilon_j^2\right), \qquad (2\text{-}14)$$

where $\epsilon = \hat{G}_{nn} / \hat{G}_{vv}$ and has the physical meaning of noise-to-signal ratio (*NSR*), or the reciprocal of signal-to-noise ratio (*SNR*), which is the more usual metric. For the conditions with light noise contamination, i.e. small ϵ_i and ϵ_j, or close enough *SNR* on each channel, the estimator in Equation (2-11) may be regarded approximately as an unbiased estimation.

Dealing with different transmissibility estimators, the estimator in Equation (2-10) relates FRFs from two single channels with transmissibility, and in other words, transmissibility can be not only estimated through data-based FRF estimations but also FRFs obtained from FE modeling. For some situations where input time series are not available, estimator in Equation (2-11) is compatible to conditions with output-only data, which is very useful for online assessment.

A portion of this chapter has been published in *Proc. SPIE 7650*, Zhu Mao and Michael

Todd, 2010. The title of this paper is “A structural transmissibility measurements-based approach for system damage detection”. The dissertation author was the primary investigator and author of this paper. The fourth section of this chapter, in part, has been published in *Mechanical Systems and Signal Processing*, Zhu Mao and Michael Todd, 2012. The title of this paper is “A model for quantifying uncertainty in the estimation of noise-contaminated measurements of transmissibility”. The dissertation author was the primary investigator and author of this paper.

3. Statistical Modeling for Uncertainty Quantification

This chapter proposes statistical models to quantify uncertainty of transmissibility and FRF estimations, for both magnitude and phase. Different approaches are adopted, suiting to different estimators. Equation (3-17) gives the variance of transmissibility magnitude estimations via perturbation. Equation (3-20) gives the PDF of auto-power density estimations, and Equation (3-28) gives PDF of transmissibility magnitude estimation estimated by auto-power densities, via a Chi-square bivariate approach. Equation (3-33) and (3-36) provide the PDFs of transmissibility and FRF magnitude estimations, and Equation (3-44) and (3-46) provide the PDFs of transmissibility and FRF phase estimations, and all four models are derived via Gaussian bivariate approach with different variable transformations.

3.1. Overview of uncertainty accumulation and statistical modeling

Figure 3-1 illustrates how transfer functions, especially for the estimation algorithms introduced in Chapter 2, are estimated and uncertainties accumulated step by step. Usually for engineering problems involved with signal processing, the input and output are measured/quantized with specific precision and sampled into discrete time domain, literally called digitization. Subject to sources of environmental and operational variability, digitized signals $u(k)$ and $v(k)$ will be always contaminated by noise $m(k)$ and $n(k)$, and this contaminated input and output series $x(k)$ and $y(k)$ are the start point for any kind of post signal processing. Particularly for transmissibility and FRF estimations in this work, the contaminated data are being Fourier transformed and Welch averaged, until getting estimated via certain estimator, which also brings extra uncertainty to the process.

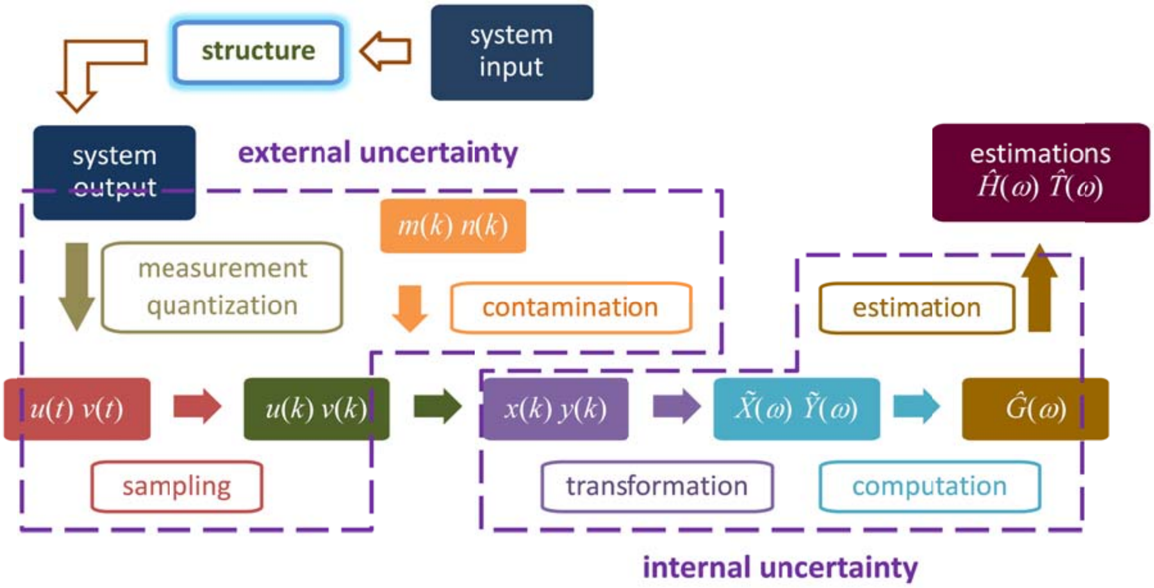

Figure 3-1: flow of uncertainty generation and accumulation

In other words, this dissertation classifies the uncertainty of data-based transfer function estimation into two groups: *external uncertainty* from a non-deterministic test environment, and *internal uncertainty* from inaccuracies in the estimation algorithm and computational errors.

Uncertainty quantification (UQ) is rooted modeling the estimation process as a random variable in order to obtain order statistics, or, if possible, a probability density function, from which any statistical order and other statistical properties are all derived. The primary result is that the accuracy of the estimation process may be quantified, given by the variance and/or significance level, which facilitates better understanding of system identification results in a way that facilitates quantitative decision-making. As an example central to this work, proper quantification of transmissibility estimation from a test establishes, through confidence bounds, statistically-sound hypothesis testing when using the estimations to determine the presence and/or location of damage.

For real vibration-based system identification implementations, Gaussian white noise is often used as excitation to stimulate structure for its stationary, broadband frequency characteristics. The Gaussian nature will be preserved when the input is passed through any linear process (the structure itself, a Fourier transform, etc.); this is an example of internal uncertainty. For external uncertainty, it is feasible to assume that other corrupting influences (“noise”) may also be modeled as Gaussian (though not necessarily correlated to the excitation) because many sources of uncertainty are, indeed, Gaussian or near-Gaussian, and under central limit theorem arguments, their superposition could be expected to converge to Gaussian. Therefore, in the next two sections, uncertainty propagation of transmissibility and FRF estimations will be computed considering the inherent Gaussian nature of the underlying uncertainty.

In the following sections, magnitude and phase uncertainty of transmissibility and the traditional FRF will be modeled through different statistical approaches. Representative estimators are adopted for the purpose of illustrating modeling processes and validating their applicability. Three quantification models are proposed in section 3.2 for transfer function magnitude estimations, namely perturbation, Chi-square bivariate and Gaussian bivariate approaches. Perturbation approach in 3.2.1 gives uncertainty bounds with respect to variance and the other two in 3.2.2 and 3.2.3 supply a full characterization of probability density functions. In section 3.3, phase estimations are studied and probability density function of phase estimations are derived via two-dimensional Gaussian distribution.

3.2. Magnitude uncertainty

3.2.1. Perturbation approach

By means of linear perturbation, Bendat and Piersol derived standard deviation of FRF magnitude estimations obtained from a single-input/single-output (SISO) model with noise-free input [79-81]. Following the same idea, standard deviation of transmissibility is derived in this section, where Bendat and Piersol's model is extended for transmissibility uncertainty modeling. Recall the SIMO signal model in Figure 2-15, a reshaped structure connecting both responses at location *i* and *j* with a new equivalent SISO flow is shown in Figure 3-2, and according to the optimized channel assumption in [79-81], where noise power densities are minimized in measurements, there will be two coinstantaneous relations:

$$G_{n_i n_i} = \left(1-\gamma^2_{v_j y_i}\right) G_{y_i y_i} \quad \text{and} \quad G_{n_j n_j} = \left(1-\gamma^2_{v_i y_j}\right) G_{y_j y_j} \,. \tag{3-1}$$

in which $\gamma^2_{v_j y_i}$ and $\gamma^2_{v_i y_j}$ are the coherence functions between corresponding series shown in Figure 3-2.

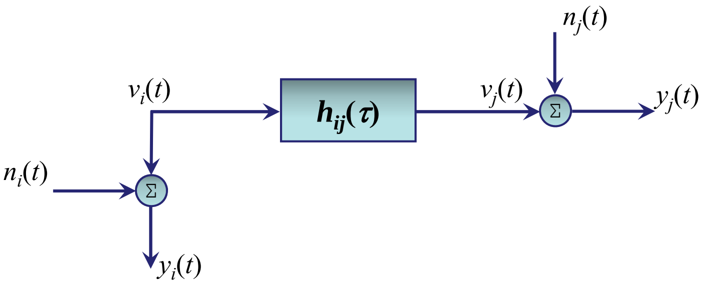

Figure 3-2: transformed data flow for transmissibility

In the new data flow shown in Figure 3-2, output measurements y_i and y_j are regarded as input and output of each other, with transmissibility h_{ij} connecting them. Since noise can appear independently on both response locations, noise must be included on both variables independently. In the signal flow model of Figure 3-2, this section aims to establish an analytical formula in which the uncertainty of transmissibility h_{ij} may be characterized, given noisy measurements y_i and y_j.

Firstly, consider the reformed estimator in Equation 2-11, and the theoretical relation holds:

$$G_{v_i v_i} = \left|T_{ij}\right|^2 G_{v_j v_j} , \tag{3-2}$$

with regard to auto-power density function of noise-free responses v_i and v_j, since the actual input excitation u and noisy measurement x is eliminated in this transmissibility case.

Taking differential increment of Equation (3-2), there will be:

$$\Delta G_{v_i v_i} = \Delta\left|T_{ij}\right|^2 G_{v_j v_j} + \left|T_{ij}\right|^2 \Delta G_{v_j v_j} , \tag{3-3}$$

where the Δ operator means the difference between an estimate of a quantity (the same convention as Equation 2-12, indicated by ˆ over the quantity) and the quantity itself, e.g., $\Delta\left|T_{ij}\right|^2 = \left|\hat{T}_{ij}\right|^2 - \left|T_{ij}\right|^2$, and so forth.

Then, square both sides of $\Delta\left|T_{ij}\right|^2 G_{v_j v_j} = \Delta G_{v_i v_i} - \left|T_{ij}\right|^2 \Delta G_{v_j v_j}$, which is the equivalent form of Equation (3-3), there will be:

$$G_{v_j v_j}^2 \left(\Delta\left|T_{ij}\right|^2\right)^2 = \left(\Delta T_{v_i v_i}\right)^2 - 2\Delta G_{v_i v_i} \Delta G_{v_j v_j} \left|T_{ij}\right|^2 + \left(\Delta G_{v_j v_j}\right)^2 \left|T_{ij}\right|^4 , \tag{3-4}$$

and take expectation operation $\mathrm{E}\left[\cdot\right]$ on both sides of Equation (3-4), there will be:

$$G_{v_j v_j}^2 \,\mathrm{E}\left[\left(\Delta\left|T_{ij}\right|^2\right)^2\right] = \mathrm{E}\left[\left(\Delta G_{v_i v_i}\right)^2\right] - 2\left|T_{ij}\right|^2 \mathrm{E}\left[\Delta G_{v_i v_i} \Delta G_{v_j v_j}\right] + \left|T_{ij}\right|^4 \mathrm{E}\left[\left(\Delta G_{v_j v_j}\right)^2\right] . \tag{3-5}$$

Consider the definitions of order statistics, variance and covariance, which are

$\mathrm{var}\left[\hat{\phi}\right]=\mathrm{E}\left[\left(\hat{\phi}-\phi\right)^2\right]=\mathrm{E}\left[\left(\Delta\phi\right)^2\right]$ and $\mathrm{cov}\left[\hat{\phi}_i,\hat{\phi}_j\right]=\mathrm{E}\left[\left(\hat{\phi}_i-\phi_i\right)\left(\hat{\phi}_j-\phi_j\right)\right]=\mathrm{E}\left[\Delta\phi_i\Delta\phi_j\right]$, Equation (3-5) can be updated as:

$$G_{v_jv_j}^2\ \mathrm{var}\left[\left|\hat{T}_{ij}\right|^2\right]=\mathrm{var}\left[\hat{G}_{v_iv_i}\right]-2\left|T_{ij}\right|^2\mathrm{cov}\left[\hat{G}_{v_iv_i},\hat{G}_{v_jv_j}\right]+\left|T_{ij}\right|^4\mathrm{var}\left[\hat{G}_{v_jv_j}\right], \tag{3-6}$$

in which variance and covariance of auto power densities are given by Reference [79], and n_d is number of averages:

$$\mathrm{var}\left[\hat{G}_{y_iy_i}\right]=G_{y_iy_i}\Big/n_d \ \text{ and } \ \mathrm{var}\left[\hat{G}_{v_iv_i}\right]=\left(G_{y_iy_i}^2-\left(1-\gamma_{v_jy_i}^2\right)^2G_{y_iy_i}^2\right)\Big/n_d\ ;$$

$$\mathrm{var}\left[\hat{G}_{y_jy_j}\right]=G_{y_jy_j}\Big/n_d \ \text{ and } \ \mathrm{var}\left[\hat{G}_{v_jv_j}\right]=\left(G_{y_jy_j}^2-\left(1-\gamma_{v_iy_j}^2\right)^2G_{y_jy_j}^2\right)\Big/n_d\ ;$$

$$\text{and } \ \mathrm{cov}\left[\hat{G}_{v_iv_i},\hat{G}_{v_jv_j}\right]=\frac{1}{n_d}\left|G_{v_iv_j}\right|^2=G_{v_iv_i}G_{v_jv_j}\Big/n_d\ .$$

Substitute all the terms back to Equation (3-6), replace $G_{y_iy_i}$ and $G_{y_jy_j}$ with $G_{v_iv_i}\big/\gamma_{v_jy_i}^2$ and $G_{v_jv_j}\big/\gamma_{v_iy_j}^2$, and divide both sides by $G_{v_iv_i}$, there is:

$$\mathrm{var}\left[\left|\hat{T}_{ij}\right|^2\right]=\frac{1}{n_d}\frac{\left(2-\gamma_{v_iy_j}^2\right)}{\gamma_{v_iy_j}^2}\frac{G_{y_iy_i}^2}{G_{y_jy_j}^2}-\frac{2}{n_d}\left|T_{ij}\right|^2\frac{G_{v_iv_i}}{G_{v_jv_j}}+\frac{1}{n_d}\left|T_{ij}\right|^4\frac{\left(2-\gamma_{v_jy_i}^2\right)}{\gamma_{v_jy_i}^2}\ . \tag{3-7}$$

In Equation (3-7), term $G_{v_iv_i}\big/G_{v_jv_j}$ can be replaced by $\left|T_{ij}\right|^2$ according to Equation (3-2), and therefore, the variance of magnitude square yields to:

$$\mathrm{var}\left[\left|\hat{T}_{ij}\right|^2\right]=\frac{2\left(\gamma_{v_iy_j}^2+\gamma_{v_jy_i}^2-2\gamma_{v_iy_j}^2\gamma_{v_jy_i}^2\right)}{n_d\gamma_{v_iy_j}^2\gamma_{v_jy_i}^2}\left|T_{ij}\right|^4\ . \tag{3-8}$$

To get the variance of magnitude, consider the following derivation with notation ϕ

representing any random variable:

$$\Delta\phi^2 = \hat{\phi}^2 - \phi^2 = (\phi + \Delta\phi)^2 - \phi^2 = 2\phi\Delta\phi + (\Delta\phi)^2 .$$

Proceeding by squaring the expression and taking the expectation on both sides:

$$(\Delta\phi^2)^2 = 4\phi^2 (\Delta\phi)^2 + 4\phi(\Delta\phi)^3 + (\Delta\phi)^4 ,$$

$$\Rightarrow \mathrm{E}\left[(\Delta\phi^2)^2\right] = 4\phi^2\, \mathrm{E}\left[(\Delta\phi)^2\right] + 4\phi\mathrm{E}\left[(\Delta\phi)^3\right] + \mathrm{E}\left[(\Delta\phi)^4\right],$$

$$\Rightarrow \mathrm{E}^2\left[\Delta\phi^2\right] + \mathrm{var}\left[\Delta\phi^2\right] = 4\phi^2\, \mathrm{var}\left[\hat{\phi}\right] + 4\phi\mathrm{E}\left[(\Delta\phi)^3\right] + \mathrm{E}\left[(\Delta\phi)^4\right], \tag{3-9}$$

while $\mathrm{E}\left[\Delta\phi^2\right] = \mathrm{E}\left[\hat{\phi}^2\right] - \phi^2 = \mathrm{var}\left[\hat{\phi}\right]$ and $\mathrm{var}\left[\Delta\phi^2\right] = \mathrm{var}\left[\hat{\phi}^2 - \phi^2\right] = \mathrm{var}\left[\hat{\phi}^2\right]$, and assume $\Delta\phi$ is zero mean Gaussian random variable, the third and fourth moment in Equation (3-9) will be 0 and $3\,\mathrm{var}^2\left[\hat{\phi}\right]$ respectively [93], then substitute these equations back into Equation (3-9), it yields to:

$$2\,\mathrm{var}^2\left[\hat{\phi}\right] + 4\phi^2\, \mathrm{var}\left[\hat{\phi}\right] - \mathrm{var}\left[\hat{\phi}^2\right] = 0 . \tag{3-10}$$

The positive solution of $\mathrm{var}\left[\hat{\phi}\right]$ in Equation (3-10) is:

$$\mathrm{var}\left[\hat{\phi}\right] = -\phi^2 + \sqrt{\phi^4 + \frac{1}{2}\mathrm{var}\left[\hat{\phi}^2\right]} , \tag{3-11}$$

and if $\mathrm{var}\left[\hat{\phi}^2\right]$ is small, a first order approximation of Equation (3-11) is available, which has a simpler form:

$$\mathrm{var}\left[\hat{\phi}\right] \approx \frac{\mathrm{var}\left[\hat{\phi}^2\right]}{4\phi^2}. \tag{3-12}$$

Apply the calculation in Equation (3-12) to (3-8), and the variance of $\left|\hat{T}_{ij}\right|$ will be:

$$\mathrm{var}\left[\left|\hat{T}_{ij}\right|\right] = \frac{\gamma^2_{v_i y_j} + \gamma^2_{v_j y_i} - 2\gamma^2_{v_i y_j}\gamma^2_{v_j y_i}}{2n_d \gamma^2_{v_i y_j}\gamma^2_{v_j y_i}} \left|T_{ij}\right|^2. \tag{3-13}$$

If noise on either side is zero, i.e., either $\gamma^2_{v_i y_j}$ or $\gamma^2_{v_j y_i}$ is equal to one, Equation (3-13) will be reduced to the model presented in Reference [79-81], which is used to quantize uncertainty of FRF magnitude without input noise.

As Equation (2-14) illustrates, the estimator in this model is biased, according to Equation (3-1):

$$\frac{G_{y_i y_i}}{G_{y_j y_j}} = \frac{G_{v_i v_i} \big/ \gamma^2_{v_j y_i}}{G_{v_j v_j} \big/ \gamma^2_{v_i y_j}} = \frac{\gamma^2_{v_i y_j}}{\gamma^2_{v_j y_i}} T_{ij}, \tag{3-14}$$

indicating that the estimator has a bias coefficient $\gamma^2_{v_i y_j} \big/ \gamma^2_{v_j y_i}$, compared to the true T_{ij}.

However, in reality, the coherence functions in Equation (3-13) and (3-14) are not available, since v_i and v_j are not measurable. Therefore further modeling is needed to achieve coherence information. Consider the H1 and H2 estimators for input-output transfer function (FRF) in Equation (2-8), the definition should be equal without input noise in the auto power density terms, thus:

$$\frac{G_{y_i y_j}}{G_{v_i v_i}} = \frac{G_{v_j v_j}}{G_{y_j y_i}} .$$

Substitute Equation (3-1), there is:

$$\frac{G_{y_i y_j}}{\gamma^2_{v_j y_i} G_{y_i y_i}} = \frac{\gamma^2_{v_i y_j} G_{y_j y_j}}{G_{y_j y_i}} ,$$

which is identical to:

$$\gamma^2_{v_j y_i} \gamma^2_{v_i y_j} = \frac{G_{y_i y_j} G_{y_j y_i}}{G_{y_i y_i} G_{y_j y_j}} = \frac{\left| G_{y_i y_j} \right|^2}{G_{y_i y_i} G_{y_j y_j}} = \gamma^2_{y_i y_j} . \tag{3-15}$$

Equation (3-15) relates the two unknown coherences $\gamma^2_{v_i y_j}$ and $\gamma^2_{v_j y_i}$ with the coherence of two measurable contaminated series y_i and y_j. In order to get Equation (3-13) and (3-14) compatible with contaminated data, a further assumption is made in Equation (3-16) that the two input-output channels should be "balanced":

$$\gamma^2_{v_j y_i} = \gamma^2_{v_i y_j} = \sqrt{\gamma^2_{y_i y_j}} . \tag{3-16}$$

Once this assumption is made, the random error of transmissibility magnitude estimation can be described with its variance:

$$\operatorname{var}\left[\left| \hat{T}_{ij} \right| \right] = \frac{1 - \sqrt{\gamma^2_{y_i y_j}}}{n_d \sqrt{\gamma^2_{y_i y_j}}} \left| T_{ij} \right|^2 , \tag{3-17}$$

and the bias error is negligible thereafter.

3.2.2. Chi-square Bivariate approach

Instead of quantifying uncertainty with order statistics, this approach considers the estimator in Equation (2-11), in which auto-power densities of two responses are involved, as listed again:

$$\left|\hat{T}_{ij}(\omega)\right| = \sqrt{\frac{\hat{G}_{y_i y_i}(\omega)}{\hat{G}_{y_j y_j}(\omega)}}\ .$$

For a stationary Gaussian random input process (denoted by *x*), the exact output *v* will be also Gaussian for a linear system. Even if the input random series is not Gaussian, the output *v*, which are the convolution of input series with structure impulse response, will converge to Gaussian due to averaging under the central limit theorem. Therefore, the smooth output auto-power spectrum estimation $\hat{G}_{vv}$ will follow a Chi-square distribution fluctuating around the true value G_{vv} [93], and the estimation satisfies Equation (3-18) where $\chi^2_{2n_d}$ represents a Chi-square distributed random variable with $2n_d$ degrees-of-freedom, and n_d has been pointed out being the number of averaging times in Welch's smooth power spectrum estimation:

$$\hat{G}_{vv} = \frac{\chi^2_{2n_d}}{2n_d} G_{vv}\,, \tag{3-18}$$

where n_d is an integer. Therefore, the transmissibility estimation according to Equation (2-11) is the square root of the ratio between two (perhaps correlated) Chi-square distributed random variables.

For the situation where measurements are subject to extraneous noise or other sorts of environmental and operational variability, like the condition in Figure 2-15, the auto-power spectrum estimation is also Chi-square distributed under the assumption of independent Gaussian noise characteristics, as shown in Equation (3-19):

$$\hat{G}_{yy} = \frac{\chi^2_{2n_d}}{2n_d} G_{yy} = \frac{\chi^2_{2n_d}}{2n_d}\left(1+\frac{1}{SNR}\right) G_{vv}, \tag{3-19}$$

where the signal-to-noise ratio $SNR = G_{vv} / G_{nn}$ is defined in the same way as before. Compared to Equation (3-18), there is a scaling factor with *SNR* involved, and this shows more clearly (than Equation (2-14)) that when the signal-to-noise ratios at both measurement DOFs i and j are nearly equal or the *SNR* of each channel is very small, the noise terms in transmissibility estimator in Equation (2-11) are negligible, and the transmissibility estimation is approximately unbiased, as previously stated.

The probability density function $p_{\chi^2}(z)$ of a Chi-square distributed variable z with $2n_d$ degrees-of-freedom may be expressed as [93]:

$$p_{\chi^2}(z; 2n_d) = \frac{z^{n_d - 1} \cdot \mathrm{e}^{-\frac{z}{2}}}{2^{n_d} \cdot \Gamma\left(n_d\right)}, \tag{3-20}$$

where $\Gamma(\cdot)$ is the Gamma function. As an outgrowth, Equation (3-20) can be used to quantify the uncertainty of auto-power spectra estimation for any Gaussian time series with n_d times of averages.

Consider the summation of the magnitude square of complex $\tilde{Y}_i$ and $\tilde{Y}_j$, which are the Fourier transform of each round of measurements y_i and y_j in Figure 2-15, the argument I_i shown in Equation (3-21) is equal to n_d times of the auto-power density estimation $\hat{G}_{y_i y_i}$:

$$I_i = \sum_{k=1}^{n_d} \left(\tilde{Y}_{iR,k}^2 + \tilde{Y}_{iI,k}^2 \right) = n_d \hat{G}_{y_i y_i}\,, \tag{3-21}$$

where $\tilde{Y}_i = \tilde{Y}_{iR} + \mathbf{i}\tilde{Y}_{iI} \in \mathbb{C}$ ($\mathbf{i}=\sqrt{-1}$) and $\tilde{Y}_{iR} = \Re\left[\tilde{Y}_i\right], \tilde{Y}_{iI} = \Im\left[\tilde{Y}_i\right]$, and the same relationship for measurements at position j. The covariance matrix $\mathbf{C} = \mathrm{E}\left[[\tilde{Y}_{iR}, \tilde{Y}_{iI}, \tilde{Y}_{jR}, \tilde{Y}_{jI}]^{\mathrm{T}}\ [\tilde{Y}_{iR}, \tilde{Y}_{iI}, \tilde{Y}_{jR}, \tilde{Y}_{jI}] \right]$ takes the form in Equation (3-22), where the subscripts $_A$ and $_C$ in the covariance terms ${}_A c_{Y_i Y_j}^2$ and ${}_C c_{Y_i Y_j}^2$ represent auto- and cross- with respect to the real and imaginary parts of $\tilde{Y}_i$ and $\tilde{Y}_j$ [94]:

$$\mathbf{C} = \begin{bmatrix} \sigma_{Y_i}^2 & 0 & {}_A c_{Y_i Y_j}^2 & -{}_C c_{Y_i Y_j}^2 \\ 0 & \sigma_{Y_i}^2 & {}_C c_{Y_i Y_j}^2 & {}_A c_{Y_i Y_j}^2 \\ {}_A c_{Y_i Y_j}^2 & {}_C c_{Y_i Y_j}^2 & \sigma_{Y_j}^2 & 0 \\ -{}_C c_{Y_i Y_j}^2 & {}_A c_{Y_i Y_j}^2 & 0 & \sigma_{Y_j}^2 \end{bmatrix}. \tag{3-22}$$

According to Reference [94], the joint probability density function $p_I\left(I_i, I_j\right)$ of arguments I_i and I_j illustrated in Equation (3-21) can be rewritten as Equation (3-23), with the covariance terms in Equation (3-22) involved:

$$\begin{aligned} p_I\left(I_i,I_j\right) = & \frac{\exp\left(-\dfrac{\sigma_{Y_j}^2 I_i + \sigma_{Y_i}^2 I_j}{2\left(\sigma_{Y_i}^2\sigma_{Y_j}^2 - {}_A c_{Y_iY_j}^2 - {}_C c_{Y_iY_j}^2\right)}\right)\cdot\left(I_i I_j\right)^{\frac{n_d-1}{2}}}{2^{n_d+1}\cdot\left(\sigma_{Y_i}^2\sigma_{Y_j}^2 - {}_A c_{Y_iY_j}^2 - {}_C c_{Y_iY_j}^2\right)\cdot\left({}_A c_{Y_iY_j}^2 + {}_C c_{Y_iY_j}^2\right)^{\frac{n_d-1}{2}}\cdot\Gamma\left(n_d\right)} \\ & \times \mathrm{I}_{n_d-1}\left(\frac{\sqrt{\left({}_A c_{Y_iY_j}^2 + {}_C c_{Y_iY_j}^2\right) I_i I_j}}{\sigma_{Y_i}^2\sigma_{Y_j}^2 - {}_A c_{Y_iY_j}^2 - {}_C c_{Y_iY_j}^2}\right) \end{aligned}, \tag{3-23}$$

where $\mathrm{I}_{n_d-1}\left(\cdot\right)$ denotes the modified Bessel function of the first kind.

Given the joint probability density function $p_I\left(\cdot,\cdot\right)$ of two Chi-square arguments shown in Equation (3-23), the the distribution of their ratio λ can be derived, expressed as the probability density function $p_{ratio}\left(\cdot\right)$:

$$p_{ratio}\left(\lambda\right) = \frac{d}{d\lambda}\left(\mathrm{Prob}\left(\frac{I_i}{I_j} < \lambda\right)\right) = \frac{d}{d\lambda}\left(\iint_{\frac{I_i}{I_j}<\lambda} p_I\left(I_i,I_j\right) dI_i dI_j\right),$$

$$\Rightarrow p_{ratio}\left(\lambda\right) = \frac{d}{d\lambda}\left(\int_{-\infty}^{0}\int_{\lambda I_j}^{+\infty} p_I\left(I_i,I_j\right) dI_i dI_j + \int_{0}^{+\infty}\int_{-\infty}^{\lambda I_j} p_I\left(I_i,I_j\right) dI_i dI_j\right). \tag{3-24}$$

Denote function $Q\left(I_i,I_j\right)$ as the indefinite integral $\int p_I\left(I_i,I_j\right) dI_i$, and therefore the derivative $\frac{\partial}{\partial I_i} Q\left(I_i,I_j\right) = p_I\left(I_i,I_j\right)$. The definite integrals in Equation (3-24) can then be expressed as:

$$Q_-\left(I_j\right) = \int_{\lambda I_j}^{+\infty} p_I\left(I_i,I_j\right) dI_i = Q\left(I_i,I_j\right)\Big|_{I_i=\lambda I_j}^{+\infty} \quad \text{and} \quad Q_+\left(I_j\right) = \int_{-\infty}^{\lambda I_j} p_I\left(I_i,I_j\right) dI_i = Q\left(I_i,I_j\right)\Big|_{I_i=-\infty}^{\lambda I_j}. \tag{3-25}$$

Because the probability density function $p_I(\cdot,\cdot)$ converges to zero at ±∞, the two integrals $Q_{\mp}(I_j)$ in Equation (3-25) are simplified to $\mp Q(\lambda I_j, I_j)$. Change the sequence of differential and integral, Equation (3-24) is updated to:

$$\begin{aligned} p_{ratio}(\lambda) &= \int_{-\infty}^{0} \frac{d}{d\lambda}\left(-Q\left(\lambda I_j, I_j\right)\right) dI_j + \int_{0}^{+\infty} \frac{d}{d\lambda}\left(Q\left(\lambda I_j, I_j\right)\right) dI_j \\ &= -\int_{-\infty}^{0} I_j \cdot p_I\left(\lambda I_j, I_j\right) dI_j + \int_{0}^{+\infty} I_j \cdot p_I\left(\lambda I_j, I_j\right) dI_j \end{aligned} ,$$

$$\Rightarrow p_{ratio}(\lambda) = \int_{-\infty}^{+\infty} \left|I_j\right| \cdot p_I\left(\lambda I_j, I_j\right) dI_j \,. \tag{3-26}$$

Considering the magnitude of transmissibility estimation is the square root of the above-mentioned ratio, another transformation via change-of-variable is required. For a continuous random variable λ whose probability density function is $p_{ratio}(\lambda)$, define a square root transformation $\Psi : \lambda \to u$, and denote the probability density function of u as $p_{sqrt}(u)$. Because of the equal probability on both side of Ψ, the relationship of $p_{sqrt}(u) \cdot |du| = p_{ratio}(\lambda) \cdot |d\lambda|$ holds, and replace variable λ with u^2, then the probability density relationship between λ and its square root u is:

$$p_{sqrt}(u) = \left|\frac{d\left(u^2\right)}{du}\right| p_{ratio}\left(u^2\right) = 2u \cdot p_{ratio}\left(u^2\right). \tag{3-27}$$

where $u \in \mathbb{R}^+$.

By substituting the joint probability density function in Equation (3-23) into the transformations in Equation (3-26) and (3-27), it will arrive at the final closed form of $p_{sqrt}\left(\cdot\right)$, which exactly describes the statistics of transmissibility estimations in Equation (2-11), subject to a Gaussian random process. Equation (3-28) renames the function derived from Equation (3-27) to $p_t\left(\cdot\right)$, and shows the probability density function of the transmissibility magnitude estimation with respect to variable $\hat{T}$:

$$p_t(\hat{T}) = \frac{2^{2n_d}\,\hat{T}^{(2n_d-1)}\left(\left(1-\rho^2\right)\sigma_{Y_i}^2\sigma_{Y_j}^2\right)^{n_d}\Gamma\left(n_d+\frac{1}{2}\right)}{\sqrt{\pi}\left(\sigma_{Y_i}^2+\hat{T}^2\sigma_{Y_j}^2\right)^{2n_d}\left(1-\frac{4\hat{T}^2\rho^2\sigma_{Y_i}^2\sigma_{Y_j}^2}{\left(\sigma_{Y_i}^2+\hat{T}^2\sigma_{Y_j}^2\right)^2}\right)^{n_d+\frac{1}{2}}\Gamma\left(n_d\right)}, \tag{3-28}$$

where the correlation coefficient $\rho = \sqrt{\frac{{}_{A}c_{Y_iY_j}^2 + {}_{C}c_{Y_iY_j}^2}{\sigma_{Y_i}^2\sigma_{Y_j}^2}}$.

It is recalled, of course, that the transmissibility is a function of frequency, so the probability density function in Equation (3-28) should be evaluated at every frequency point with the corresponding $\sigma_{Y_i}^2\left(\omega\right)$, $\sigma_{Y_j}^2\left(\omega\right)$ and $\rho\left(\omega\right)$ at that frequency line.

This general result quantifies exactly the uncertainty in transmissibility amplitude estimation for the estimator given in Equation (2-11). Computation of this exact probability density function allows the computation of more accurate order statistics, as necessary, in order to quantify uncertainty from an estimate of transmissibility. This is of particular importance when transmissibility is being used as a feature for system identification or structural health monitoring applications. Although Equation (3-28) nicely characterizes the distribution of transmissibility magnitude estimations calculated from estimator in Equation (2-11), there is a limitation of the estimator itself. According to Equation (3-19), if 1/*SNR* is not ignorable, or not equal on i^{th} and j^{th} channel, the estimations will be biased and degraded, despite of how many averages there are. This makes the statistical model less useful and motives another UQ approach in the next part.

3.2.3. Gaussian Bivariate approach

From Equation (2-13), it is known that the estimators $\hat{T}_{ij} = \hat{G}_{xy_i} \big/ \hat{G}_{xy_j}$ and $\hat{T}_{ij} = \hat{H}_i \big/ \hat{H}_j$ are unbiased if the additive noise is uncorrelated with the measurements. Considering central limit theorem, both numerator and denominator in the two estimators are the results from n_d averages, and therefore the transmissibility magnitude could be approximated as the ratio between two Gaussian random variables.

As secondary consideration, however, note that the former uses the cross power spectral density estimates while the latter uses the FRF estimates. Formulas for normalized error $\varepsilon(\cdot)$ for cross power spectra and transfer function estimates with zero input noise *m*(*t*) are given by [79], where $\gamma_{xy_i}^2$ is the usual coherence function:

$$\varepsilon\left(\left|\hat{G}_{xy_i}\right|\right) \equiv \frac{\sigma\left(\left|\hat{G}_{xy_i}\right|\right)}{\left|G_{xy_i}\right|} = \frac{1}{\sqrt{n_d \gamma_{xy_i}^2}} \quad \text{and} \quad \varepsilon\left(\left|\hat{H}_i\right|\right) \equiv \frac{\sigma\left(\left|\hat{H}_i\right|\right)}{\left|H_i\right|} = \sqrt{\frac{1-\gamma_{xy_i}^2}{2n_d \gamma_{xy_i}^2}}, \tag{3-29}$$

From Equations (3-29), the normalized error for the FRF estimate decreases with both averaging (n_d) and with improved coherence ($\gamma_{xy_i}^2 \rightarrow 1$), while the normalized error for the cross-power spectrum can only improve with averaging, even with perfect coherence. Figure 3-3 compares the normalized error for these two estimators for fixed n_d=100 averages. For this performance reason, the transmissibility estimate, approached by the ratio of Gaussian-like transfer function estimates, is considered "optimal". However, in this section, the non-optimal estimator is selected, for a purpose of uncertainty quantification illustration, since the modeling process in this section is not specific for estimations through FRF or auto-power density.

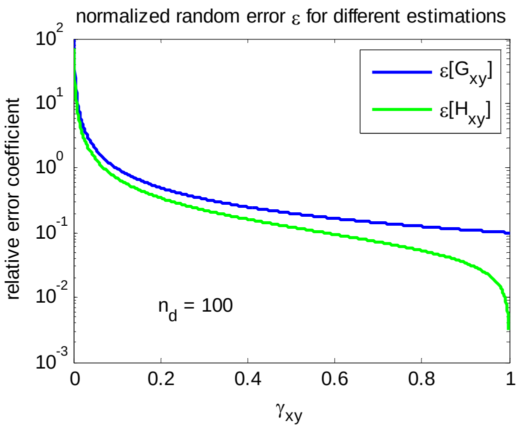

Figure 3-3: comparison of normalized error for a fixed number of averages

Recalling the estimator of transmissibility in Equation (2-9), the magnitude estimation is:

$$\left|\hat{T}_{ij}(\omega)\right| = \frac{\left|\hat{G}_{xv_i}(\omega)\right|}{\left|\hat{G}_{xv_j}(\omega)\right|}, \tag{3-30}$$

in which the cross power spectrum $\left|\hat{G}_{xy}(\omega)\right|$ at any frequency ω has a histogram that is well-described by a gamma distribution, although the actual distribution of this random variable is not accessible, assuming the time series *x*(*n*) and *y*(*n*) are Gaussian, and when the number of averaging is sufficient, the degree of both Gamma distributions will be high enough to make both distributions adequately Gaussian. As a result, the transmissibility magnitude estimation in Equation (3-30) can be modeled as the ratio between two correlated Gaussian random variables with each mean and variance, i.e.,

$$\left|\hat{G}_{xy_{i,j}}(\omega)\right| \sim \mathcal{N}\left(\mu_{C_{i,j}}, \sigma^2_{C_{i,j}}\right), \tag{3-31}$$

in which the subscript $_C$ denotes cross power density and *i* and *j* represent order statistics from each channel. Joint probability density function of two cross power density magnitude estimations $p_{i,j}$ is therefore stated in Equation (3-32):

$$p_{i,j}(g_i, g_j) = \frac{1}{2\pi\sigma_{Ci}\sigma_{Cj}\sqrt{1-\rho^2}} e^{-\frac{1}{2(1-\rho^2)}\left(\frac{(g_i-\mu_{Ci})^2}{\sigma^2_{Ci}} - 2\rho\frac{(g_i-\mu_{Ci})(g_j-\mu_{Cj})}{\sigma_{Ci}\sigma_{Cj}} + \frac{(g_j-\mu_{Cj})^2}{\sigma^2_{Cj}}\right)}, \tag{3-32}$$

where g_i and g_j are the variables of $\left|\hat{G}_{xy_i}\right|$ and $\left|\hat{G}_{xy_j}\right|$ in the sampling domain, and ρ is the correlation between the two random variables. By integrating over the domain of $g_i/g_j \le h$, Fieller gives explicitly the probability density function of Gaussian ratio distribution [95], and rewriting it with above-mentioned parameters, the probability density function of the transmissibility magnitude estimation $\left|\hat{T}\right|$ is expressed with respect to sampling variable h as Equation (3-33) shows:

$$p_{|\hat{T}|}(h) = \frac{\gamma}{\pi\alpha} \cdot e^{-\frac{1}{2(1-\rho^2)}\left(\frac{\mu_{Ci}^2}{\sigma_{Ci}^2} - 2h\frac{\mu_{Ci}\mu_{Cj}}{\sigma_{Ci}\sigma_{Cj}} + \frac{\mu_{Cj}^2}{\sigma_{Cj}^2}\right)} + \frac{\beta}{\sqrt{2\pi}\alpha^{3/2}} \cdot e^{-\frac{\left(\mu_{Ci}-h\mu_{Cj}\right)^2}{2\alpha}} \cdot \mathrm{Erf}\left(\frac{\beta}{\sqrt{2\alpha\gamma}}\right), \tag{3-33}$$

in which $\alpha = \sigma_{Ci}^2 - 2\rho h \sigma_{Ci}\sigma_{Cj} + h^2\sigma_{Cj}^2$, $\beta = \sigma_{Ci}\left(\rho\mu_{Ci}\sigma_{Cj} - \mu_{Cj}\sigma_{Ci}\right) + h\sigma_{Cj}\left(\rho\mu_{Cj}\sigma_{Ci} - \mu_{Ci}\sigma_{Cj}\right)$, $\gamma = \sqrt{1-\rho^2}\sigma_{Ci}\sigma_{Cj}$, $\rho = \frac{\mathrm{cov}\left(g_i, g_j\right)}{\sigma_{Ci}\sigma_{Cj}}$, and $\mathrm{Erf}\left(\cdot\right)$ is error function.

Similarly, considering the magnitude H1 estimation of FRF in Equation (3-34):

$$\left|\hat{H}\left(\omega\right)\right| = \frac{\left|\hat{G}_{xy}\left(\omega\right)\right|}{\left|\hat{G}_{xx}\left(\omega\right)\right|}, \tag{3-34}$$

the auto-power density on denominator is proved to be Chi-square distributed in 3.2.2, which is a special case of Gamma distribution, therefore, with sufficient averages, the Gaussian bivariate approach can be also applied onto statistical modeling of FRF magnitude estimations. Denote parameters of Gaussian $\left|\hat{G}_{xx}\left(\omega\right)\right|$ in Equation (3-35):

$$\left|\hat{G}_{xx}\left(\omega\right)\right| \sim \mathcal{N}\left(\mu_A, \sigma_A^2\right), \tag{3-35}$$

where subscript $_A$ represents auto-power spectrum. Following the same derivation, it will come up to Equation (3-36), which is the PDF of H1 estimation of FRF magnitude:

$$p_{|\hat{H}_{i,j}|}(h) = \frac{\gamma}{\pi\alpha} \cdot e^{-\frac{1}{2(1-\rho^2)}\left(\frac{\mu_A^2}{\sigma_A^2} - 2h\frac{\mu_A\mu_{C_{i,j}}}{\sigma_A\sigma_{C_{i,j}}} + \frac{\mu_{C_{i,j}}^2}{\sigma_{C_{i,j}}^2}\right)} + \frac{\beta}{\sqrt{2\pi}\alpha^{3/2}} \cdot e^{-\frac{\left(h\mu_A-\mu_{C_{i,j}}\right)^2}{2\alpha}} \cdot \mathrm{Erf}\left(\frac{\beta}{\sqrt{2\alpha\gamma}}\right), \tag{3-36}$$

in which the notations follow the same convention but different coefficients:

$\alpha = h^2\sigma_A^2 - 2\rho h\sigma_A\sigma_{C_{i,j}} + \sigma_{C_{i,j}}^2$, $\beta = h\sigma_A\left(\rho\mu_A\sigma_{C_{i,j}} - \mu_{C_{i,j}}\sigma_A\right) + \sigma_{C_{i,j}}\left(\rho\mu_{C_{i,j}}\sigma_A - \mu_A\sigma_{C_{i,j}}\right)$,

$\gamma = \sqrt{1-\rho^2}\sigma_A\sigma_{C_{i,j}}$, and $\rho = \dfrac{\mathrm{cov}\left(g_A, g_{C_{i,j}}\right)}{\sigma_A\sigma_{C_{i,j}}}$.

The H2 estimator of FRF magnitude will have the same form of PDF with only the parameters different from H1 estimator, and will not be explicitly presented in this section.

3.3. Phase uncertainty

For complex transfer functions, the phase estimation, at arbitrary frequency ω, is related with its real and imaginary part via four-quadrant arctangent function ($\mathrm{atan}\,2(\cdot)$), and phase estimation of transmissibility is mathematically shown in Equation (3-37):

$$\measuredangle\hat{T}(\omega) = \arg\left(\hat{T}(\omega)\right) = \mathrm{atan}\,2(\hat{T}_I(\omega), \hat{T}_R(\omega)), \tag{3-37}$$

and real and imaginary parts $T_R = \Re[T]$ and $T_I = \Im(T)$. For the same purpose as modeling magnitude estimations, the estimations of real and imaginary parts at frequency ω, $\hat{T}_R(\omega)$ and $\hat{T}_I(\omega)$, can be regarded as two Gaussian distributed random variables, i.e.,

$$\begin{aligned} \hat{T}_R &\sim \mathcal{N}\left(\mu_{T_R}, \sigma_T^2\right) \\ \hat{T}_I &\sim \mathcal{N}\left(\mu_{T_I}, \sigma_T^2\right) \end{aligned}. \tag{3-38}$$

In Equation (3-38), the real and imaginary parts have the same variance, because both parts are originally from the same Gaussian time series, and the Fourier Transform does not discriminate the variance of each part. Moreover, because the real and imaginary parts are always orthogonal, the correlation between these two variables is zero. Therefore, the uncertainty of phase estimation may be modeled starting from the joint probability density function of uncorrelated Gaussian bivariates:

$$p_{\hat{T}_R,\hat{T}_I}(h_R,h_I)=\frac{1}{2\pi\sigma_T^2}e^{-\frac{1}{2}\left(\frac{\left(h_R-\mu_{T_R}\right)^2+\left(h_I-\mu_{T_I}\right)^2}{\sigma_T^2}\right)}. \tag{3-39}$$

In order to quantify the uncertainty of random variable defined in Equation (3-37), variable θ is introduced, which is variable of the PDF in the phase sampling domain, and define a transform $\mathbf{\Psi}:\langle h_R,h_I\rangle\rightarrow\langle h_R,\theta\rangle$ to relate the real and imaginary samples in Equation (3-39):

$$\begin{cases} h_R=h_R \\ \theta=\operatorname{atan}2\left(h_I,h_R\right) \end{cases}, \tag{3-40}$$

so the inverse transform $\mathbf{\Psi}^{-1}:\langle h_R,\theta\rangle\rightarrow\langle h_R,h_I\rangle$ will be:

$$\begin{cases} h_R=h_R \\ h_I=\tan\left(\theta\right)h_R \end{cases}. \tag{3-41}$$

Thus, the joint probability density function p_Θ of the transformed variables is given by Equation (3-42):

$$p_\Theta(h_R,\theta)=\left|\mathbf{J}\right|\cdot p_{\hat{T}_R,\hat{T}_I}(h_R,h_I)=\left|\mathbf{J}\right|\cdot p_{\hat{T}_R,\hat{T}_I}(\mathbf{\Psi}^{-1}\left(h_R,\theta\right)), \tag{3-42}$$

where $\mathbf{J} = \left| \frac{\partial\left(h_R, h_I\right)}{\partial\left(h_R, \theta\right)} \right| = h_R \sec^2\left(\theta\right)$ is the Jacobian determinant and $p_{\hat{T}_R,\hat{T}_I}(\cdot,\cdot)$ is the joint PDF in Equation (3-39).

Once the joint PDF in Equation (3-42) is obtained, the marginal distribution may be calculated by integrating Equation (3-42) over the entire h_R domain so that the PDF of phase estimation is achieved. Because the inverse transform defined in Equation (3-41) loses the four-quadrant information which originally existed in the forward transform in Equation (3-40), the marginal integration must be calculated for the right and left half-planes separately:

$$\begin{aligned} p_{\measuredangle\hat{T},I\&IV}(\theta) &= \int_0^{+\infty} p_\Theta(h_R,\theta)dh_R = \int_0^{+\infty} h_R \sec^2\left(\theta\right)\cdot p_{\hat{T}_R,\hat{T}_I}(h_R,\tan\left(\theta\right)h_R)dh_R \\ p_{\measuredangle\hat{T},II\&III}(\theta) &= \int_{-\infty}^{0} p_\Theta(h_R,\theta)dh_R = \int_{-\infty}^{0} -h_R \sec^2\left(\theta\right)\cdot p_{\hat{T}_R,\hat{T}_I}(h_R,\tan\left(\theta\right)h_R)dh_R \end{aligned}, \tag{3-43}$$

and this means the distribution of phase estimation is described in a piecewise function. However, the final closed-form solution after substituting Equation (3-39) into Equation (3-43) simplifies to a unified equation:

$$p_{\measuredangle\hat{T}}(\theta) = \frac{e^{-\frac{\mu_{T_R}^2+\mu_{T_I}^2}{2\sigma_T^2}}}{2\pi} + \frac{\eta\cdot e^{-\frac{\left(\mu_{T_R}\sin(\theta)-\mu_{T_I}\cos(\theta)\right)^2}{2\sigma_T^2}}}{2\sqrt{2\pi}\sigma_T}\left(1+\mathrm{Erf}\left(\frac{\eta}{\sqrt{2}\sigma_T}\right)\right), \tag{3-44}$$

where $\eta = \mu_{T_R}\cos\left(\theta\right) + \mu_{T_I}\sin\left(\theta\right)$, and $\mathrm{Erf}\left(\cdot\right)$ is the error function. This PDF quantifies the uncertainty of phase estimation and is supposed to be evaluated within any 2π period, independent of the absolute phase reference point.

In fact, Equation (3-44) characterizes not only the phase estimation distribution of transmissibility, but any phase estimation of complex Gaussian variables. In the context of transfer function, we can also quantify FRF phase uncertainty by slightly modifying this equation. Assuming the Gaussian bivariate parameters are shown in Equation (3-45):

$$\begin{aligned} \hat{H}_R &\sim \mathcal{N}\left(\mu_{H_R}, \sigma_H^2\right) \\ \hat{H}_I &\sim \mathcal{N}\left(\mu_{H_I}, \sigma_H^2\right) \end{aligned}, \tag{3-45}$$

the final form of FRF phase estimation's PDF is:

$$p_{\measuredangle \hat{H}}(\theta) = \frac{e^{-\frac{\mu_{H_R}^2 + \mu_{H_I}^2}{2\sigma_H^2}}}{2\pi} + \frac{\eta \cdot e^{-\frac{\left(\mu_{H_R}\sin(\theta) - \mu_{H_I}\cos(\theta)\right)^2}{2\sigma_H^2}}}{2\sqrt{2\pi}\sigma_H}\left(1 + \mathrm{Erf}\left(\frac{\eta}{\sqrt{2}\sigma_H}\right)\right), \tag{3-46}$$

in which $\eta = \mu_{H_R}\cos\left(\theta\right) + \mu_{H_I}\sin\left(\theta\right)$.

This chapter, in part, has been published in *Proc. SPIE 7650*, Zhu Mao and Michael Todd, 2010. The title of this paper is “A structural transmissibility measurements-based approach for system damage detection”. The dissertation author was the primary investigator and author of this paper. A portion of this chapter has been published in *Mechanical Systems and Signal Processing*, Zhu Mao and Michael Todd, 2012. The title of this paper is “A model for quantifying uncertainty in the estimation of noise-contaminated measurements of transmissibility”. The dissertation author was the primary investigator and author of this paper. A portion of this chapter has been submitted to *Mechanical Systems and Signal Processing*, by Zhu Mao and Michael Todd. The title of this paper is “Statistical modeling of frequency response function estimation for uncertainty quantification”. The dissertation author was the primary investigator and author of this paper.

4. Statistical Model Validation

In Chapter 3, the uncertainty of transfer function estimations, both magnitude and phase, has been quantified through different models, where these models assumed an underlying stationary Gaussian process/noise assumption. The equations derived are specific for certain estimators, but the modeling approach is generic for the UQ of other estimators, with similar derivation. In this chapter, some of the representative estimators will be used as examples to estimate transmissibility/FRF and quantify uncertainty and demonstrate the validation process.

Besides the cubical FE model introduced in Chapter 2, several test structures are adopted to validate these proposed statistical models, providing simulated data with "ideal" testing and real lab measurements, respectively. For the test structure providing simulation data, structural output responses can be calculated analytically from modal superposition; and the input excitation can be ideally Gaussian and white without any coupling effect from shaker or structure. Simulation data are contaminated with white noise to validate UQ models under more conditions. For a real structure, the same validation process is applied onto a lab-scale clamped plate; the actual data will contain both internal and external uncertainties, where further contamination is also added to the lab measurements with extraneous artificial noise, so as to validate the statistical models via a more stringent test.

4.1. FE satellite model

Gaussian white noise is applied onto the aforementioned surrogate PnPSat model in ABAQUS (section 2.1), to validate the transmissibility statistical quantification model established in 3.2.1 via linear perturbation. Standard deviation is used as bounds of uncertainty, and the FE model is run n_t=128 times for a Monte-Carlo test. With certain pre-set “number of σ”, i.e. significance, outliers at each frequency point are counted and percentage over the entire n_t realizations is compared to Bendat and Piersol's classical model presented in [79-81].

In Figure 4-1, an example of outlier percentage is plotted, which is the amount of transmissibility estimations beyond 1σ error bounds, at every frequency point, divided by the total number of tests n_t, and the green line represents the average over entire frequency range, compared with the red line, which is the 1-σ Gaussian threshold (around 32%.) The upper plot in Figure 4-1 is obtained from Bendat's model with noise on i^{th} channel (input side of Figure 3-2) ignored, and the lower plot is the result calculated from our model derived in 3.2.1.

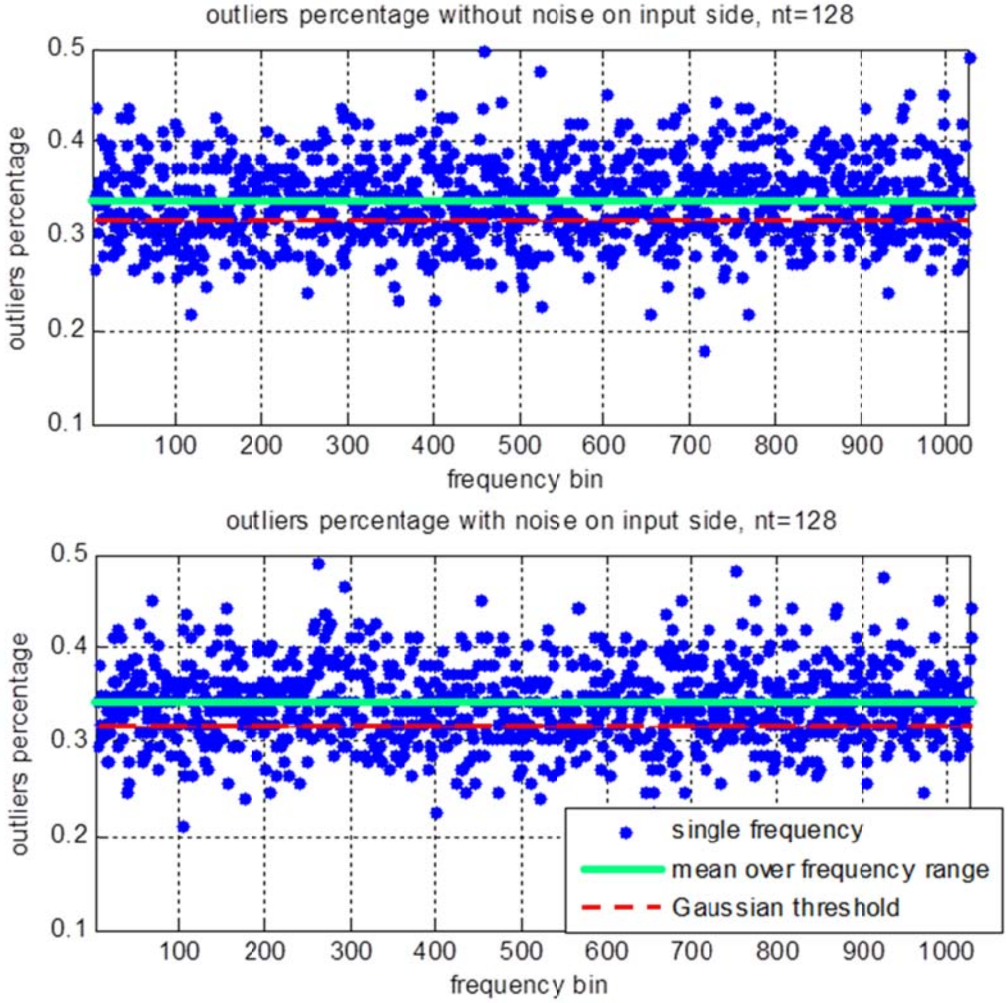

Figure 4-1: outliers counting in error bounds test

Figure 4-1 illustrates that, considering noise on both input and output side of the signal flow in Figure 3-2, performance of the derived model is as good as Bendat's classical one. Both models have an overall outlier percentage slightly bigger than Gaussian 1-σ level, because the real distribution of transmissibility is not normal and it is inappropriate to anticipate equal significance levels with arbitrary cutoff threshold.

A more detailed list, with outlier percentages from different noise levels and variation intervals, is included in Table 4-1. From this table, there is a consistency over various noise levels, and an acceptable agreement with the theoretical Gaussian probabilities. For a comparison purpose, outlier percentages calculated from classical model with input noise ignored are also listed in the table.

Because running FE models are expensive and time consuming, the results in Table 4-1 are from data sets sufficient for only n_d=16 times of averages and n_t=128 total Monte-Carlo realizations. Results are good enough to show a consistency and validation.

Table 4-1: percentage of outliers with perturbation uncertainty bounds

Noise to Signal Ratio		**1σ (68%)**		**2σ (95%)**		**3σ (99%)**	
Input	**Output**	**w/ noise**	**w/o noise**	**w/ noise**	**w/o noise**	**w/ noise**	**w/o noise**
0.200	0.190	33.9	33.7	6.35	6.24	0.879	0.865
0.100	0.095	34.1	34.1	6.54	6.23	0.811	0.796
0.059	0.057	34.3	34.2	6.35	6.25	0.732	0.739
0.020	0.019	34.1	34.2	6.32	6.26	0.765	0.743
0.0050	0.0047	34.0	33.9	6.39	6.28	0.704	0.721
The number of averages is n_d=16 in power spectrum calculation.							

4.2. Beam simulation

Instead of generating input and output data through sophisticated FE model, this section, statistical quantification models derived in Equations (3-20, 28, 33, 36, 44 and 46) are validated. Taking advantage of the availability of analytical FRF/transmissibility, structural responses are much more easily accessible, therefore big amount of Monte-Carlo realizations will be practical and more number of averages can make the Gaussian assumption better satisfied.

4.2.1 Model description and transfer functions

A beam test structure with proportional damping is considered as the test structure for generating frequency response function and transmissibility from which surrogate "experimental" data will be obtained in order to test the model derived in the previous chapter. The structure is excited with Gaussian white noise, and the vertical acceleration responses at two arbitrary positions are considered as measured outputs. According to knowledge of dynamics, the frequency response function between input and output at any location can be approximated analytically by the superposition of first N mode shapes, as shown in Equation (4-1), where Ψ_{pk} and Ψ_{jk} are the k^{th} mode shape functions at input and output coordinates p and j, and Ω_k and ζ_k are the natural frequency and damping ratio for k^{th} mode, respectively:

$$H_j(\omega)_{\text{(accelerance)}} = \frac{V_j}{X} = \sum_{k=1}^{N} \frac{\Psi_{jk}\Psi_{pk}\omega^2}{\Omega_k^2 - \omega^2 + 2\mathbf{i}\zeta_k\Omega_k\omega} e^{\mathbf{i}(\theta_k - \pi)}, \tag{4-1}$$

where $k = 1,2,3...n$ and $\tan\theta_k = \frac{2\zeta_k\Omega_k\omega}{\omega^2 - \Omega_k^2}$.

As a benchmark for the statistical model, Equation (4-2) shows the analytically-calculated transmissibility as the ratio between the two FRFs:

$$T_{ij}(\omega) = \frac{V_i/X}{V_j/X} = \frac{\sum_{k=1}^{N} \frac{\Psi_{ik}\Psi_{pk}}{\Omega_k^2 - \omega^2 + 2\mathbf{i}\zeta_k\Omega_k\omega} e^{\mathbf{i}(\theta_k - \pi)}}{\sum_{k=1}^{N} \frac{\Psi_{jk}\Psi_{pk}}{\Omega_k^2 - \omega^2 + 2\mathbf{i}\zeta_k\Omega_k\omega} e^{\mathbf{i}(\theta_k - \pi)}}, \tag{4-2}$$

Figure 4-2 shows the setup of beam structure designed with a standard W40 I-shape cross-section, 12-meter length span, and 3% proportional damping. The input and two output positions are arbitrarily picked at 15%, 30% and 70% of the entire beam length respectively.

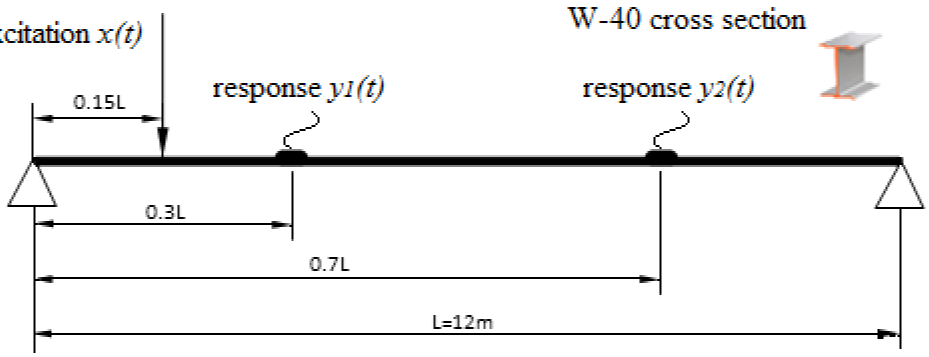

Figure 4-2: simply-supported beam with excitation and measurements positions for model validation

After calculating the analytical FRFs and transmissibility via Equation (4-1) and (4-2), these transfer functions are plotted in logarithm scale in Figure 4-3, with first five modes taken into account.

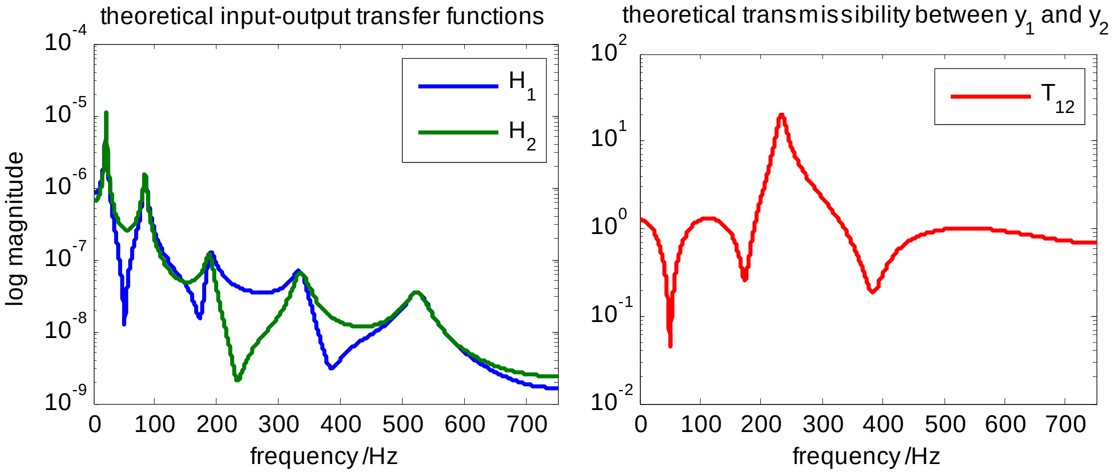

Figure 4-3: theoretical FRFs and transmissibility for the simple beam structure

4.2.2 Validation for transmissibility

Estimation of transmissibility is achieved from estimator defined in Equation (2-11), which supplies only magnitude estimation. In the meantime, auto-power density is also verified to be Chi-square distributed in this part. For case 1, no extraneous noise will be included, i.e. pure responses calculated from modal superposition and *NSR*=0. For case 2, different levels of contamination are considered to simulate a stricter test situation.

Case 1: No extraneous noise

The first case assumes no extraneous noise on any channel such that the explicit noise terms in the estimators are ignored, and only internal estimation uncertainty is considered. In other words, the test "measures" v_1 and v_2 from the two locations in Figure 4-2.

In Figure 4-4, a sample of auto-power spectrum estimations $\hat{G}_{vv}$ from noise-free responses v_1 and v_2 is plotted, with the 90% confidence bounds from Equation (3-20) shown in dashed lines, and the expectation value calculated from the proposed PDF. Similarly, an arbitrary sample of transmissibility estimation from one test is shown in Figure 4-5, with uncertainty bounds calculated from Equation (3-28). The two figures show how the estimation of power density and transmissibility from single test falling in between the upper and lower boundaries.

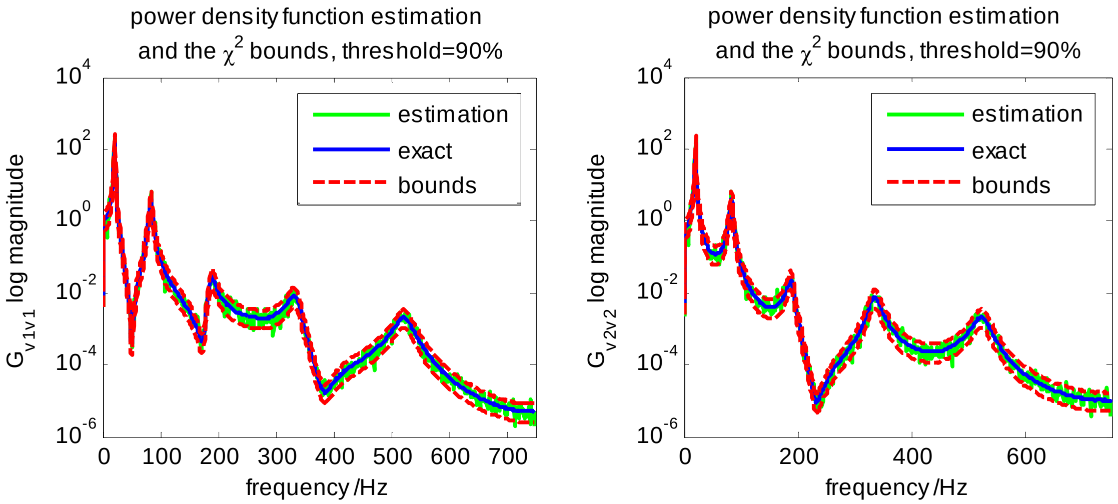

(a) G_{v1v1} estimation and uncertainty bounds (b) G_{v2v2} estimation and uncertainty bounds

Figure 4-4: auto-power spectrum estimations at the two response locations respectively, and 90% confidence bounds under noise free condition

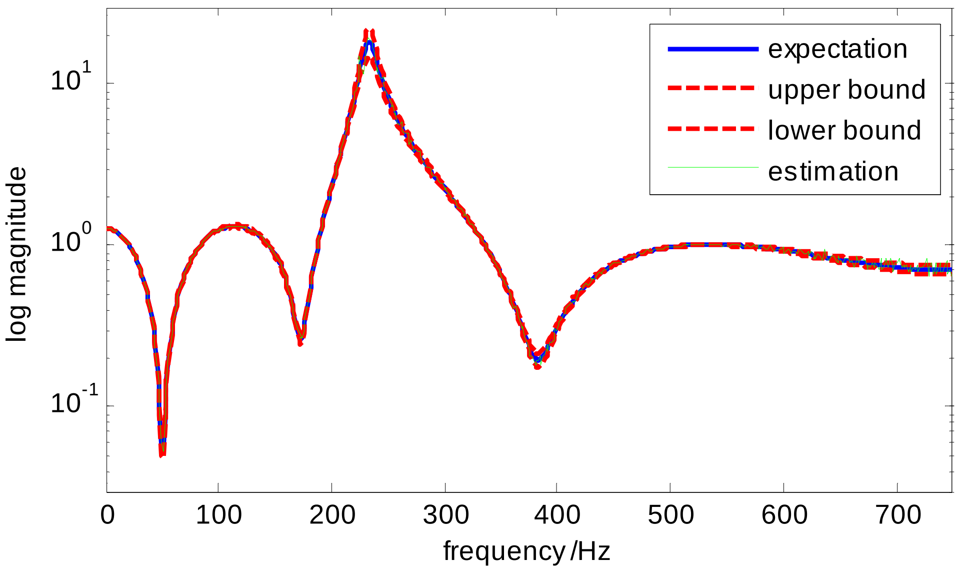

Figure 4-5: transmissibility estimation and 90% confidence bounds, noise free case

Qualitatively, the analytically-predicted confidence lines appear to appropriately bind the estimation, but a quantitative verification is performed via outlier detection and Monte-Carlo analysis. As such, the same calculation of estimations is repeated for a large number of tests (n_t=512times), so that at each frequency point, there are 512 estimates, and from these independent events, the probability of the estimations outlying the confidence boundaries may be compared with the pre-set threshold associated to the boundaries. The outlier percentage for all three different estimations at each frequency point, which is the number of outliers divided by the total number of tests in Monte-Carlo simulation, are plotted in Figure 4-6, together with a benchmark line on the pre-set level of 10%. There is excellent consistency between the observed outlier percentage and the pre-established thresholds computed analytically from the probability density function Equation (3-20) and (3-28).

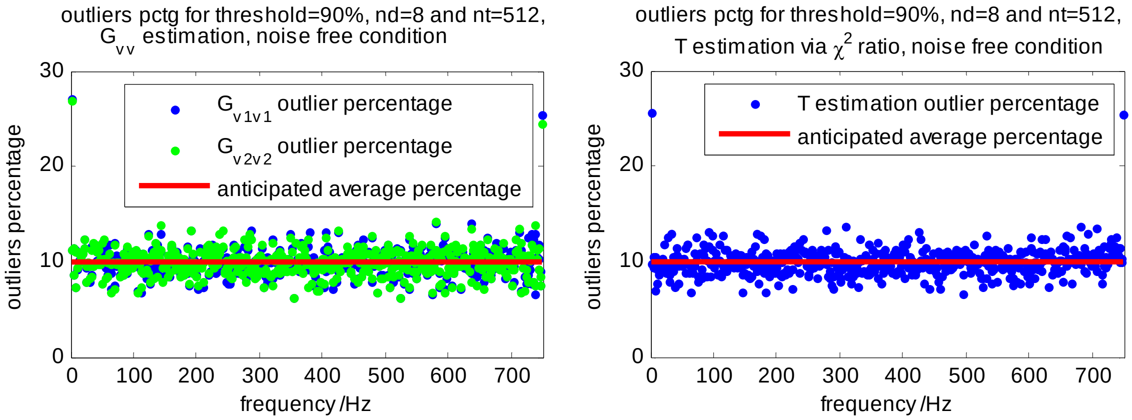

(a) outlier percentage of auto-power density estimation, with 90% threshold

(b) outlier percentage of transmissibility estimation, with 90% threshold

Figure 4-6: Outlier percentage of estimations at every frequency point

Further validation may be given by examining the Monte-Carlo simulation histograms at each frequency line and comparing to the theoretical distributions (for the output auto-spectra in Equation (3-20) and the transmissibility in Equation (3-28)). At one representative frequency line, Figure 4-7 illustrates the agreement between the actual histogram from the Monte-Carlo test and the predicted distribution curve (red curve), with predicted 5% and 1-5% boundaries (green dots) and the expectation (green line). The histogram is extremely well-predicted by the model, including the tails, suggesting that well-quantified uncertainty in the test estimates are possible at even high-order statistical moments, if desirable.

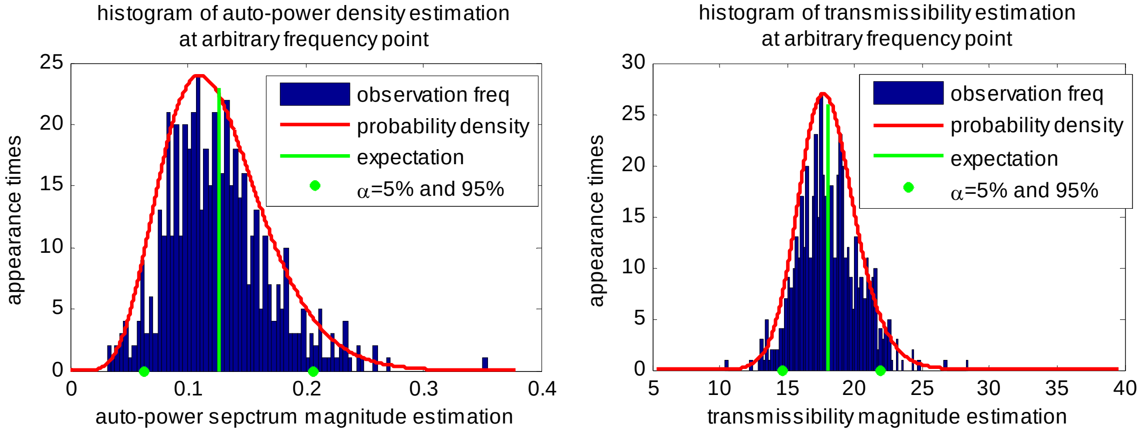

Figure 4-7: histogram of auto-power density and transmissibility estimations with modeled distribution

Case 2: Noise-contaminated output measurements

The previous analysis considered only uncertainties from the estimation process, and this subsection will consider the additional influence of external noise contamination. Due to the inherent performance of any given channel, the output may be dominated by noise in some frequency regions where the local $SNR(\omega)$ is sufficiently low. Under this circumstance, the estimation itself of the transmissibility will lose its accuracy at those frequency lines, specifically for this given estimator, because the auto-power density cannot be eliminated by averaging. In order to show the local dominance, the output measurements are contaminated with Gaussian white noise, but the uncertainty model does not require whiteness. In this subsection, two groups of results will be presented in Figure 4-8 and 4-9, with average 1% and 10% noise-to-signal levels, i.e. global SNR is 20 and 10 dB respectively. All other parameters remain the same as the external noise-free condition in last case.

From Figures 4-8 and 4-9, the statistical model continues to accurately predict the actual pre-set confidence of 90% (as verified by Monte-Carlo outlier count), although, as mentioned, the auto-spectra and transmissibility disappear in the background noise floor at frequency lines with sufficiently low *SNR*.

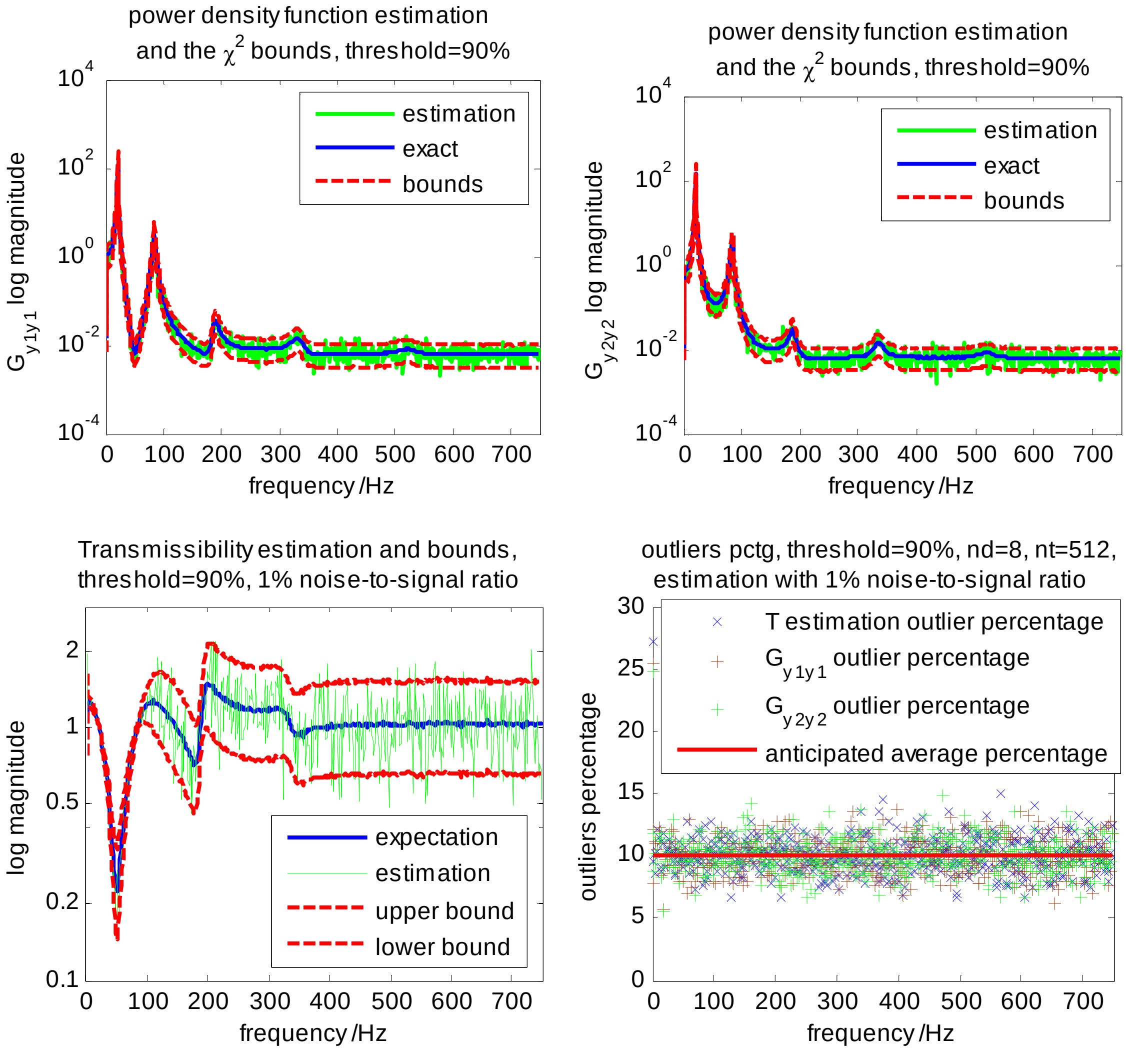

Figure 4-8: Estimations and uncertainty bounds with 90% confidence, and outlier percentages, *SNR*=20dB

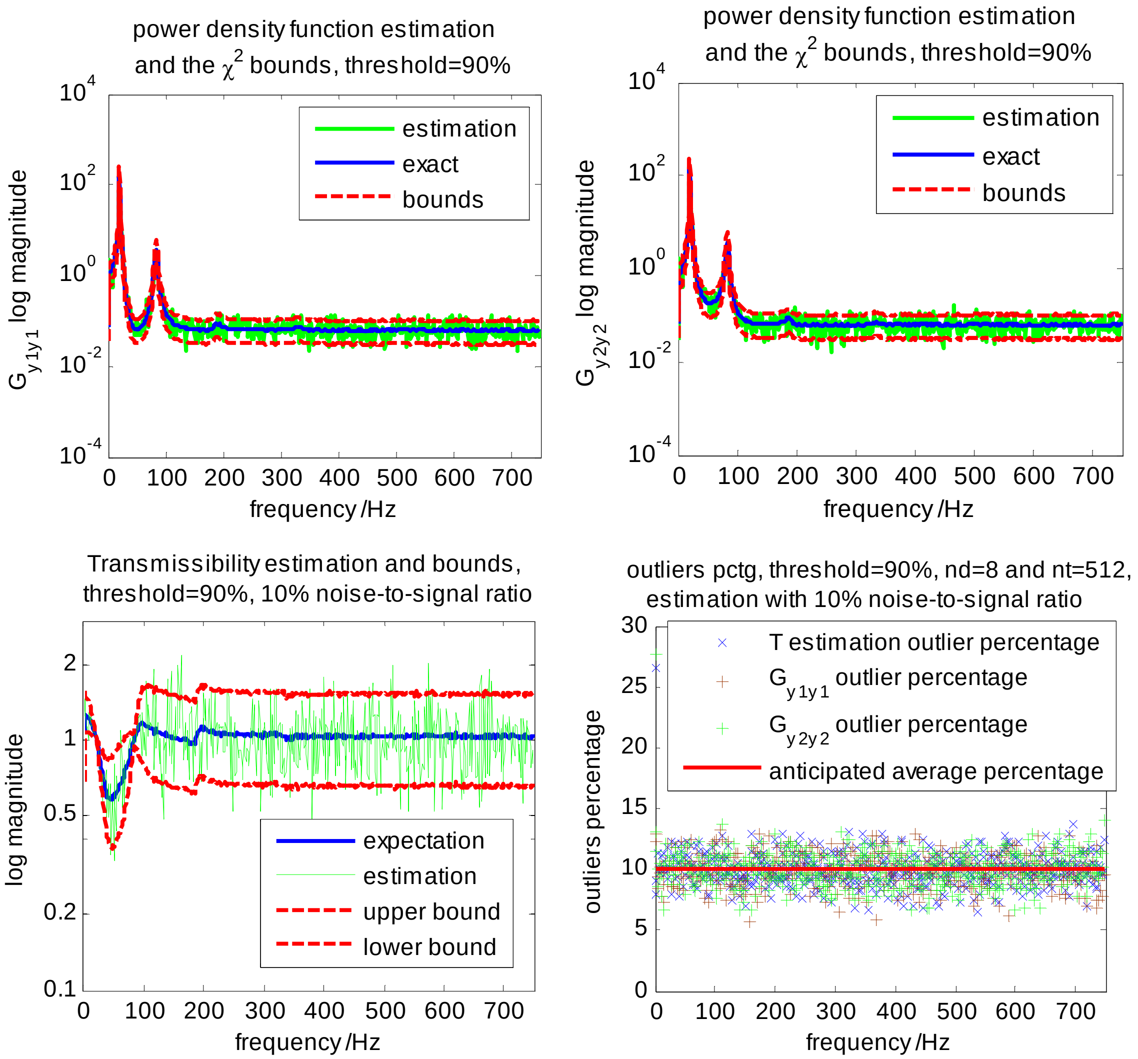

Figure 4-9: Estimations and uncertainty bounds with 90% confidence, and outlier percentages, *SNR*=10dB

4.2.3. Statistical model validation for transmissibility with other thresholds

In the previous subsections, the statistical models of both auto-power density function and transmissibility estimations were validated at each frequency line with a 90% threshold, at two different signal-to-noise levels, where a Monte-Carlo outlier percentage was used as the validation criterion. For a more comprehensive validation, the outlier percentage of the estimations was evaluated for multiple confidence thresholds. For brevity, the outlier percentages at every frequency line will not be presented, but rather the histogram of observed average percentage over the entire frequency domain (up to about 750 Hz) with four pre-set thresholds, which are 99%, 95%, 90%, and 75%, is shown in Figure 4-10.

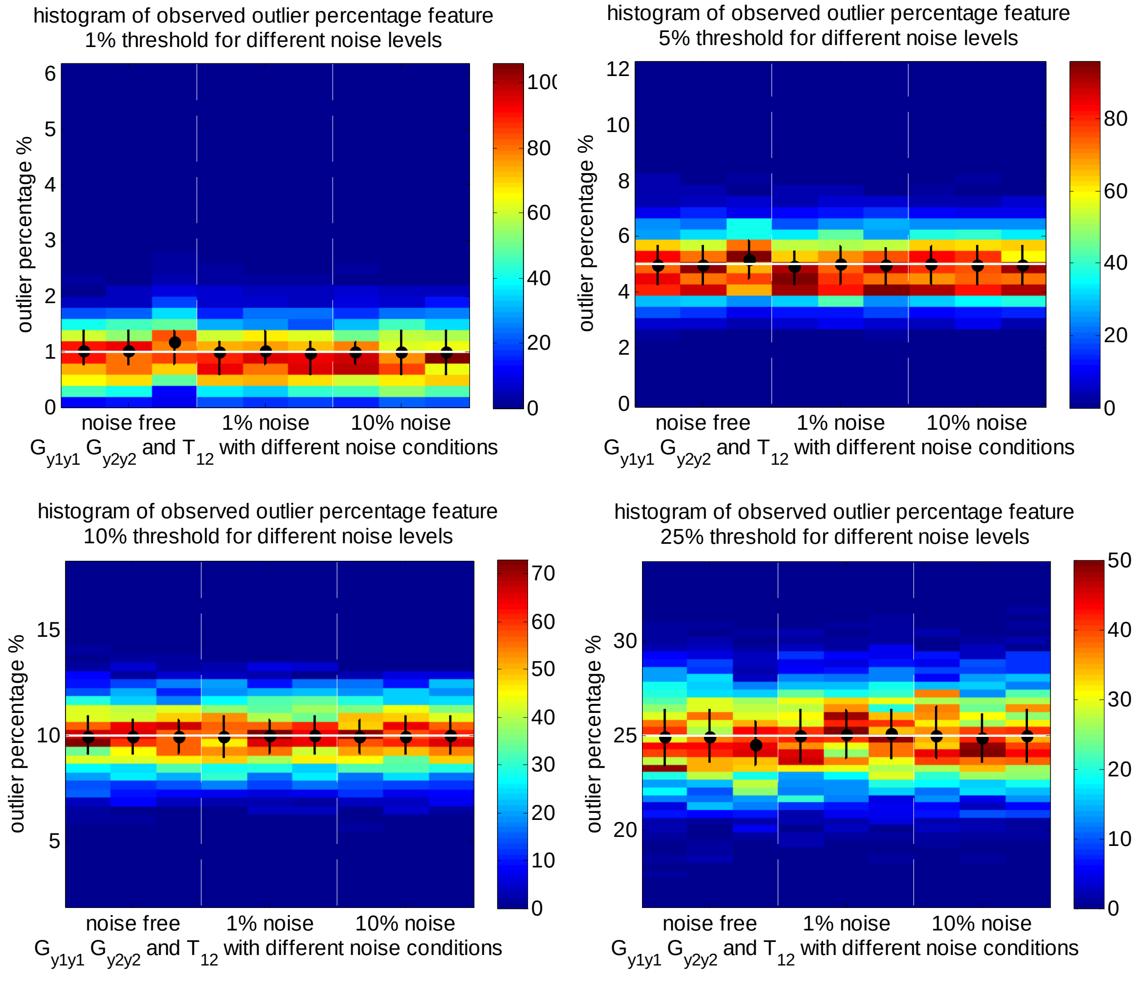

Figure 4-10: histogram and quartiles of averaged outlier percentages for three noise levels and four different thresholds

Figure 4-10 illustrates the histogram of observed average outlier percentage in Monte-Carlo simulation, where the color-scale index counts the number of appearances of outlier percentages indicated at intervals along the vertical axis. Each subplot represents a case with a different pre-set threshold, from which the uncertainty bounds of the estimations are given. In each subplot, there are three groups of histograms representing three noise levels, and in each group there are three columns of data representing the results from $G_{y_1 y_1}$, $G_{y_2 y_2}$ and T_{12} from left to right. The horizontal lines are the anticipated percentages for each picked threshold, while the black dots are the mean values of all the observation, with corresponding quartiles showing in vertical bars which indicate half of the observed average outlier percentages fall inside the delimited areas. Excellent agreement is concluded from Figure 4-10 when high numbers of appearances (determined by the dark red colors) are coincident with the black dots and secondarily with the interquartile ranges. It appears from the figure that the distribution of auto-power spectra and transmissibility estimations given by the statistical model are accurate for all multiple levels of confidence and external noise levels.

4.2.4. Validation for FRF magnitude and phase

In this part, FRF between y_1 in Figure 4-2 and excitation x is estimated via H1 estimator in Equation (2-8). Figure 4-11 shows the magnitude and phase of the FRF for the two different contamination conditions, and also the 90% of confidence interval obtained from the proposed PDF models in Equation (3-36) and (3-46). For the external noise-free condition, uncertainties in both magnitude and phase are very small; a zoomed-in plot is overlaid to show how estimations are bounded. When the simulated output is contaminated by noise at 1% noise-to-signal level in Figure 4-11(b) and (d), the estimations degrade, as expected, and correspondingly, the confidence interval becomes wider.

Instead of visualizing only the 90% confidence interval along all frequencies, Figure 4-12 shows the histogram and modeled distribution for the same four cases, at an arbitrarily picked frequency line, (around 584 Hz.) Quantiles of 5% and 95%, regarding a 90% of confidence interval, are marked with stars. The same conclusion, that noise broadens the distribution of both magnitude and phase estimations, is made.

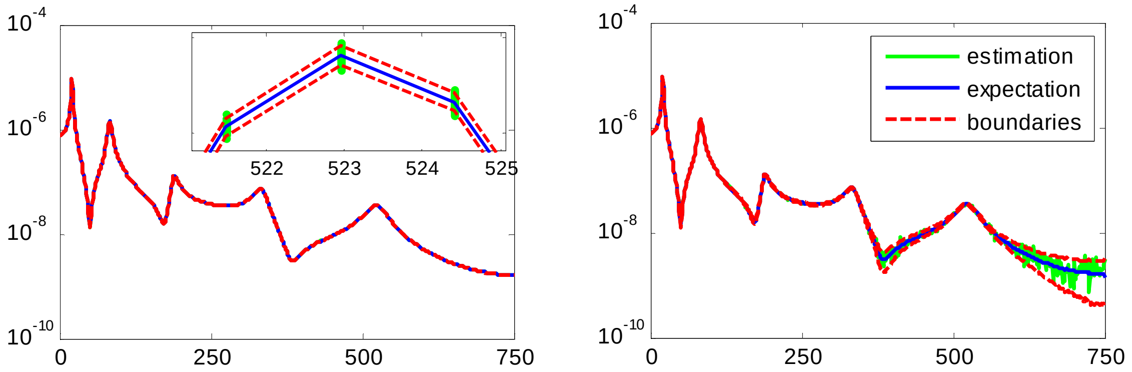

(a) magnitude estimation, noise free (b) magnitude estimation, noise contaminated

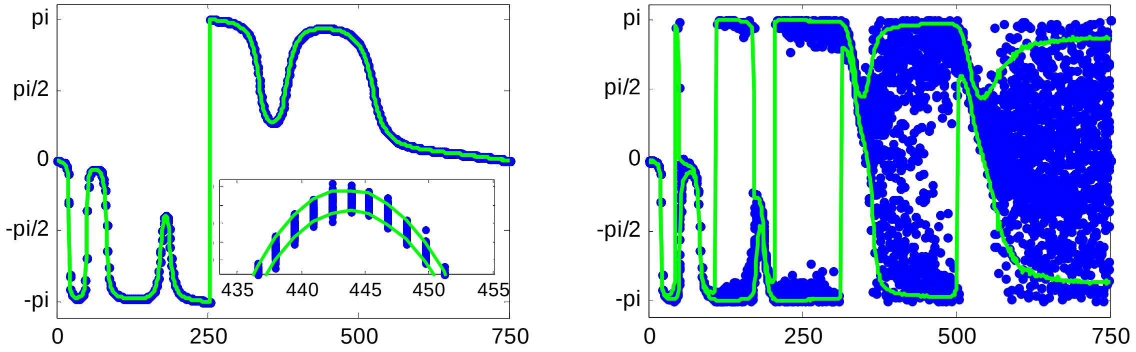

(c) phase estimation, noise free (d) phase estimation, noise contaminated

Figure 4-11: FRF estimations of beam structure with 90% of confidence interval

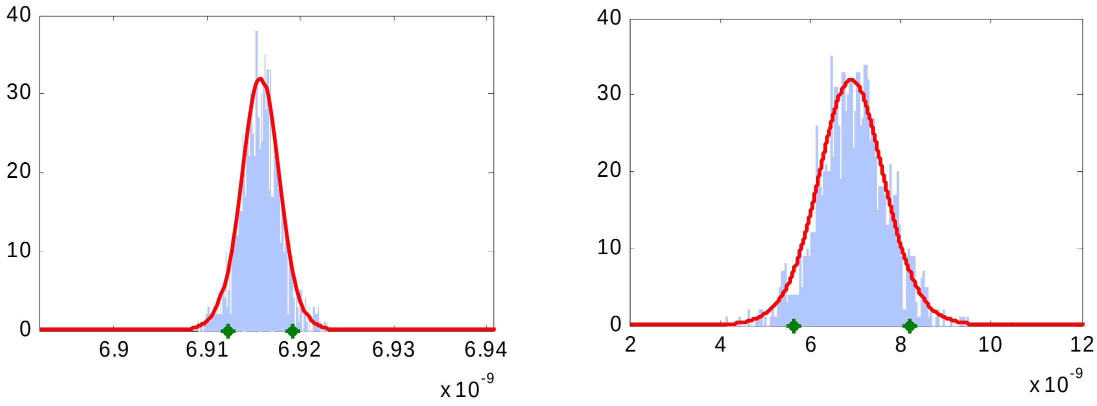

(a) magnitude estimation, noise free (b) magnitude estimation, noise contaminated

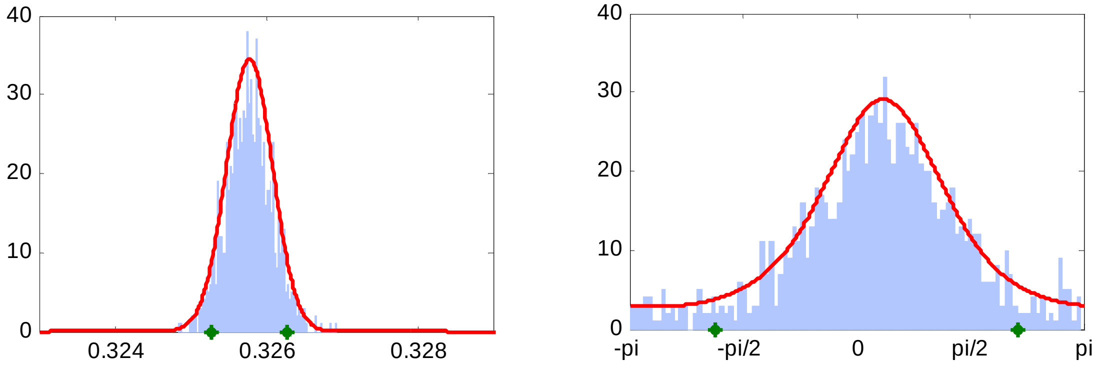

(c) phase estimation, noise free (d) phase estimation, noise contaminated

Figure 4-12: histogram of beam structure estimations at single frequency line with characterized distribution and 90% quantiles

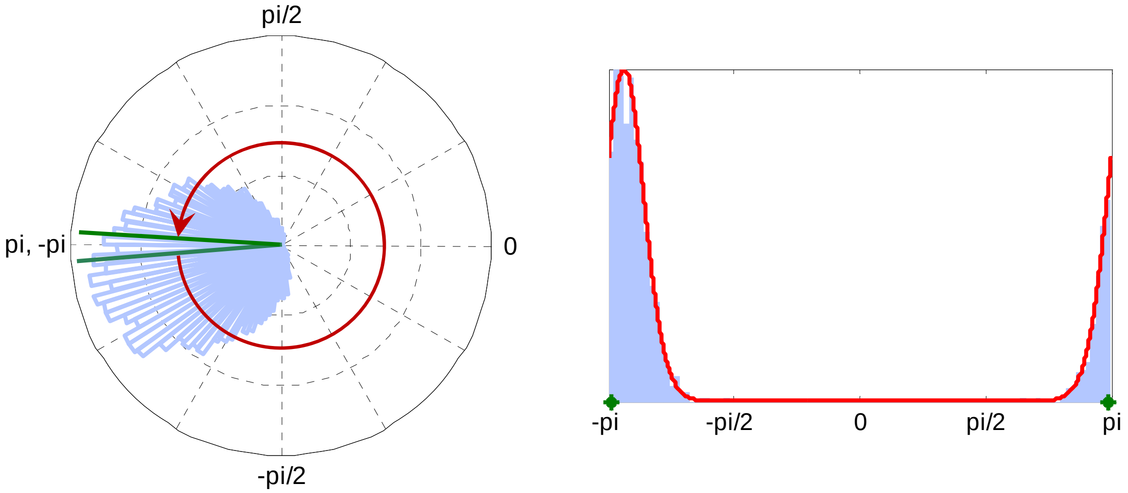

(a) polar histogram of phase estimation (b) linear histogram of phase estimation

Figure 4-13: histograms of beam structure phase estimations

As phase angles with any number of 2π multiples are identical, we use wrapped phase for simplified visualization of the phase estimation and the corresponding confidence intervals, so that all estimations can be compared within a single 2π region. Moreover, this 2π region is usually defined from –π to π, although [0, 2π) and other conventions are also used in different contexts. And for the cluster of phase estimations shown in Figure 4-13(a), we used [–π, π) as the evaluation field, and as a result, the whole distribution will be separated into two parts near far left and right side on the linear histogram shown in Figure 4-13(b), so that the quantiles with 90% of confidence embrace almost the entire 2π region. Again, in real implementation, this can be easily transformed into single-peak distribution by changing the 2π evaluation field, without affecting the statistics.

Figure 4-11 and 4-12 illustrate how the boundaries quantify the uncertainty of estimations qualitatively, but a more thorough validation is implemented by running a Monte-Carlo test and calculating the outlier percentage at each frequency line. By comparing the outlier percentage with the complement of pre-set confidence threshold, the statistical model would be validated in a more quantitative way. Multiple confidence thresholds are pre-set to be 99%, 95%, 90% and 75%, and the outlier percentages over the entire frequency domain (0~750 Hz) for magnitude and phase estimations (both noise contamination conditions) are plotted from Figure 4-14 to 4-17.

In Figure 4-14 to 4-17, outlier percentage observations are plotted in cross marker and the complements of confidence threshold ($1-\alpha$ value) are plotted as a horizontal line for reference. All four groups of results are very consistent with the anticipated lines, and stable across the frequency domain. For this beam model simulation test, all uncontaminated data are truly noise-free, which means operational and environmental uncertainties are non-existent, i.e., uncertainty is from the random input and the estimation algorithm itself. There are some frequency regions in Figure 4-16, especially near 250 Hz, where the consistency is not as good as other regions, because of the imperfect Gaussian propagation from input to real and imaginary part of frequency response function. Once the data are contaminated with noise, more normality comes directly into FRF estimations, as a result the models works better, as what we can see from Figure 4-15 and 4-17.

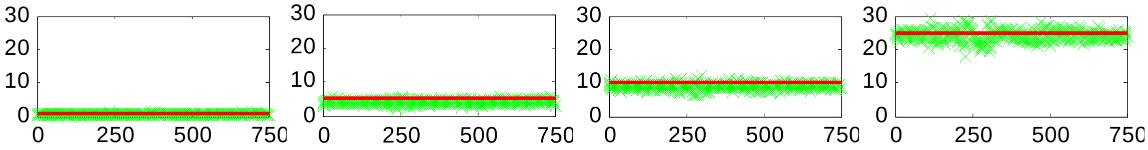

Figure 4-14: outlier percentages of beam structure magnitude estimations, noise free condition

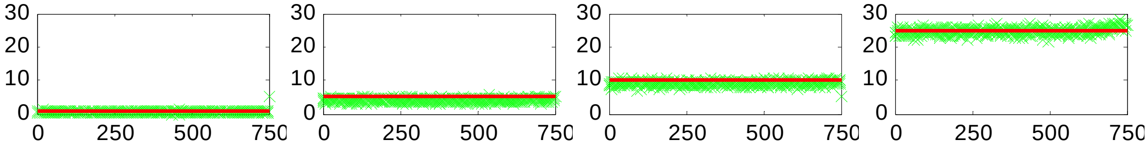

Figure 4-15: outlier percentages of beam structure magnitude estimations, noise contaminated condition

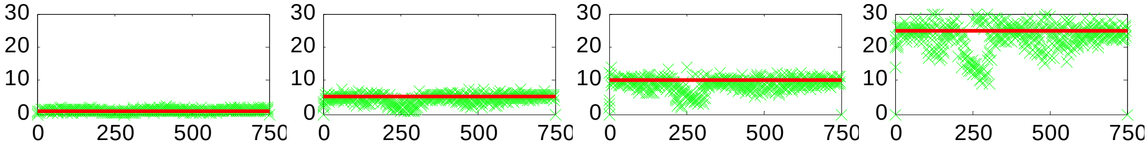

Figure 4-16: outlier percentages of beam structure phase estimations, noise free condition

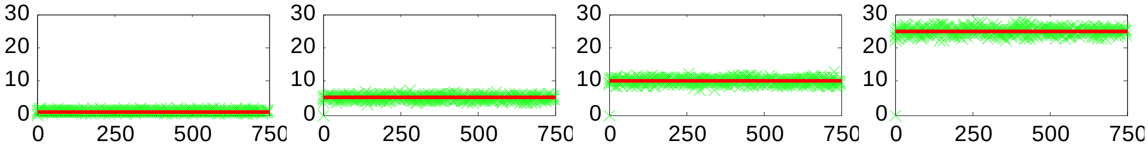

Figure 4-17: outlier percentages of beam structure phase estimations, noise contaminated condition

4.3. Plate structure

4.3.1. Structure description

Unlike simulation data, where the external noise level is well-controlled (and even eliminated), we validate the statistical models with tests on a more realistic structure. A clamped plate, which is well isolated from ground noise and the mechanical coupling from shaker, shown in Figure 4-18, is tested, and input force and output acceleration are measured simultaneously. In this test, both input and output measurements are subject to external uncertainties, although the experiment is fairly well-controlled within a laboratory setting. To be more severe, the lab data obtained from sensors are also contaminated with extraneous artificial Gaussian white noise to study the consequence of lower signal-to-noise ratio due to external noise influences.

Figure 4-19 shows locations of responses, and arbitrarily in this section, FRF is calculated between response at IP#2 and excitation and transmissibility is calculated between IP#2 and #4.

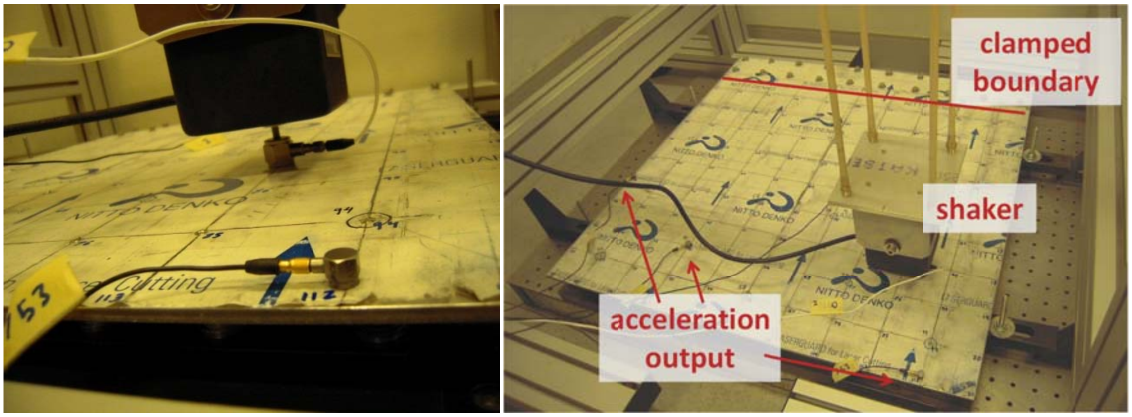

Figure 4-18: plate structure setup

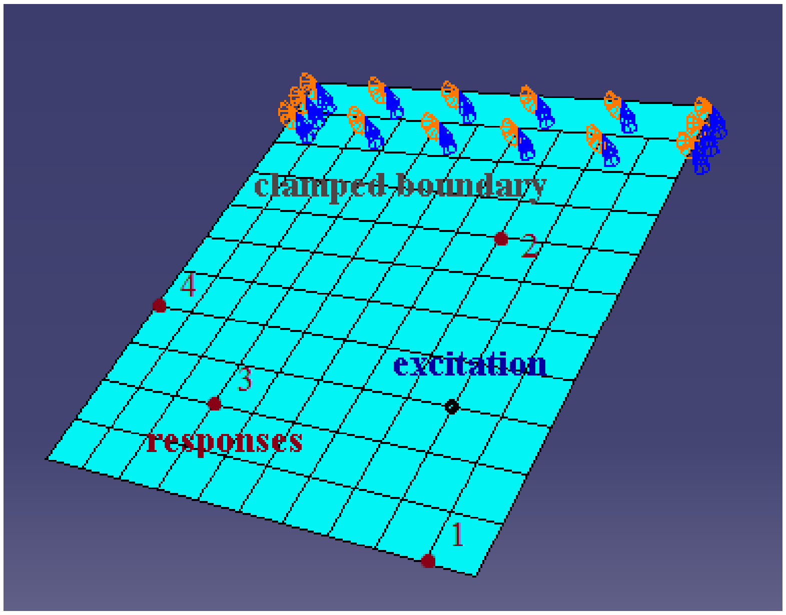

Figure 4-19: plate structure setup

4.3.2. Validation of FRF magnitude and phase

Magnitude and phase estimations of the plate structure are plotted in Figure 4-20, also with 90% of significance interval. Compared to the results of beam simulation without external noise (Figure 4-11), the distribution of plate estimations for non-contaminated condition is apparently wider, because of the naturally unavoidable noise in the measurements. As the measurements get further contaminated by artificial noise, the uncertainty bounds with 90% of confidence become more separated.

Figure 4-21 shows the same observation more directly by overlapping the histogram of estimations with modeled probability density and 90% quantiles at a single frequency line (arbitrarily picked at 332 Hz). Despite of the good consistency between proposed statistical models and histogram, there is a slight skewness of the histogram in Figure 4-21(b), indicating the predicted PDF does not fully characterize the actual distribution. The reason is that the magnitude estimations cannot be negative numbers, even though the final probability density model was defined for the entire real field. As a result, at those frequency lines with small estimations, the left tail of the predicted PDF will traverse the negative side and mismatch the histogram. Thus, for some of those special cases, the left quantile is negative and cannot be illustrated in logarithm scale, as shown in frequency region 0 to 100 Hz in Figure 4-20(b).

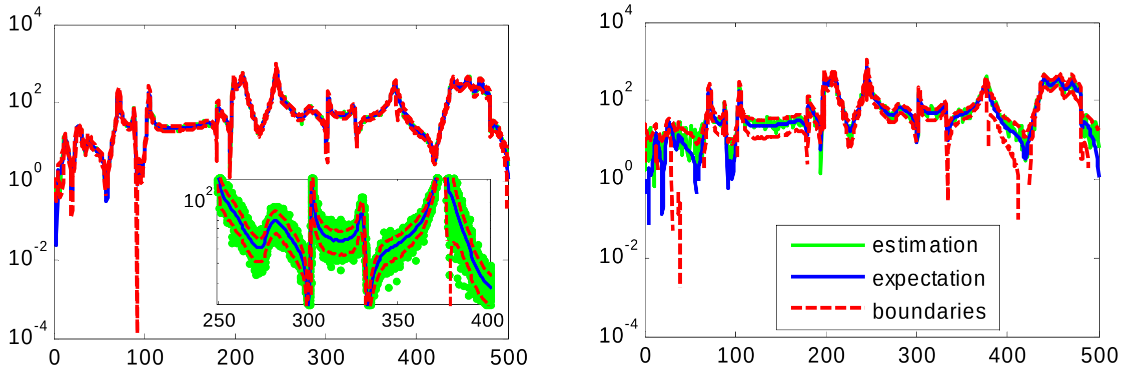

(a) magnitude estimation, noise free (b) magnitude estimation, noise contaminated

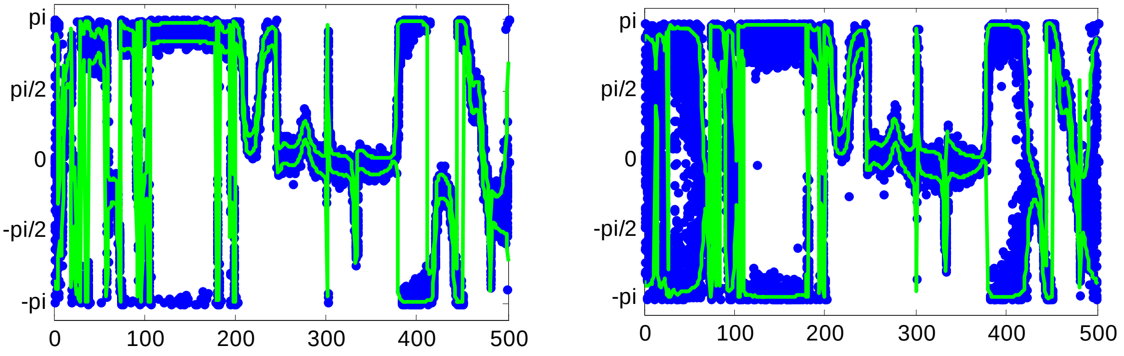

(c) phase estimation, noise free (d) phase estimation, noise contaminated

Figure 4-20: FRF estimations of plate structure with 90% of confidence interval

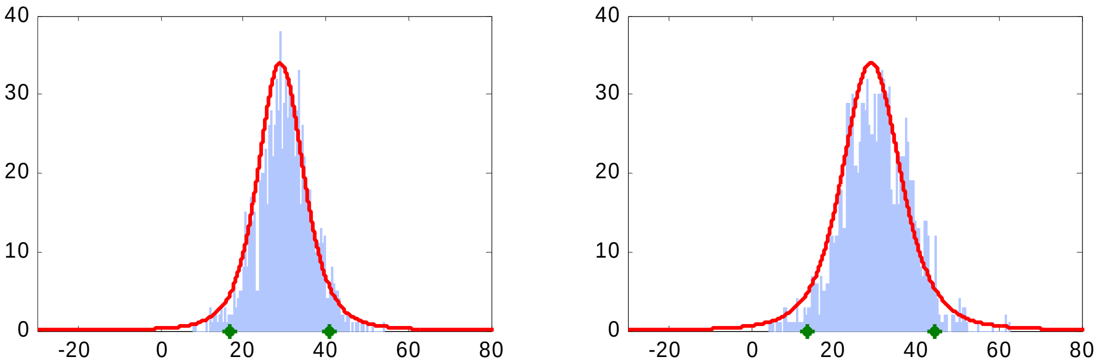

(a) magnitude estimation, noise free (b) magnitude estimation, noise contaminated

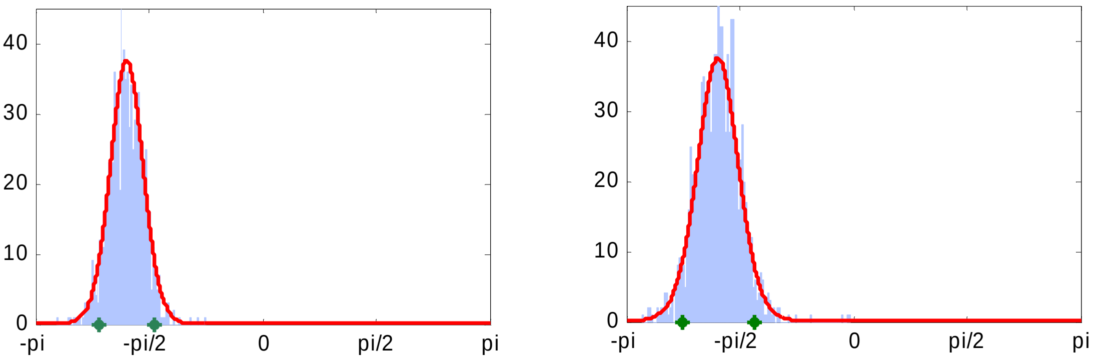

(c) phase estimation, noise free (d) phase estimation, noise contaminated

Figure 4-21: histogram of plate structure estimations at single frequency line with characterized distribution and 90% quantiles

After visually check the distribution of single frequency line and the 90% confidence interval of magnitude and phase estimation, the outlier percentages versus frequency are plotted through Figure 4-22 to 4-25. Due to the existence of noise even for the original data claimed to be “external” noise free, the outlier percentage plots are more stable over frequencies compare to the results shown in Figure 4-14 to 4-17. One thing needed to be addressed is that there is a small underestimation for some of the subplots for magnitude estimation outliers in Figure 4-22 and 4-23, such as the 95% and 90% significance. This indicates the miss-match of predicted distribution with real histogram, due to the skewness previously mentioned in Figure 4-21 for non-negative magnitude, and also the slight violation of Gaussian assumption made before statistical modeling. There is also possibly slight nonlinearity in the structure, which clearly is not controllable, that can distort the statistics. This issue will be discussed in section 4.4.

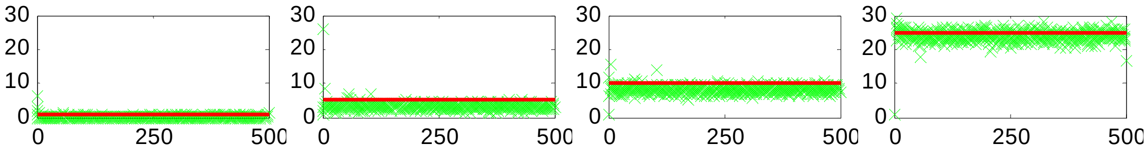

Figure 4-22: outlier percentages of plate structure magnitude estimations, original data

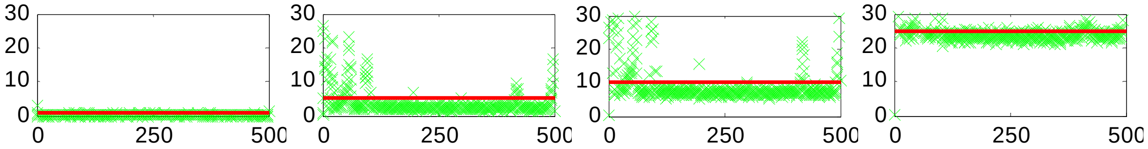

Figure 4-23: outlier percentages of plate structure magnitude estimations, noise contaminated data

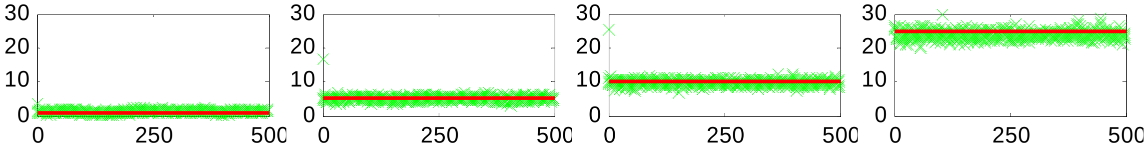

Figure 4-24: outlier percentages of plate structure phase estimations, original data

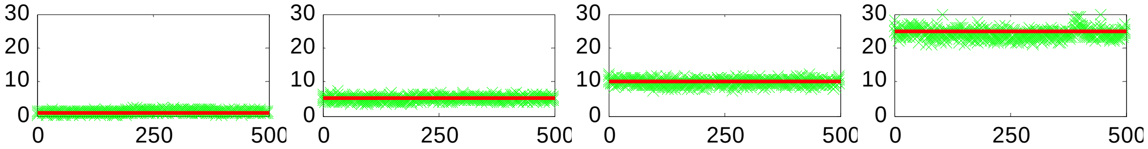

Figure 4-25: outlier percentages of plate structure phase estimations, noise contaminated data

4.3.3. Validation of transmissibility magnitude and phase

Using the same plate structure, transmissibility, both magnitude and phase, are estimated from the measured data for many testing rounds in order to compare with the predicted distributions. Again, to simulate in-situ testing, the data are contaminated with artificial white noise to make the environment stricter and estimations more realistic.

Figure 4-26 plots the magnitude and phase estimation of transmissibility for both noise free and contaminated conditions, with 90% of confidence boundaries also shown. For condition with extraneous noise, the estimations become much more variable, and accordingly, the confidence boundaries given by the statistics models are more widely separated.

For magnitude estimations, the predicted expectations at all the frequency lines are also plotted. It is clear to see the consistency between the expectation (blue) and the noisy estimations (green) from Figure 4-26(c), but not as clear from Figure 4-26(a) because the estimation itself is very good , and all the curves fall on top of each other. In some region of Figure 4-26(c), such as 0~150Hz, the lower bound is not plotted. This is because the magnitude is always positive, but the probability density function in Equation (3-33) is evaluated in the entire real number field. For these areas, the lower boundary is evaluated to be negative so that cannot be plotted in logarithm scales. This issue, same as the problem in FRF magnitude distributions, will be discussed in the next section.

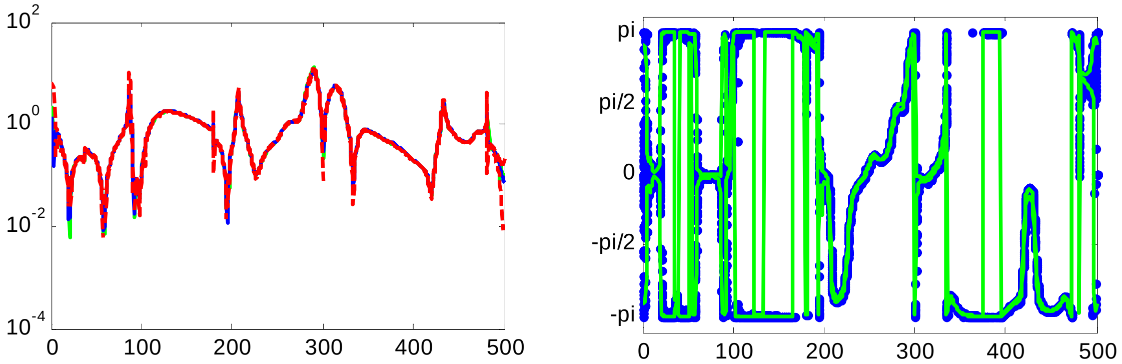

(a) magnitude, noise free condition (b) phase, noise free condition

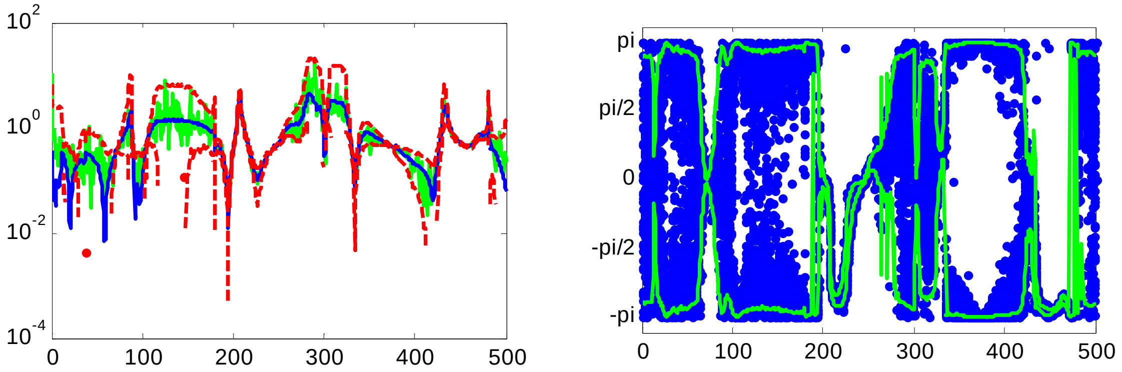

(c) magnitude, contaminated condition (d) phase, contaminated condition

Figure 4-26: transmissibility estimations of plate structure with 90% of confidence interval

Phase estimations are plotted in the wrapped way to better show the noisy estimation with corresponding boundaries. Due to the noise influence, unwrapped phase estimations from different experiments will have multiple 2π intervals, and make each round of estimations hard to be compared.

In Figure 4-27, histograms of magnitude and phase estimations are shown at an arbitrary frequency line, with the probability density curve given by the statistical models presented before.

Green stars are the 5% and 95% of significance, also given by the statistical models. Histograms show good consistency at this frequency line with the modeled distribution, and for noise-contaminated condition all the estimations are wider distributed.

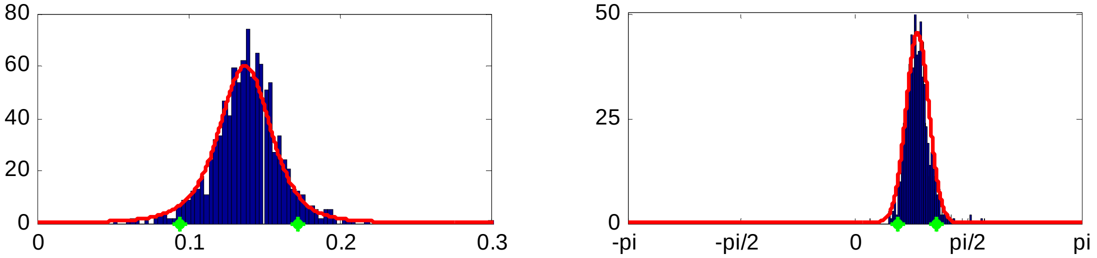

a) magnitude, noise free condition b) phase, noise free condition

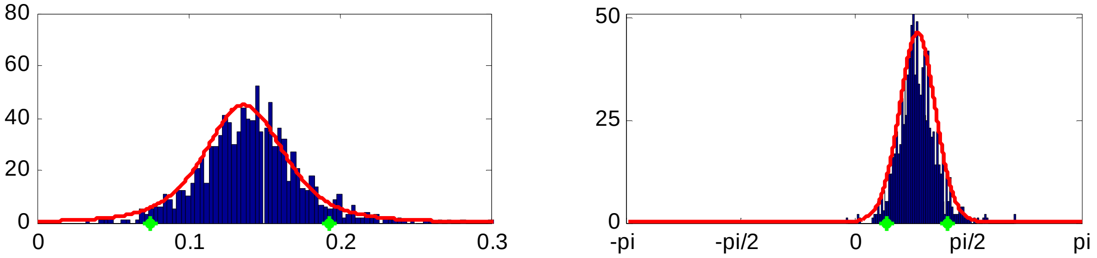

c) magnitude, contaminated condition d) phase, contaminated condition

Figure 4-27: histograms and predicted distributions of transmissibility estimations in plate structure

For a more systematic validation of the statistical models presented in Equation (3-33) and (3-44), a significance level is set to be 90%, and at all the frequency lines, outlier percentage is evaluated. Figure 4-28 shows the observed outlier percentages along entire frequency domain, and the 10% anticipation is plotted in red line as a reference.

Under noise-free condition, the models work very well as Figure 4-28(a, b) illustrates.

Among all the frequency lines, the statistical models give stable and consistent outlier predictions. For the conditions with artificial noise, which is a stricter test condition, although the general trend is still consistent, the stationarity of outlier percentage is getting poor. However, the test data obtained have a fixed length; therefore there is limited opportunity to improve the number of averages n_d in order to reduce the noise influence. But in fact, the estimator in Equation (2-9) does converge to the true value as n_d increases, and thus the statistical models will have improved performance with increasing number of averages.

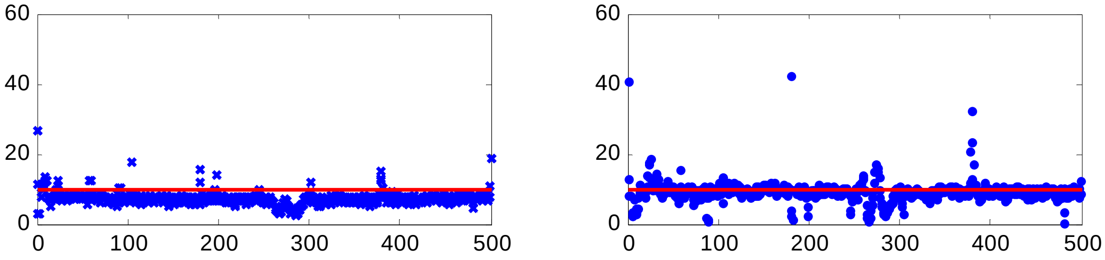

(a) magnitude, noise free condition

(b) phase, noise free condition

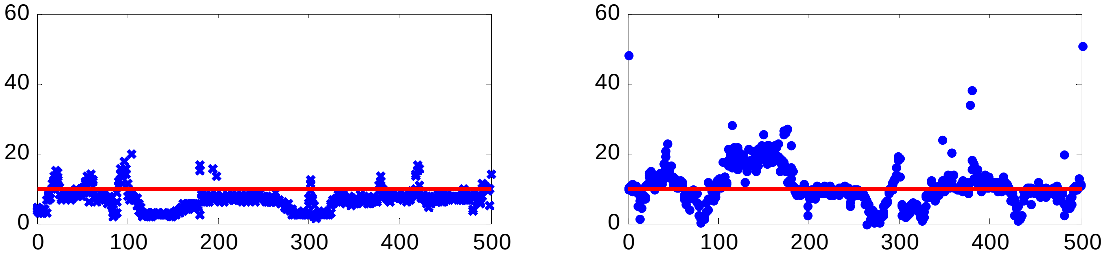

(c) magnitude, contaminated condition

(d) phase, contaminated condition

Figure 4-28: transmissibility outlier percentages of plate structure estimations

4.4. UQ models comparison

In this Chapter, Monte-Carlo tests from different structures are implemented to validate statistical models of transmissibility and FRF established in Chapter 3. There are uncertainty models for different magnitude and phase estimators, which require different information from random excited inspections.

Uncertainty model obtained from perturbation approach only requires output series, from which the bias and deviation of transmissibility magnitude are expressed in coherence function. This quantifies uncertainty in the fastest way with least calculation consumption, but only gives order statistics without fully characterizing the distribution. For the Chi-square bivariate approach, the estimator of transmissibility is compatible with output-only data and this is useful for the situation where input excitation is ambient or unable to be measured. The Chi-square bivariate uncertainty model quantifies transmissibility and FRF estimated through auto-power density functions, and the estimators are biased if the *NSR* is not negligible. In other words, the estimator is not accurate but the statistical model accurately describes the full distribution. For magnitude estimations through cross-power densities and phase estimations through real and imaginary parts, statistical models are established via Gaussian bivariate method, and these models are overall the most stable and robust models with noise influence. Having enough averages, the Gaussian bivariate models work very efficiently, although they are approximate models. In the plate test, limited by certain data acquisition parameters, the data collected are sufficient for only eight averages, which is way less than the number of averages in other simulation tests. As a result, the auto/cross power density estimations are not Gaussian distributed enough to permit this model to accurately characterize the uncertainties. In other words, by improving the number of average in spectral estimation, the normality will be improved, leading to greater consistency with Gaussian modeling assumptions.

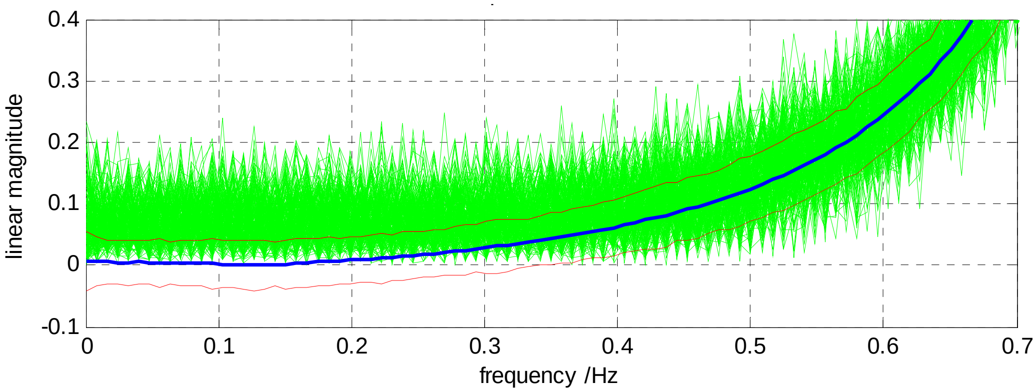

Figure 4-29: zoom-in of poor uncertainty quantification when the magnitude is small

Figure 4-29 shows the aforementioned limitation of the magnitude uncertainty model established via Gaussian bivariate approach, being addressed in Figure 4-20(b) and 4-26(c). Because the assumption of normality does not consist the non-negative fact of power spectrum magnitude, the lower bound in Figure 4-29 (or left tail of distribution) traverses below zero, when the true magnitude (blue) is very small. Moreover, increasing number of averages will reduce the variation of estimates and therefore better performance for the statistical model to capture the skewed distribution in the positive domain and avoid the negative tails. Figure 4-30 illustrates how the negative left tails and non-zero skewness are avoided by increasing number of averages, and meanwhile the normality is improved.

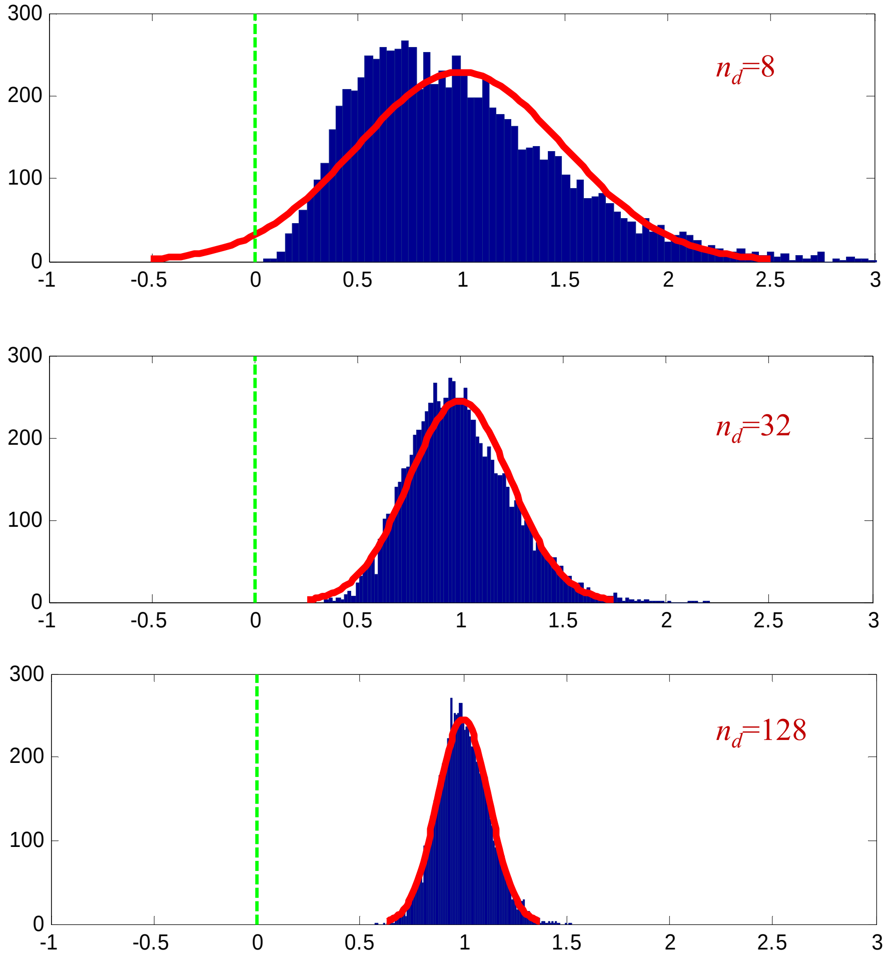

Figure 4-30: avoiding negative left tails and improving normality

With uncertainty fully characterized by means of the proposed PDF models, there is a clearer picture of the actual distribution of transfer function estimations, which is very useful for system identification and health monitoring/damage prognosis applications and other related areas. Given the distribution of estimations, it is possible to detect statistical significance, which in the context of structure health monitoring, is used in hypothesis testing for damage detection. Consequently, with the significance level provided by the statistical models established, a quantitative understanding of the estimations is obtained and also a quantified confidence for decision making of any kind that relies on the estimations.

This chapter, in part, has been published in *Proc. SPIE 7650*, Zhu Mao and Michael Todd, 2010. The title of this paper is “A structural transmissibility measurements-based approach for system damage detection”. The dissertation author was the primary investigator and author of this paper. A portion of this chapter has been published in *Mechanical Systems and Signal Processing*, Zhu Mao and Michael Todd, 2012. The title of this paper is “A model for quantifying uncertainty in the estimation of noise-contaminated measurements of transmissibility”. The dissertation author was the primary investigator and author of this paper. A portion of this chapter has been submitted to *Mechanical Systems and Signal Processing*, by Zhu Mao and Michael Todd. The title of this paper is “Statistical modeling of frequency response function estimation for uncertainty quantification”. The dissertation author was the primary investigator and author of this paper. A portion of this chapter has been published in *Proc. SPIE 8348*, Zhu Mao and Michael Todd, 2012. The title of this paper is “Uncertainty propagation of transmissibility-based structural health monitoring features". The dissertation author was the primary investigator and author of this paper. A portion of this chapter has been submitted for publication in *Proceedings of the ASME 2012 Conference on Smart Materials, Adaptive Structures and Intelligent Systems, SMASIS 2012-7935*, Zhu Mao and Michael Todd, 2012. The title of this paper is "The quantification of uncertainty in SHM features derived from frequency response estimation". The dissertation author was the primary investigator and author of this paper.

5. Application to damage identification by hypothesis testing

In Chapter 3, multiple statistical models were established by which the uncertainty levels in various FRF and transmissibility estimators were quantified, and in Chapter 4 those models were validated via Monte-Carlo testing by comparing outlier percentages in observations with the significance level of boundaries computed from the models. These estimators are often directly used in outlier detection (unsupervised learning) modes for the damage detection problem via binary hypothesis testing, although no claim is made that these are optimal detection tools displaying good sensitivity and specificity.

5.1. Damage identification paradigm

5.1.1. Damage detection in FE cubical model

In section 2.2, a contrived satellite with cubical shape was a surrogate data source, and in section 4.1, the derived standard deviation of transmissibility magnitude estimation was validated with structural response under white noise excitations. For a given confidence level, the upper and lower error bounds of transmissibility estimation may be computed, so two new metrics are proposed to evaluate the results: (i) calculate the amount/percentage of outliers *OP* at each frequency point, or the average over the whole frequency domain, which has been used for model validation in section 4.1:

$$OP = 1 - \frac{\sum_{l=1}^{n_{bin}} \left[\underline{B}(l) \le T(l) \le \overline{B}(l) \right]}{n_{bin}}. \tag{5-1}$$

where $\underline{B}(l)$ and $\overline{B}(l)$ are the lower and upper bounds of uncertainty with certainty significance setting at l^{th} frequency bin; meanwhile, (ii) calculate all the outliers' root-mean-squared distance to the uncertainty bounds (*RMSE*), as shown in Equation (5-2):

$$\forall l \in \left[1, n_{bin}\right], \text{ define } \begin{cases} Q(l) = \underline{B}(l) - T(l), & T(l) \in \left(-\infty, \underline{B}(l)\right) \\ Q(l) = 0, & T(l) \in \left[\underline{B}(l), \overline{B}(l)\right], \\ Q(l) = T(l) - \overline{B}(l), & T(l) \in \left(\overline{B}(l), +\infty\right) \end{cases}$$

and therefore:

$$RMSE = \sqrt{\frac{1}{n_{bin} - 1} \left(\sum_{l=1}^{n_{bin}} Q^2(l) \right)}. \tag{5-2}$$

In *RMSE* definition, only the root-mean-square error of outliers is counted, and Figure 5-1, as an example, illustrates how far away the outliers exist beyond the error bounds. Because both *OP* and *RMSE* metric evaluate the average outlying level among all frequency bins, it is different from Monte-Carlo simulation and does not require many trials, although averaging among multiple tests will make these metrics more stable predictors.

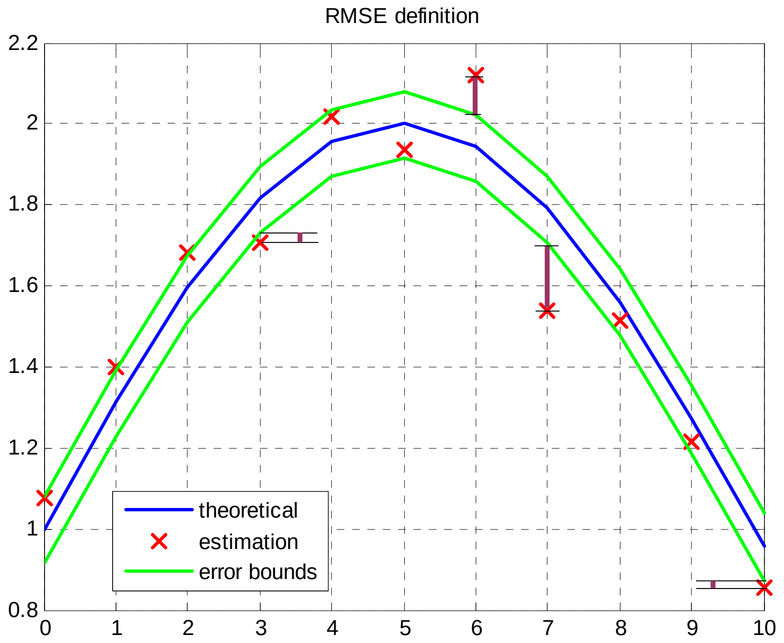

Figure 5-1: root-mean-square metric illustration

Implementing Gaussian excited simulation on the aforementioned FE model with damage pre-set as shown before in Figure 2-5, with each level of stiffness change defined in Figure 2-6, both *OP* and *RMSE* metrics for the baseline and damaged transmissibilities between two arbitrary IPs are calculated and plotted in Figure 5-2 and 5-3, with center-located excitation and off-center excitation, respectively.

From the four plots, there are some qualitative observations: (i) if the damage is small, i.e. a damaged stiffness that is close (a few percent) to that of the frame stiffness, the *OP* and *RMSE* are a little larger than the metrics obtained from baseline cases, no matter where the excitation is; (ii) if the damage is severe, i.e. the damaged stiffness is small enough compared with the structural stiffness, then the metrics become saturated as the stiffness decreases further, zero stiffness for the furthest, and nearly 100% of the estimations are beyond the error bounds; (iii) there is certain region of "moderate" damage, where both metrics are monotonic with the loss of connecting stiffness, and compared to small and severe damages, this region has good sensitivity of damage severity.

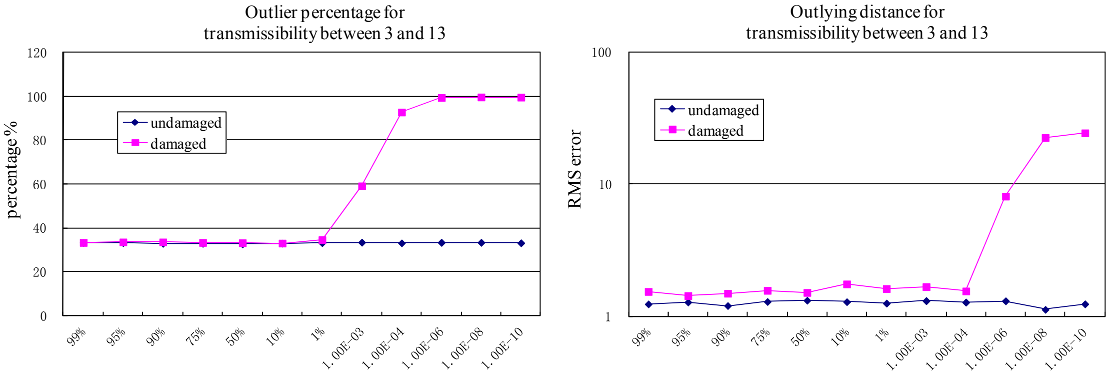
Outlier percentage for transmissibility between 3 and 13

Outlying distance for transmissibility between 3 and 13

Figure 5-2: *OP* and *RMSE* for center excitation results

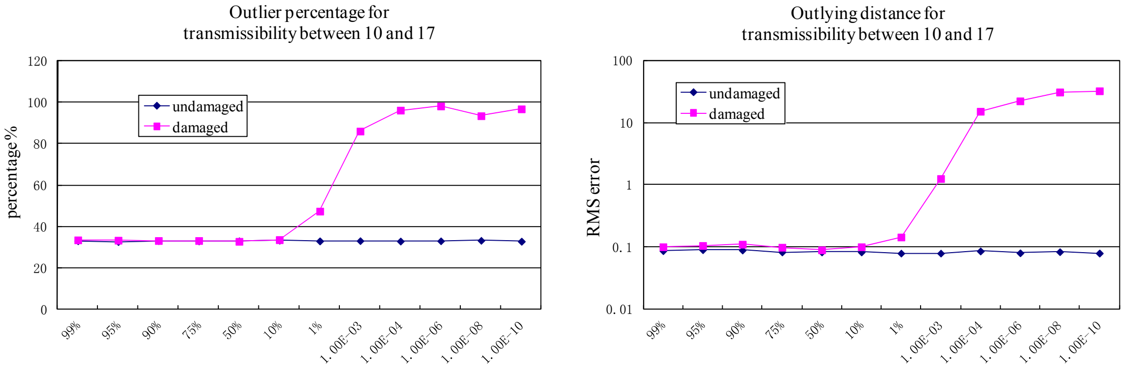
Outlier percentage for transmissibility between 10 and 17

Outlying distance for transmissibility between 10 and 17

Figure 5-3: *OP* and *RMSE* for offset excitation results

From the results presented in Figure 5-2 and 5-3, which are from single test, the *OP* and *RMSE* between lightly-damaged conditions and baseline can be barely distinguished. However, extraneous noise existence will cause uncertainty in the transmissibility estimation, and therefore propagates into any features used in the damage detection problem. For these lightly-damaged cases, it may occur that the damaged *OP* and *RMSE* drop below some the undamaged metric evaluations. To visualize this issue regarding damage detection, there are 128 rounds of tests for several damage levels (from 99% down to 10% of original stiffness) implemented, and the group results with baseline cases are compared.

Figures 5-4 and 5-5 show a very clear picture of damage detection for light stiffness degradation, using offset excitation as example. For 100% of the original stiffness, the damaged structure is identical to the undamaged one, except for the contaminated noise (external uncertainty in each run), and the *OP* and *RMSE* from both groups agree very well, so the mean value (marked as small circles) are very close. But for other conditions with degraded stiffness, the metrics disagree, which denotes damage existence.

Similar to the results in Figure 5-2 and 5-3, there is not perfect consistency and sensitivity observed for relatively heavier damage, i.e., those metrics do not increase accordantly. The reason is that the damaged/degraded stiffness may be still relatively high, so that the dynamics from frame dominates the response. Comparing the two metrics, a cursory conclusion can be made that the *OP* metric would be the better to detect the damage, because there are no intersections for damaged and undamaged values according to Figure 5-4 and 5-5.

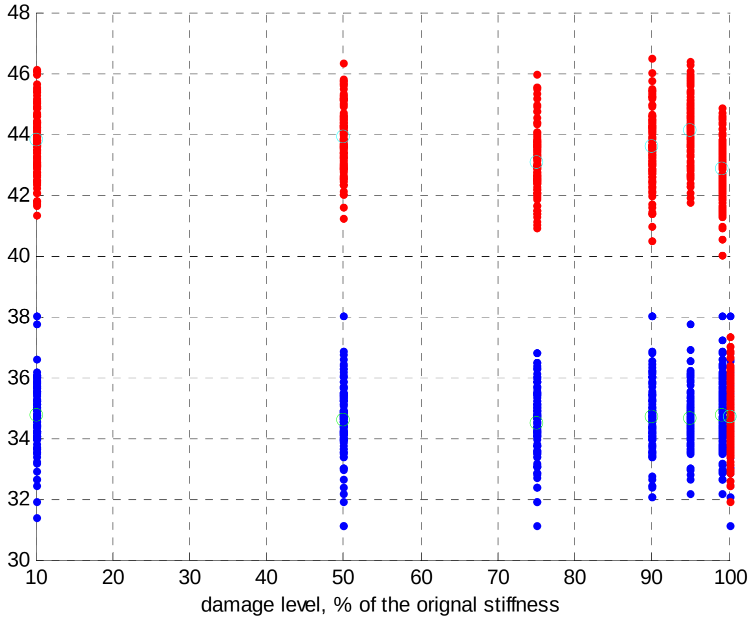

Figure 5-4: *OP* for light damaged cases

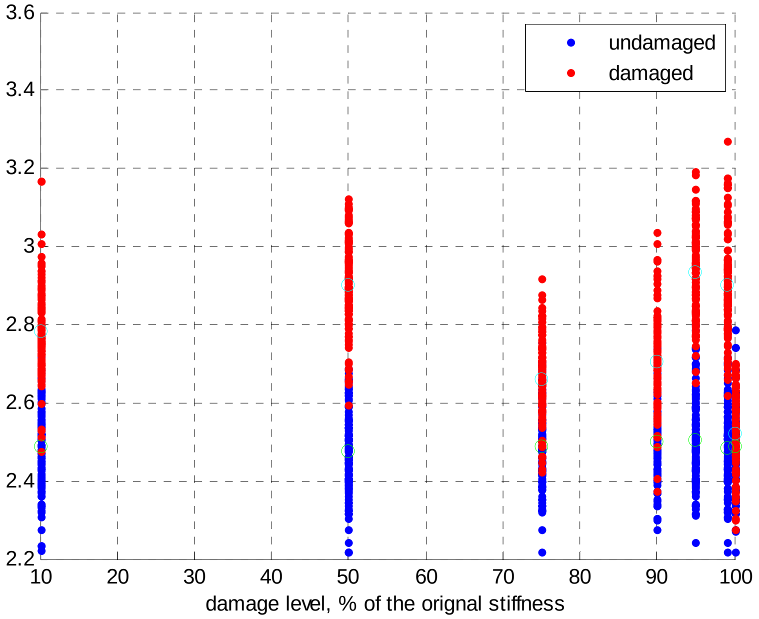

Figure 5-5: *RMSE* for light damaged cases

5.1.2. Damage detection in plate model

An external spring is placed underneath the plate structure introduced in section 4.3 as structural damage (a local stiffness perturbation), as shown in Figure 5-6, and transmissibility magnitude is estimated between IP #2 and #4, using different estimators. In this section, the outlier threshold is fixed to be 90%, (for perturbation model without PDF available, threshold is picked as ±1σ,) and compare the outlier percentage of every UQ model, with different noise contamination conditions. Corresponding confidence bounds are calculated from the three uncertainty models derived in Chapter 3.

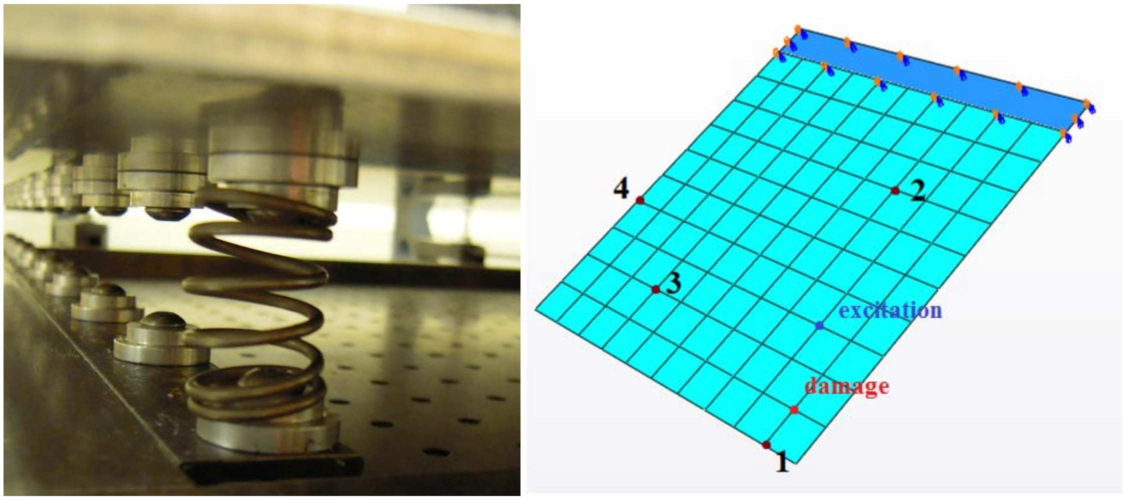

Figure 5-6: test structure and spring damage

Figure 5-7 shows again the estimated transmissibility magnitude and uncertainty bounds given by a different UQ model. The left column of Figure 5-7 represents the extraneous noise free condition, which means the uncertainty is primarily from well-controlled lab noise and the estimation algorithm itself; as a result, the estimations are very accurate, and all the confidence bounds are very close to each other. The right column of plots in Figure 5-7 represents the condition with 1% *NSR* Gaussian white noise added in order to simulate a more realistic environment with other sources of ambient noise and variability. For the noise-contaminated conditions, transmissibility magnitude estimations are corrupted with obviously larger uncertainty, but the quantification models also capture the change and reflect wider uncertainty intervals.

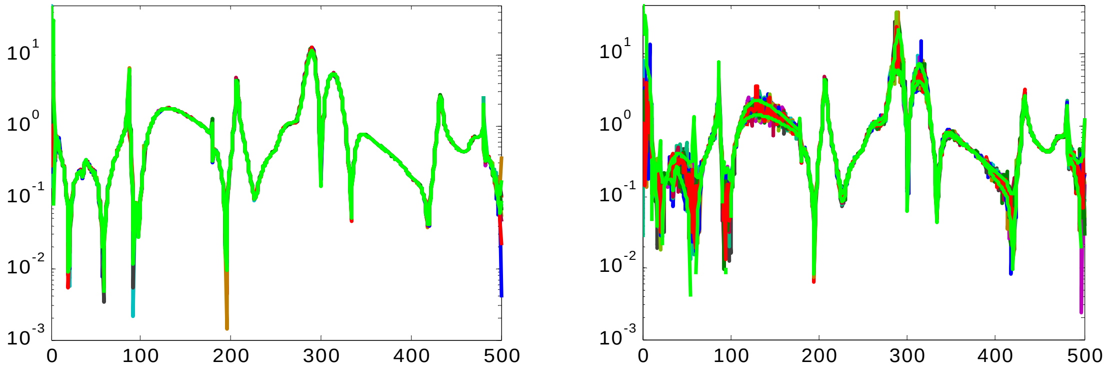

(a) ±1σ bounds, perturbation approach, noise free

(b) ±1σ bounds, perturbation bivariate, contaminated

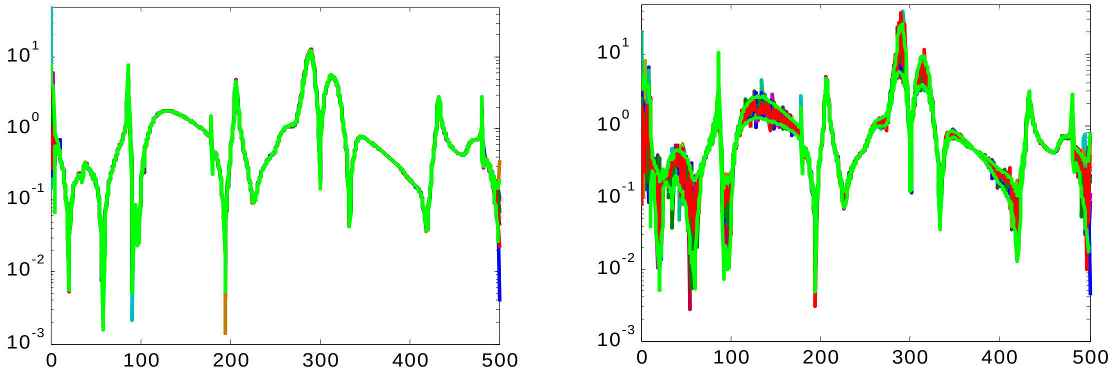

(c) 90% confidence, Gaussian bivariate, noise free

(d) 90% confidence, Gaussian bivariate, contaminated

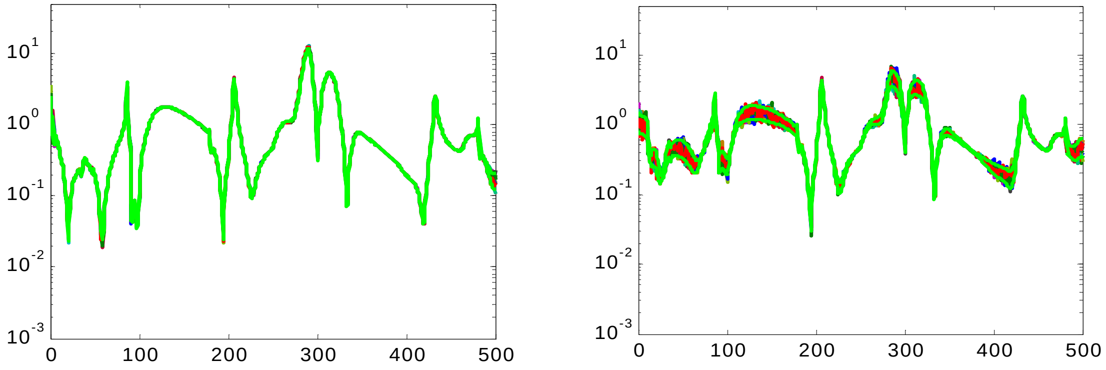

(e) 90% confidence, Chi-square bivariate, noise free

(f) 90% confidence, Chi-square approach, contaminated

Figure 5-7: undamaged transmissibility estimation between position 2 and 4, with confidence bounds plotted in green.

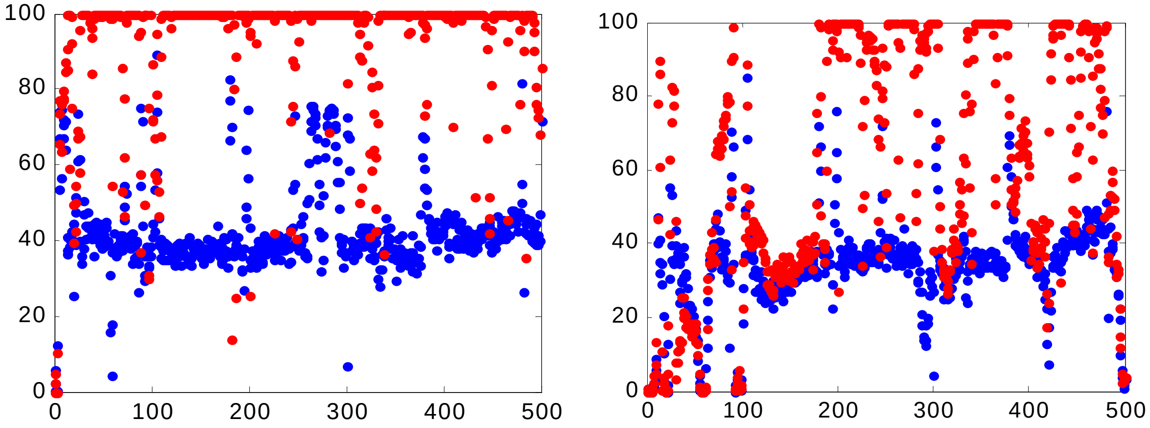

(a) Perturbation approach, noise free (b) Perturbation approach, noise contaminated

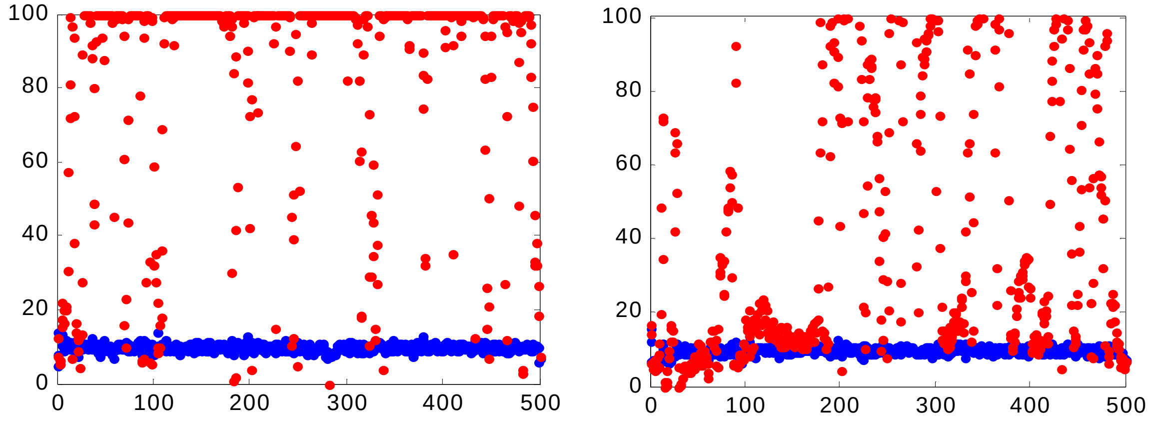

(c) Gaussian bivariate, noise free (d) Gaussian bivariate, noise contaminated

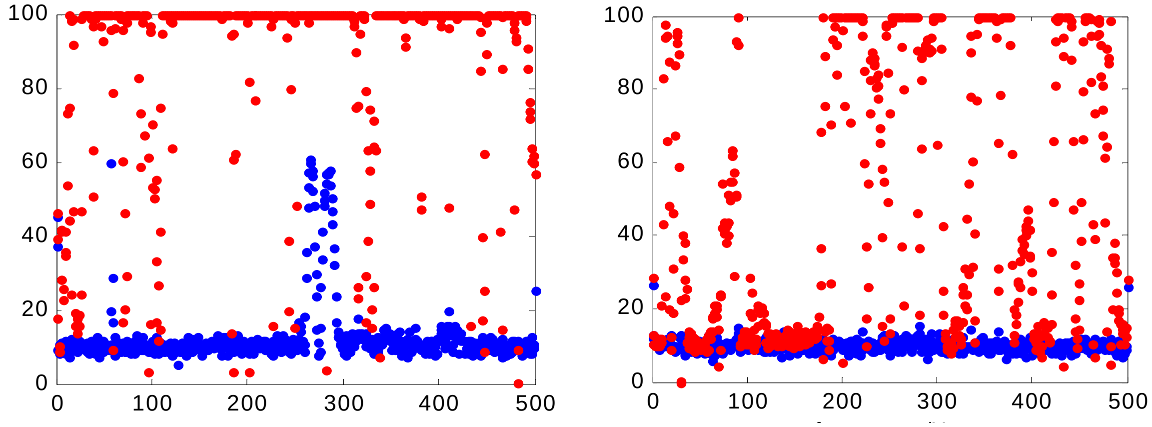

(e) Chi-square bivariate, noise free (f) Chi-square bivariate, noise contaminated

Figure 5-8: Transmissibility estimation outlier percentage at each frequency line, blue: undamaged condition; red: damaged condition

One observation from Figure 5-7(f) is that, unsurprisingly, the estimator expressed in Equation (2-11) involved with output auto-power density function does not require information from input. Consequently, when the extraneous noise is added onto outputs, the estimation quality degrades without the reference from input series, and sharp peaks and notches are not observed as in Figures 5-7(b, d).

Specific performance comparison among the methods may be achieved by comparing experimental outliers to predicted outliers (based on percentage). A 500-round Monte-Carlo test was implemented, and at every frequency line the uncertainty models were evaluated. The percentage of outliers was calculated and plotted in Figure 5-8. For statistical models established via Gaussian and Chi-square bivariate approaches, probability density functions are available, and the confidence level is set to be 90%, anticipating 10% outliers. For the statistical model given by perturbation approach, there is only standard deviation of estimations available, without full knowledge of the actual underlying distribution; therefore in Figure 5-7(a, b) and 5-8(a, b) only the estimations and outlier percentages bounded by one standard deviation limits are plotted for fair comparison.

From the outlier percentage plots in Figure 5-8, it can be concluded that all the uncertainty models are stable in different frequency lines and different noise contamination conditions, and all are sensitive to capturing the structural parameter changes. For extraneous noise-free conditions, a dramatic increase of outlier observations is present, no matter which quantification model is applied. When the measurements are suffered to extraneous noise, the outlier detection can still capture most of the statistical significances.

There is a very narrow frequency region below 300 Hz for the noise free condition in Chi-square outlier percentage plot (Figure 5-8(e)) where baseline values are not as consistent with the pre-set confidence threshold. This is because of a violation of the stationary Gaussian time series requirement, and therefore weak satisfaction of Chi-square characteristics in auto-power density magnitude. By increasing the length of measurement or adding extraneous Gaussian noise, the stationarity will become much better, and this can be seen from Figure 5-8(f).

From the entire frequency domain point of view, conclusions can be made that perturbation approach gives the fastest damage detection possibility, but it is not as stable or accurate as the other two. Gaussian bivariate approach is the most stable/reliable method in quantifying the confidence. However, once extraneous noise is present in measurements or the record is long enough to show stationarity, the Chi-square model also has very good performance for uncertainty quantification. From damage detection point of view, degradation can be seen from both Gaussian and Chi-square bivariate approaches once there is contamination, but the noise influence in estimations given by Equation (2-9) can be improved by increasing number of averages, hence outperforms the estimator in Equation (2-11). Therefore, Gaussian bivariate statistical model is the overall best-performing significance detection tool if a high number of averages are possible.

5.1.3. Damage localization in plate model

Continue studying the same data set obtained from plate structure, there are responses at four differrent locations from which FRFs and transmissibilities between different IPs can be estimated. Generally speaking, damage localization is complicated problem suffered to incompleteness of structural dynamics and dynamics coupling/influence between substructures. Therefore, only the orignal time series obtained without further artificial noise contamination is considered, in order not to get the problem too sophisticated.

Figure 5-9 listed twenty realizations for each one of all four transfer functions' magnitude, and both baseline and damaged conditions are included. All those estimations are overlapped on top of each other, and for some specific frequency regions, it is easy to visually distinguish the damaged/undamaged groups without quantitative evaluation, as circled in the figure for examples.

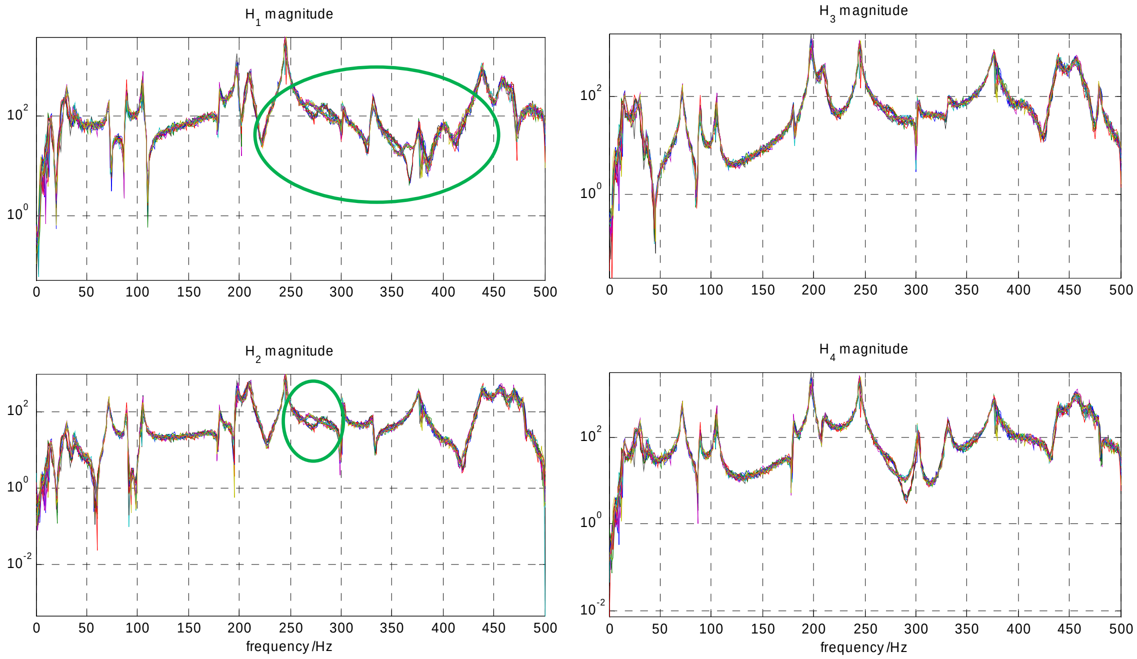

Figure 5-9: magnitude of transfer function H, at each measurement point

Figure 5-10 plot multiple realizations of phase estimation from both undamaged and damaged conditions, according to the same four FRFs. Red dots represent the estimations from damaged condition, and it is clear to see the non-overlapped estimations, and may suggest a better sensitivity of damage detection than magnitude estimation.

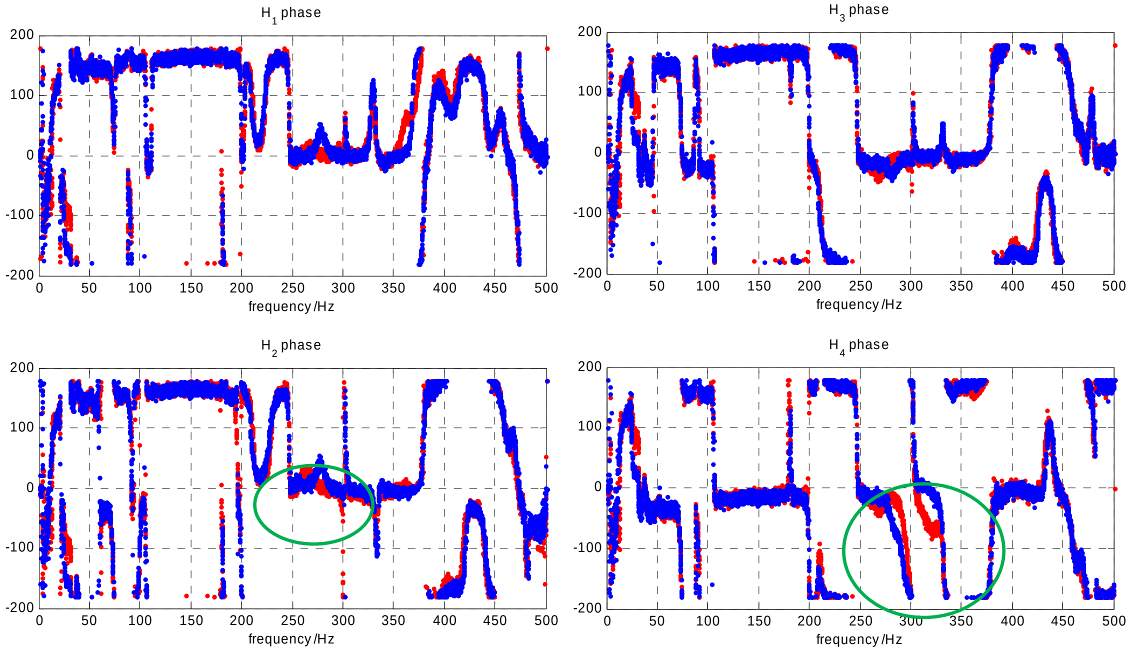

Figure 5-10: phase of transfer function H, at each measurement point

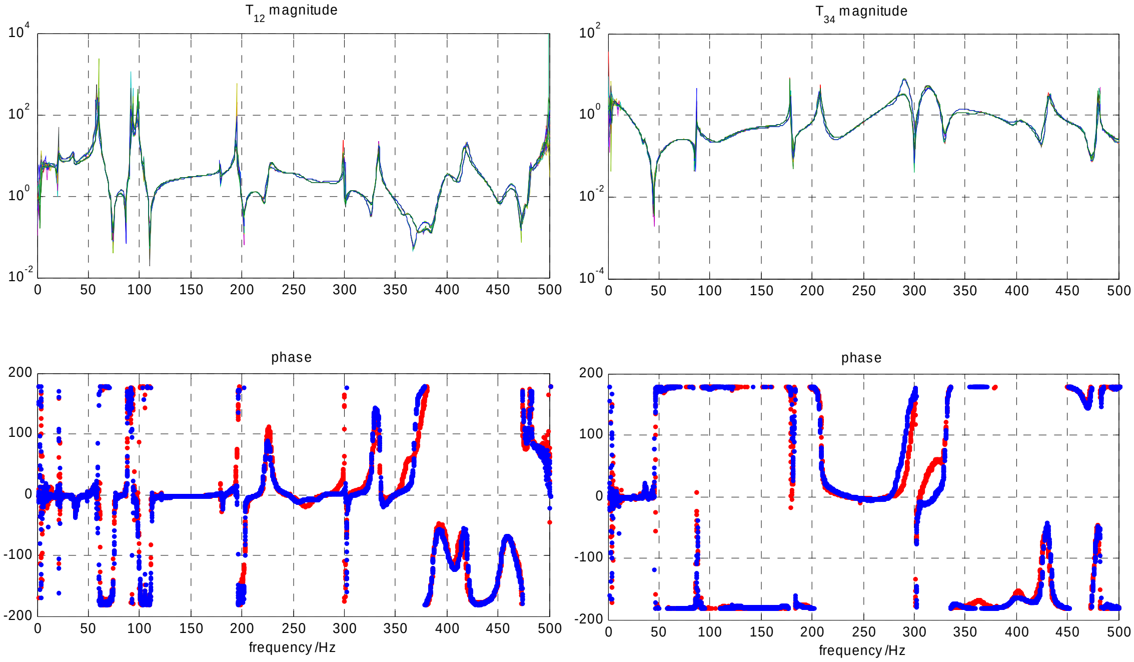

Figure 5-11: transmissibility T between 1~2 and 3~4

Similarly, transmissibility magnitude and phase estimations between IP locations 1~2 and

3~4 are plotted in Figure 5-11. Compared to Figure 5-9 and 5-10, the transmissibility estimation is much less fluctuating and has narrower uncertainty intervals, for both magnitude and phase. This could make transmissibility a more sensitive detector to capture the changes caused by system parameter change, which is damage in this context.

Adopting the magnitude and phase statistical models in Gaussian bivariate approach, there are decision boundaries with certainty confidence level available. Similar to previous work, two metrics are defined as expressed in Equation (5-3) and (5-4):

$$\overline{pct} = \frac{1}{n_{bin}} \sum_{l=1}^{n_{bin}} \left(pct_{(l)} - q \right), \tag{5-3}$$

$$MSE = \sum_{l=1}^{n_{bin}} \left(pct_{(l)} - q \right)^2 , \tag{5-4}$$

which are respectively the average outlier percentage over all the frequency lines and the mean square error of the outlier percentage offsetting from the pre-set threshold q, which is 10% here. Notation n_{bin} is the total number of frequency bins and $pct_{(l)}$ is the outlier percentage at l^{th} frequency line.

Evaluation of the metrics in Equation (5-3) and (5-4) are plotted in Figure 5-12, with the data from H_1, H_3, T_{12} and T_{34} taken into account. Both plots show metrics consistently overlapping in undamaged cases, and a clear separation in damaged cases, no matter what spectrum it represents. Metric evaluations for transmissibility are bigger than the evaluation for FRF, which indicates the previously mentioned better sensitivity of transmissibility, and in the meantime, the evaluations for H_1 and T_{12} are bigger than H_3 and T_{34} respectively, this could be caused by the location of damage, which is very close to the measurement point #1, referring to Figure 5-6.

Based on the data from this plate test, Figure 5-12 shows the feasibility using outlier analysis to localize structural defect. With a more refined sensing mesh, and thorough comparison between any combinations of measurement points for both magnitude and phase, there will be clearer and more robust localization decisions. Moreover, this outlier analysis should be synthesized with structural analysis, from which sensitivity of change of FRF/transmissibility could be studied, and correlation between metrics and locations will be better known since they might not be monotonically correlated.

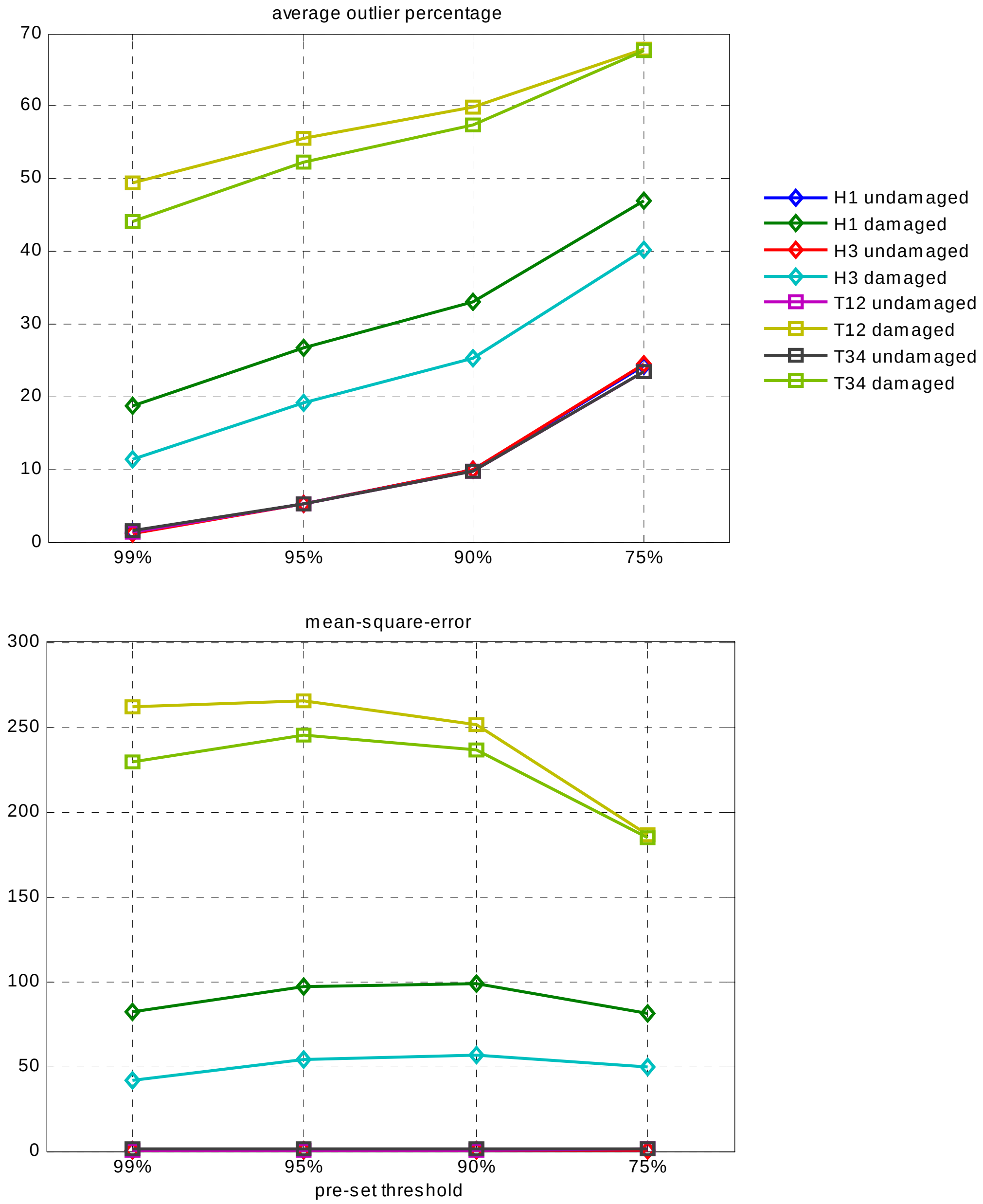

Figure 5-12: metric evaluation for transfer function magnitude outliers with different pre-set confidence threshold, upper: $\overline{pct}$; lower: MSE

5.2 Receiver operating characteristics (ROC)

In section 5.1, the damage detection and localization are implemented via quantified uncertainty bounds. The detection process is in fact statistical significance detection under hypothesis testing, which will be focused on in the next section. Here the question is raised: what is the performance, as measured in detection rate and false positive rate, of the approach developed in the last section? Receiver operating characteristics (ROC) is adopted to evaluate the detectability of each problem and suggest the best threshold for decision making.

A sample 3-DOF model is established, for implementing hypothesis test of transmissibility change detection, where analytical expressions of FRF and transmissibility are available from Equation (4-1) and (4-2). Figure 5-13 shows the structure where Gaussian noise is applied on mass #3 and corresponding responses are measured at the other two masses. The stiffness of spring #1 is tuned slightly to make the system change like damage presence. Figure 5-14 shows the cluster of analytical FRFs and transmissibilities of the structure, where the stiffness of k_1 drops from 100% to 99%, 98%, 97%, 95%, 90% and 75%, so the spectral curves shift accordingly to lower frequency. The left hand side y-axis is for FRF magnitude and the right hand side y-axis is for transmissibility magnitude, and all spectra are plotted in dB scale.

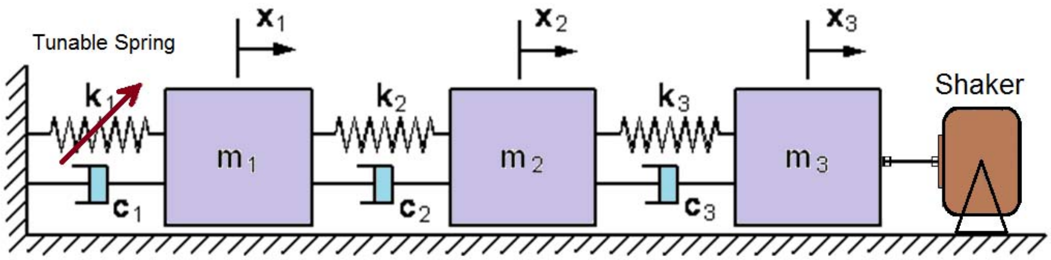

Figure 5-13: test structure used for hypothesis test

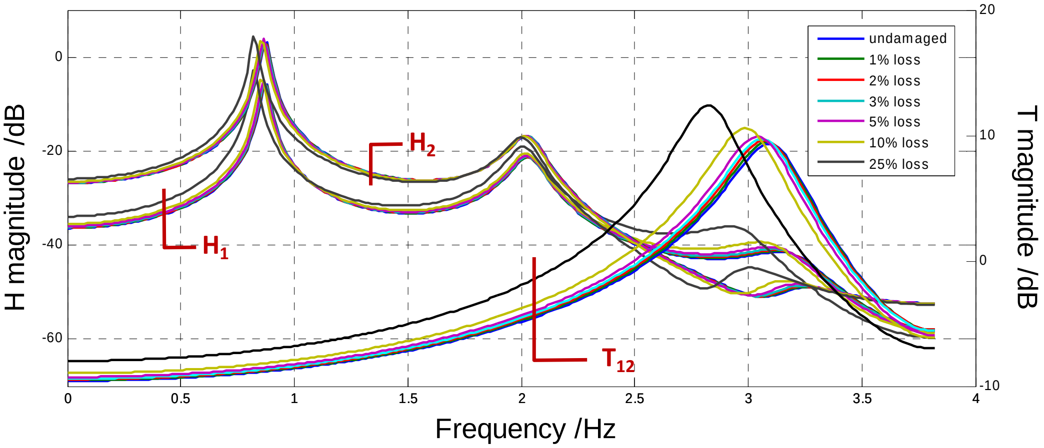

Figure 5-14: analytical transfer functions H_1, H_2 and transmissibility T_{12} spectra for different damage levels

A random process is applied onto the test structure to simulate a realistic system identification progress. Gaussian random series will be added to mass #3, and the estimation of transmissibility magnitude is evaluated from Equation (2-11), contaminated with different levels of independent Gaussian noise. In order to illustrate how noise affects the transmissibility estimation, and how the distributions for undamaged and damaged cases overlap, a small number of n_d=4 averages are chosen. In a real implementation, there will be many more averages made and the quality of estimation will be much better. Figure 5-15 plots the transmissibility estimations for different damage levels, and for 0, 1% and 10% of *NSR* levels.

Using the model given in Equation (3-28), the uncertainty of the estimation can be quantified, rather than qualitatively observing the curve shift, by determining if there is statistically significant separation between different sets of data. Two arbitrary frequency lines are picked as examples to evaluate the probability density and the operating characteristics below. The example frequency points are at 0.87 Hz, close to FRF resonance and having bigger input-output gain, and 3.12Hz, with low input-output gain.

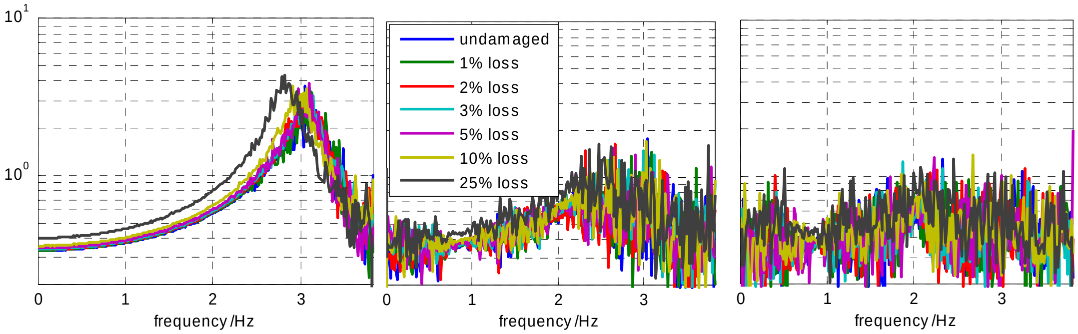

Figure 5-15: transmissibility estimations with n_d=4, left: no extraneous noise; middle: 1% *NSR*; right: 10% *NSR*

Figure 5-16 lists the probability density evaluations for three noise-contaminated conditions and at the mentioned two frequency lines. It can be seen both decrease of input-output gain, and more uncertainties and heavier overlapping in the distributions caused by noise contamination.

For an arbitrary threshold, there are true positives (true detections) and false positives (false alarms) existing simultaneously. As shown in Figure 5-17, with a random threshold represented by a vertical line, the area marked in green and yellow is false positive, while the area marked in red and yellow is true positive. In order to quantify the separation of distributions in Figure 5-16, the receiver operating characteristic (ROC) curves are calculated, which compare the true positive detection rates versus false positive rates for a given decision boundary (threshold); these curves are often used in detection optimization and decision making [96].

Figure 5-18 shows the ROC curves with the same groups of settings, and the results are consistent with the above qualitative observations. For the steepest curves, upper left one, the close-to-one true positive rate only costs an almost negligible number of false positives, and this means the distributions from different data sets can be completely separated, without any overlapping. Conversely, the lower right plot in Figure 5-18 shows the poorest binary classification among the six plots, which is not much better than random guess, and high/low true positive and false positive rates appear simultaneously. The 45° straight line corresponds to a random guess, meaning equal detections and false alarms like coin flipping.

Although the direction that the probability density curve moves toward is not monotonic with the stiffness loss, here in this Chapter, the null hypothesis is not changed to make the ROC curve always remain above random guess line (45-degree line). Therefore, a ROC curve that moves down and to the right (compared to a random guess) is also interpreted as equally optimal to the traditional interpretation of one that moves up and to the left.

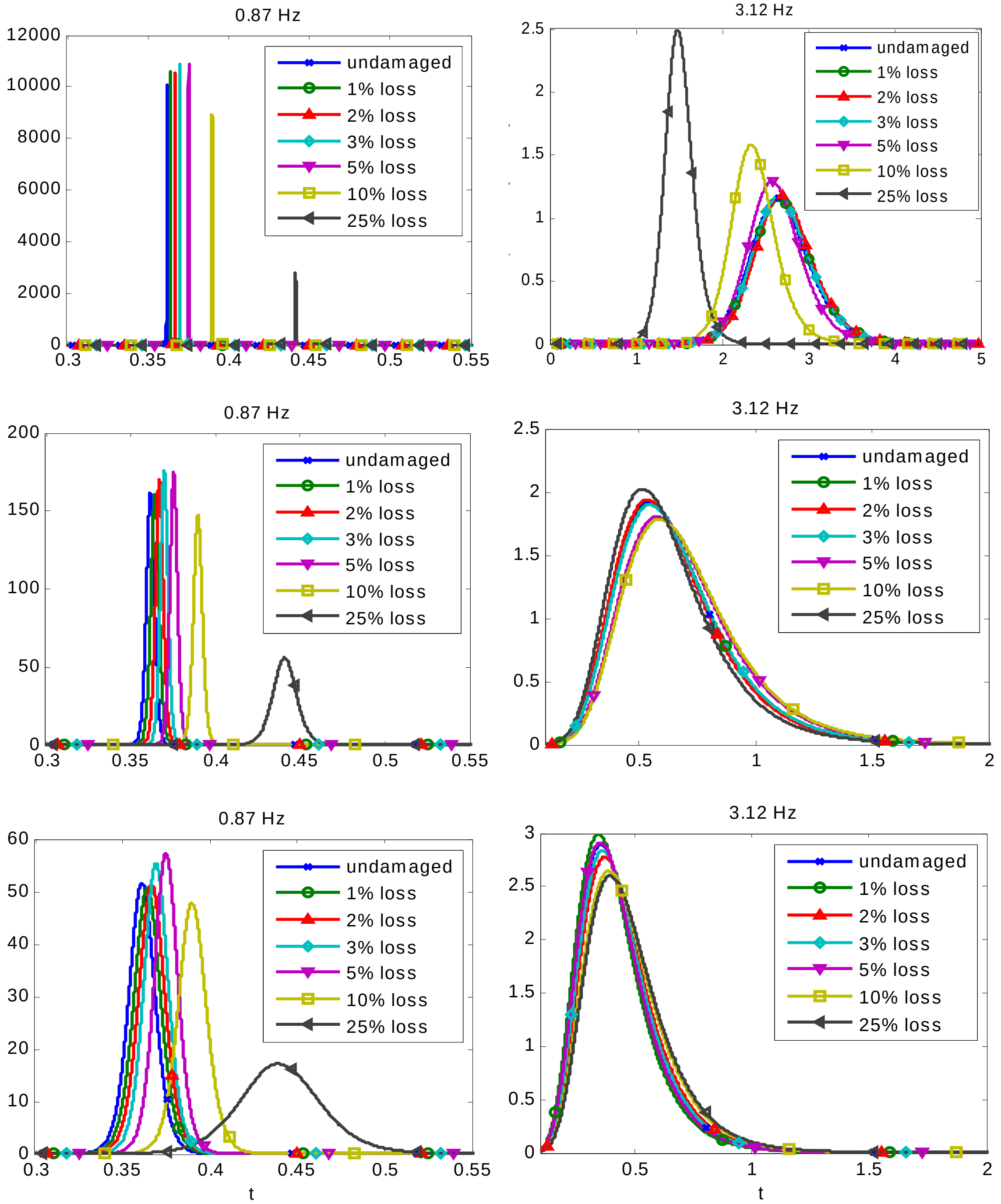

Figure 5-16: probability density function of transmissibility estimations for different damage levels. Upper left: 0.87Hz, external noise free; mid left: 0.87Hz, 1% *NSR*. Lower left: 0.87Hz, 10% *NSR*; upper right: 3.12Hz, external noise free; mid right: 3.12Hz, 1% *NSR*; lower right: 3.12Hz, 10% *NSR*

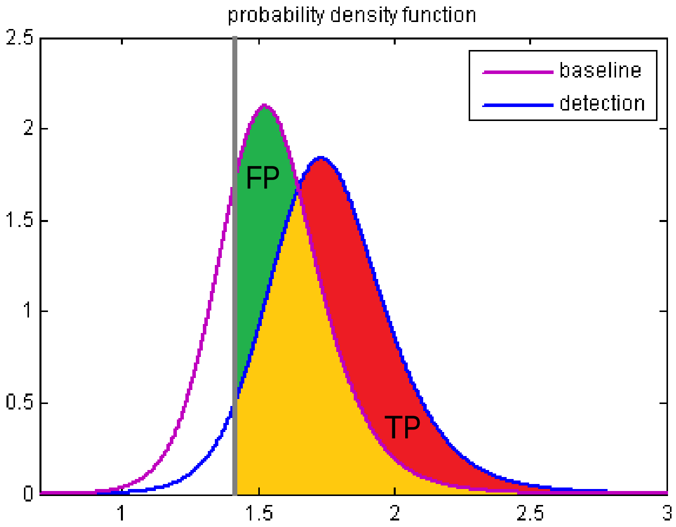

Figure 5-17: true positive rate and false positive rate

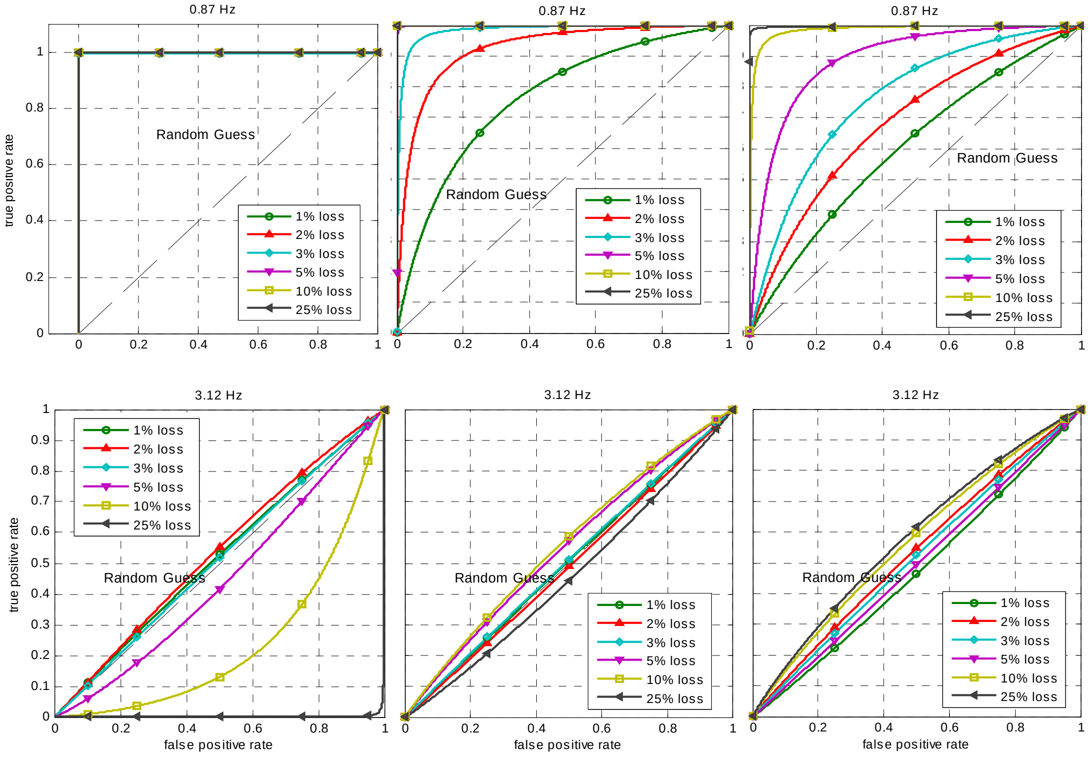

Figure 5-18: ROC curves for different frequencies and settings with n_d=4, upper left: 0.87Hz, external noise free; upper mid: 0.87Hz, 1% *NSR*; upper right: 0.87Hz, 10% *NSR*; lower left: 3.12Hz, external noise free; lower mid: 3.12Hz, 1% *NSR*; lower right: 3.12Hz, 10% *NSR*

By computing how much deviation a particular ROC curve has from the random guess line, there is a reasonable metric for quantifying how good a particular frequency line is as a candidate detector. This metric is defined by calculating the area-under-the curve (*AUC*) as the planar area between the ROC measurement and random guess line. As shown in Figure 5-19, the metric has a range from 0 to 0.5, and when the *AUC* is closer to 0.5, the detection is closer to optimal.

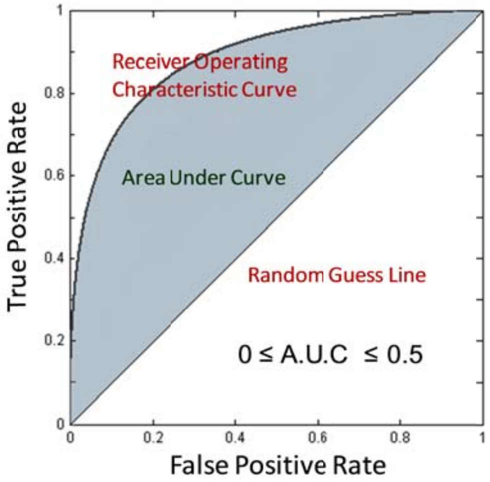

Figure 5-19: definition of Area Under Curve (*AUC*)

The *AUC* metric is evaluated for all the damage levels under the situations with different noise levels, and the results are plotted in Figure 5-20. The same conclusions may be drawn with more details. Severe damage will have greater separation and thus better detectability. For the noise-free case, it is clear that in the frequency region with large input-output gain, the transmissibility estimation will be very sensitive to the structural parameter change; in the frequency region with low gains, there is no clear data separation, even when the damaged stiffness is 25% lower than its original value.

As the level of extraneous noise goes higher, shown in middle and right plots in Figure 5-20, the *AUC* evaluations, as expected, drop dramatically at all frequencies. But at the frequencies where large input-output gain is available, there will be better detection performance, but the range of frequencies to choose is becoming narrower as *NSR* goes high, and shrinking to the area near resonances. This indicates that it is the easiest to implement binary classification of transmissibility estimations near resonant frequencies.

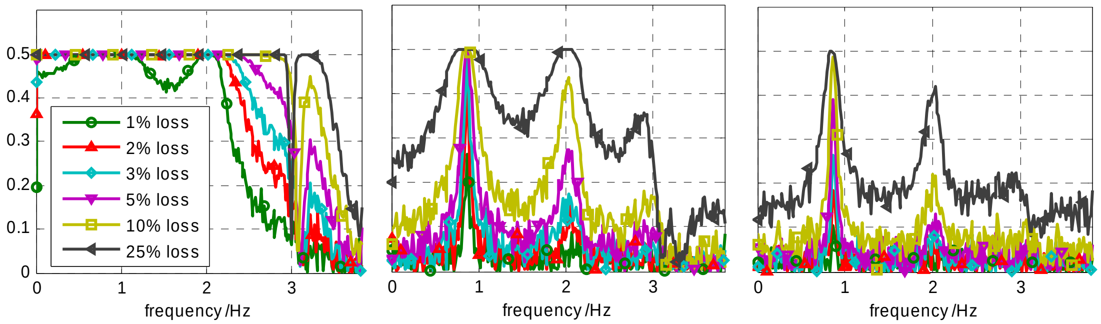

Figure 5-20: *AUC* metric evaluation v.s. frequency, left: external noise free; middle: 1% of *NSR* right: 10% of *NSR*

Figure 5-21 highlights the *AUC* metric evaluation at two previously-mentioned sample frequency lines, i.e. 0.87Hz and 3.12Hz, referring to frequencies with large and small input-output gains. As damage becomes severe, the detectability is better, and for big enough damage, the *AUC* value is still good for noise-contaminated conditions and small-gain frequency lines.

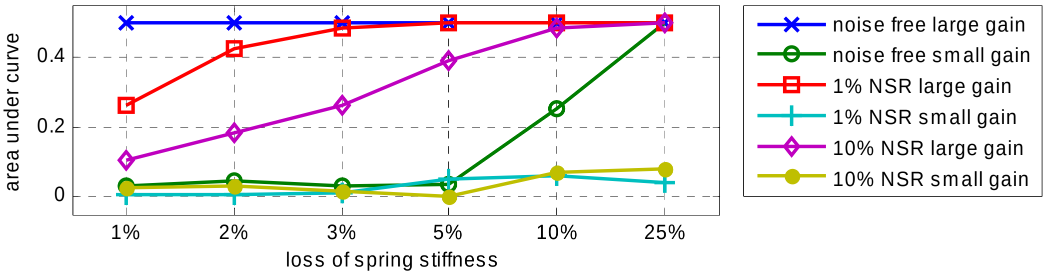

Figure 5-21: Comparison of *AUC* for different damage levels and noise-to-signal levels

Different from the ideal 3-DOF theoretical model, a quick baseline-damage-separation is also studied on the lab-scale plate structure presented in 5.1.2. Different estimations quantified by three UQ models are compared. Figure 5-22 shows the visualization of each model for damaged/undamaged structure at an arbitrary frequency line, with both noise-free and 1% *NSR* noise-contaminated data. Perturbation approach only gives standard deviation (without underlying PDFs), but histogram of measurements are plotted in Figure 5-22 (a, d) with asterisks highlighting ±1σ uncertainty bounds. For each model, there is overlap between the two distributions, although it may appear that the chi-square model performs the best purely based on visual observation. Thus quantitatively, ROC curves for the two approaches supplying analytical PDFs are plotted in Figure 5-23. The two curves with noise contamination are much closer to the random guess line (45-degree line) than the two noise-free ROC curves, as would be expected. Comparing the results between the models, it is clear to see that Chi-square results are furthest from the random guess line and have the best *AUC*, which means for a certain number of false alarms there will be more true detections. Therefore, despite from the conclusion made in 5.1.2 for entire frequency domain that Gaussian bivariate approach gives the most stable detection, there is a slightly more sensitive and specific detection at single frequency line through Chi-square bivariate distribution modeling. Thus in real applications, selection of estimators and UQ models should consider a variety of factors, such as the signal to noise quality, availability of input data, and also the specific SHM features involving only single frequency lines or the entire frequency domain.

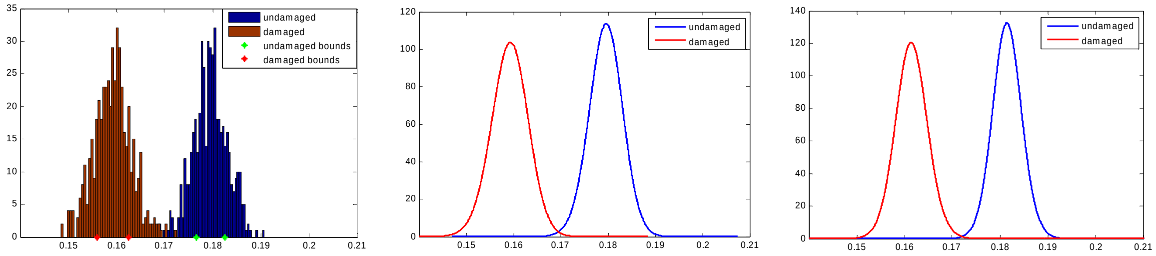

(a) Histogram and 1-σ bounds of perturbation model, noise free

(b) PDF of Gaussian bivariate model, noise free

(c) PDF of Chi-square bivariate model, noise free

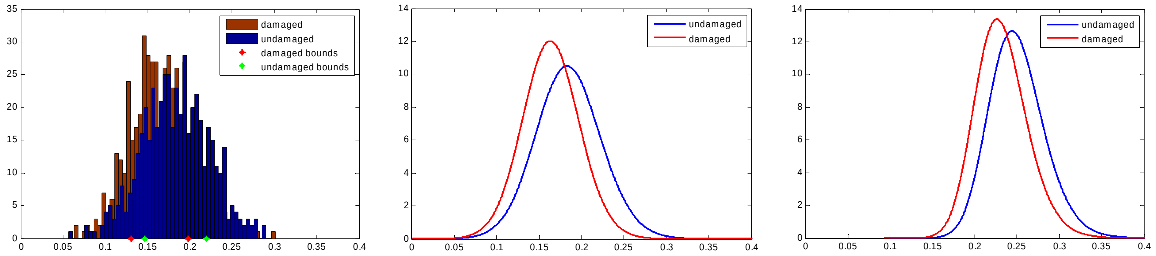

(d) Histogram and 1-σ bounds of perturbation model, contaminated

(e) PDF of Gaussian bivariate model, noise contaminated

(f) PDF of Chi-square bivariate model, noise contaminated

Figure 5-22: statistical model visualization for transmissibility estimation at an arbitrary frequency

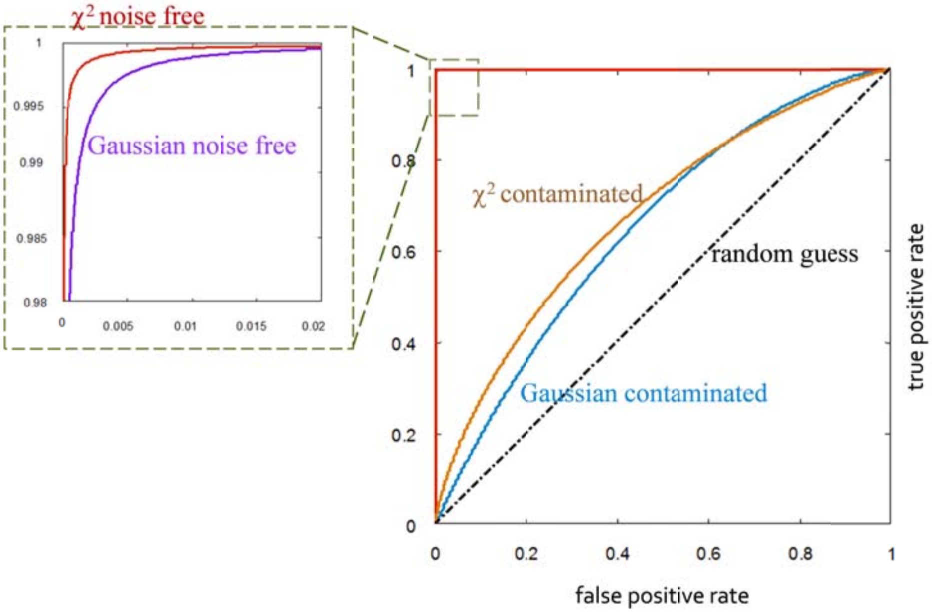

Figure 5-23: Receiver operating characteristics (ROC) for Gaussian bivariate detection and Chi-square bivariate detection

5.3 Optimal statistical hypothesis test

In section 5.2, separation of two distributions is studied, with *AUC* metric evaluating the receiver operating characteristics. Some of the hypothesis test ideas have been mentioned without detail discussion, and in this section, statistical significance detection will be discussed from the hypothesis test point of view.

5.3.1. Introduction of hypothesis test

Statistical hypothesis test is well founded by Neyman and Pearson [96], and it turns decision making problems into acceptance or rejection of given statistical hypotheses under certain confidence. Following Neyman-Person theorem, the damage detection is to choose among two mutually exclusive hypotheses, namely null hypothesis and alternative hypothesis:

$$\begin{aligned} \mathcal{H}_0 &: z \sim \Phi\left(\mathbf{\Lambda}_u\right) \\ \mathcal{H}_1 &: z \sim \Phi\left(\mathbf{\Lambda}_d\right) \end{aligned}, \tag{5-5}$$

where z is the feature measurement and Φ is PDF of z, with undamaged parameter set Λ_u or damaged parameter set Λ_d. To maximize probability of detection P_D for any given significance α, i.e. given probability of false alarms P_FA, decide $\mathcal{H}_1$ if the likelihood ratio:

$$L(z) = \frac{\Phi\left(z;\mathcal{H}_1\right)}{\Phi\left(z;\mathcal{H}_0\right)} > \gamma, \tag{5-6}$$

where the threshold γ is associated with α by:

$$\alpha = \mathrm{P}_\mathrm{FA} = \int_{\{z:L(z)>\gamma\}} \Phi\left(z;\mathcal{H}_0\right) dz, \tag{5-7}$$

and the corresponding optimal probability of detection is therefore:

$$\mathrm{P}_D = \Phi\left(\mathcal{H}_1;\mathcal{H}_1\right) = \int_{\{z:L(z)>\gamma\}} \Phi\left(z;\mathcal{H}_1\right) dz. \tag{5-8}$$

From the hypothesis point of view, the two types of errors mentioned in last section, namely false positive and false negative, can be expressed as: Type I error is the false alarm when a true null hypothesis is rejected, and type II error is the cases that false null hypothesis fails to be rejected [96].

In the hypothesis tests to be shown in this section, the statistical significance detection problems are classified into four cases, shown in Figure 5-24.

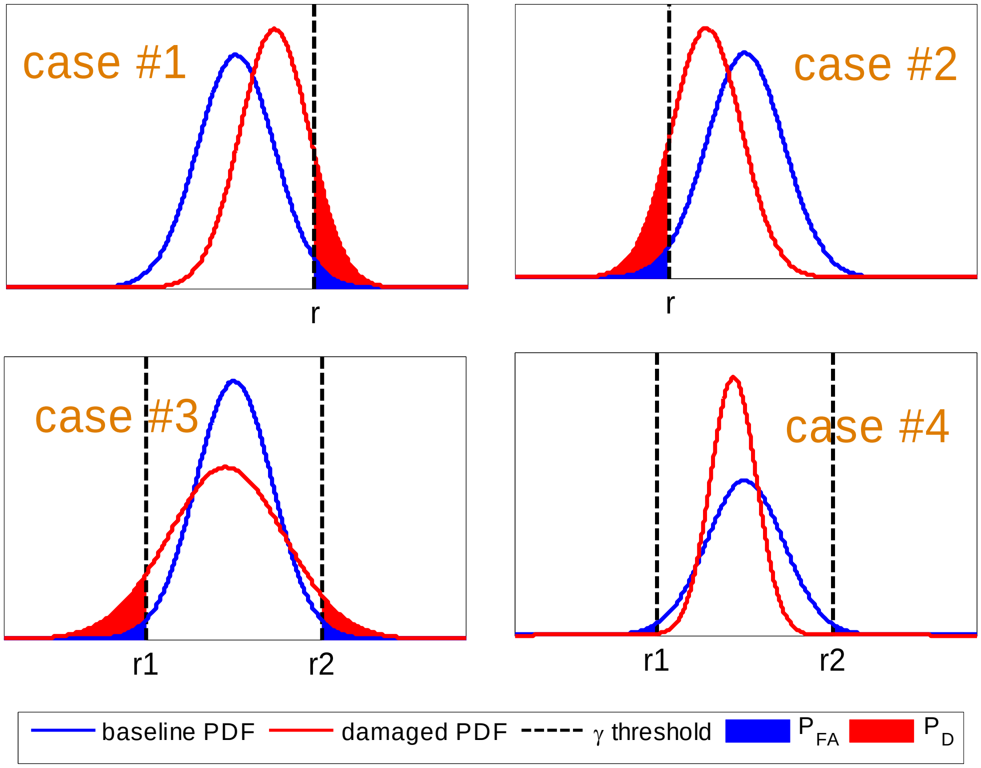

Figure 5-24: hypotheses for different conditions

For the first two cases, the damaged distribution differs from baseline primarily as mean shift without distinct change of variation, so that the region of rejection only needs to be on one side of the distribution domain. Case #1 and#2 represent respectively the increasing and decreasing mean shift of damaged distribution. Different from the single tail test, Case #3 and #4 show more obvious changes in variation than mean, so both tails should be considered as critical region. In particular, the detectors regarding four cases in Figure 5-24 can be expressed explicitly as Equation (5-9):

$$\text{Case \#1,}\ \begin{array}{l}\mathcal{H}_0 : z \le \gamma \\ \mathcal{H}_1 : z > \gamma\end{array}; \qquad \text{Case \#2,}\ \begin{array}{l}\mathcal{H}_0 : z \ge \gamma \\ \mathcal{H}_1 : z < \gamma\end{array};$$

$$\text{Case \#3 and \#4,}\ \begin{array}{l}\mathcal{H}_0 : \gamma_1 \le z \le \gamma_2 \\ \mathcal{H}_1 : z < \gamma_1 \cup z > \gamma_2\end{array}, \tag{5-9}$$

in which γ is obtained via Equation (5-7) associated with significance level α, while γ_1 and γ_2 in the double tailed hypothesis test are associated to $\alpha/2$ and $1-\alpha/2$ percentile on each side.

5.3.2. Example of hypothesis test

In this part, the proposed hypothesis test in Equation (5-9) is implemented based upon the baseline and damaged transmissibility/FRF, both their magnitude and phase obtained from beam and plate structure introduced in section 4.2 and 4.3. Probability of detection P_D will be presented for different test conditions with various P_{FA} thresholds, and at each frequency line, P_D is color-coded indicating which case the detection problem at this frequency is. Legend of the color-coded P_D is illustrated in Figure 5-25.

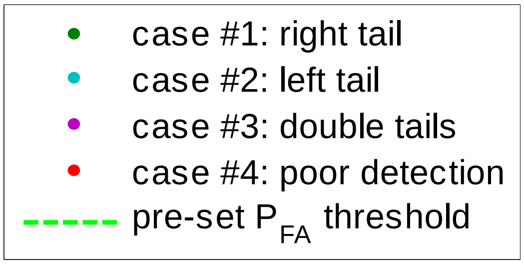

Figure 5-25: legend of PD of different cases

The null/alternative hypotheses in Equation (5-9) for the two double-tail tests are identical, but Case #3 and #4 are still differentiated, because Case #4 will have a poor P_D which is always less than P_{FA}, no matter how the hypothesis is designed. Therefore it is group classified as poor detection condition.

Firstly consider the hypothesis test with beam damage detection, in which the vibration test has been characterized in Figure 4-2. Figure 5-26 plots the expectation of FRF (H and H_d) and transmissibility (T and T_d) for both magnitude and phase. Two pre-set P_{FA} tolerance levels are selected and detection problems with different noise contamination conditions are also considered, in which 0, 1% and 10% NSR are shown from Figure 5-27 to 5-30.

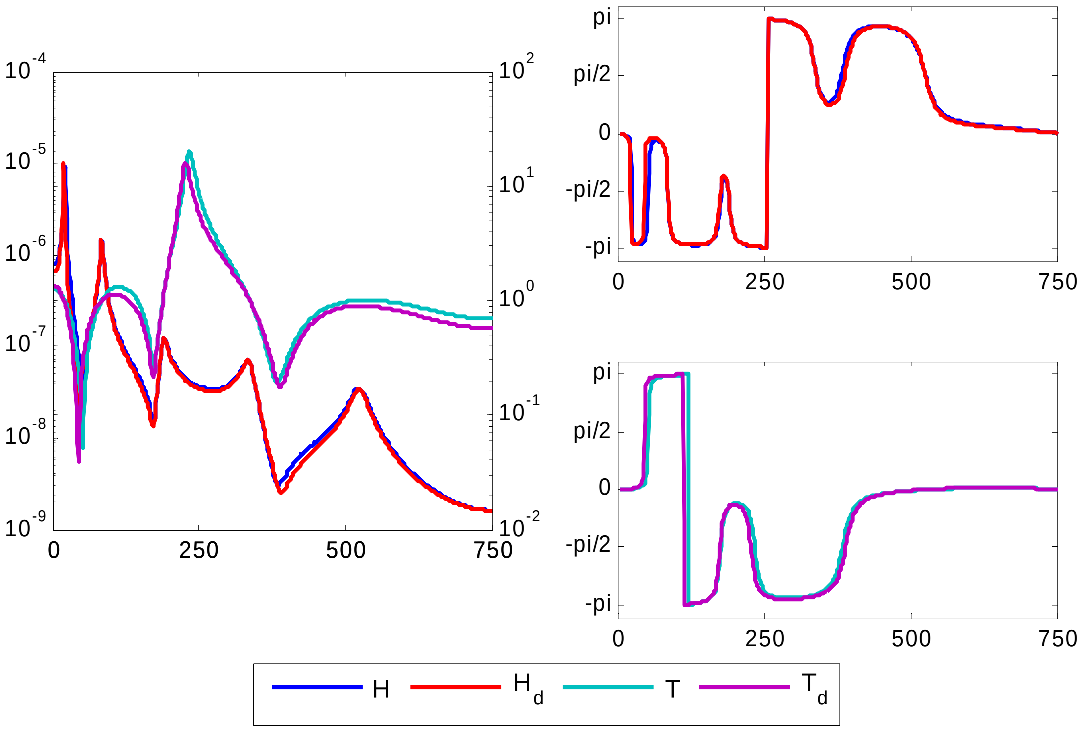

Figure 5-26: magnitude (left) and phase (right) of transfer functions of beam structure, baseline and damaged conditions.

Comparing Figures 5-27 and 5-28, there is mostly near 100% detection for noise free condition, with both P_{FA} thresholds. For contaminated cases, transmissibility outperforms FRF slightly, but both detectors perform only well at low frequency region, which matches to the bandwidth with high input-output gain addressed in Figure 5-26(left), therefore good local $SNR(\omega)$. In high frequency area, because of the fairly poor estimation quality, according to Figure 4-11, the detection of statistical significance is very hard. Figures 5-29 and 5-30 illustrate the same observations on phase detection, and in these figures, there are obviously more presence of Case #3 for both transmissibility and FRF than what is seen in magnitude results, which means for phase estimation, damaged data often appear increasing of variance. Moreover, for this specific test and damage setting, magnitude detector has better P_D than phase detector.

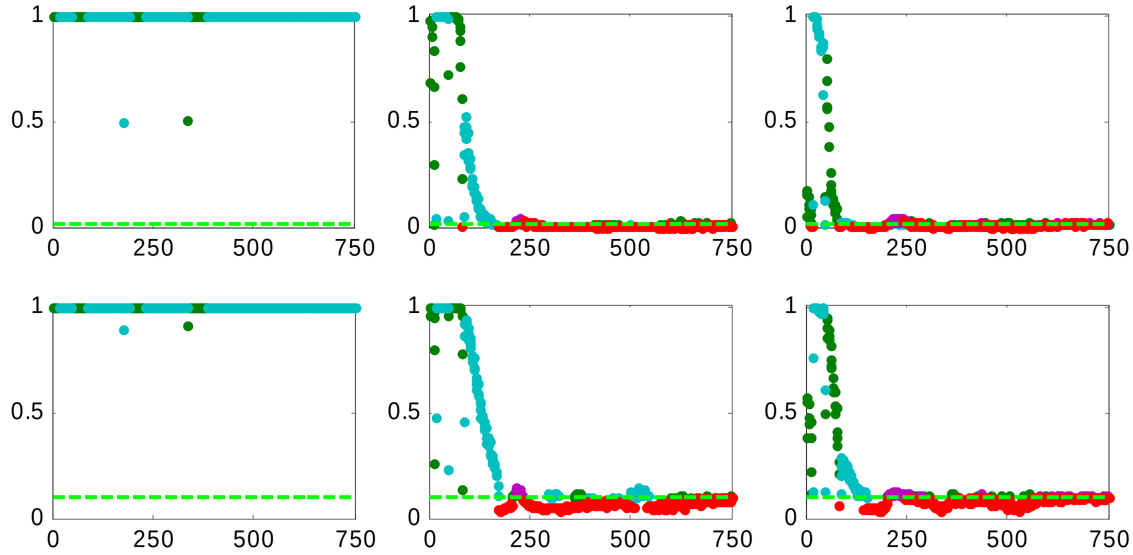

Figure 5-27: P_D of beam structure T magnitude with 1% (upper row) and 10% (lower row) of pre-set P_{FA} threshold. Left to right columns: 0, 1% and 10% *NSR* contamination.

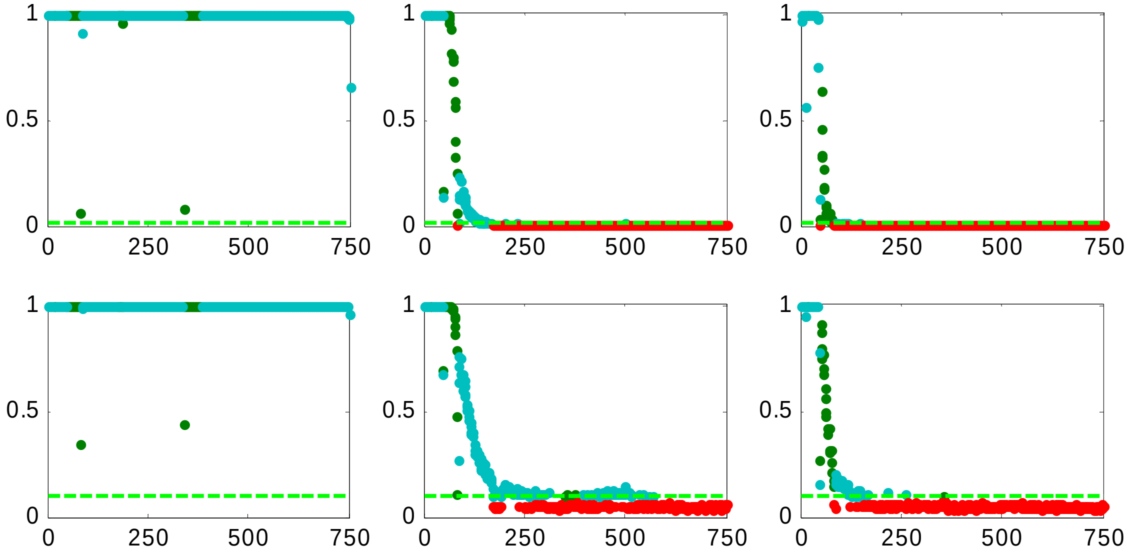

Figure 5-28: P_D of <u>beam</u> structure <u>H</u> <u>magnitude</u> with 1% (upper row) and 10% (lower row) of pre-set P_{FA} threshold. Left to right columns: 0, 1% and 10% *NSR* contamination.

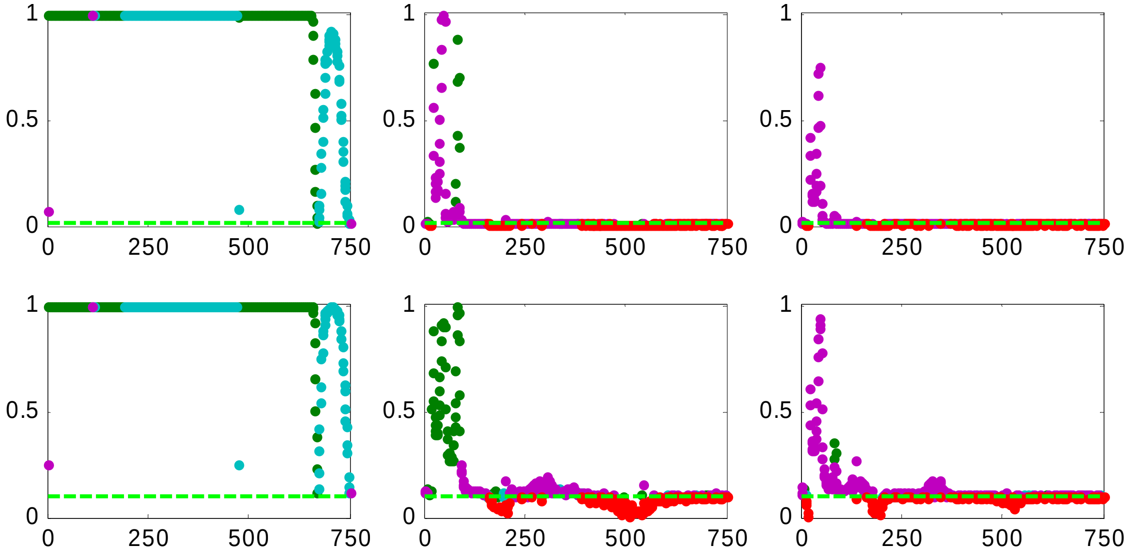

Figure 5-29: P_D of <u>beam</u> structure <u>T</u> <u>phase</u> with 1% (upper row) and 10% (lower row) of pre-set P_{FA} threshold. Left to right columns: 0, 1% and 10% *NSR* contamination.

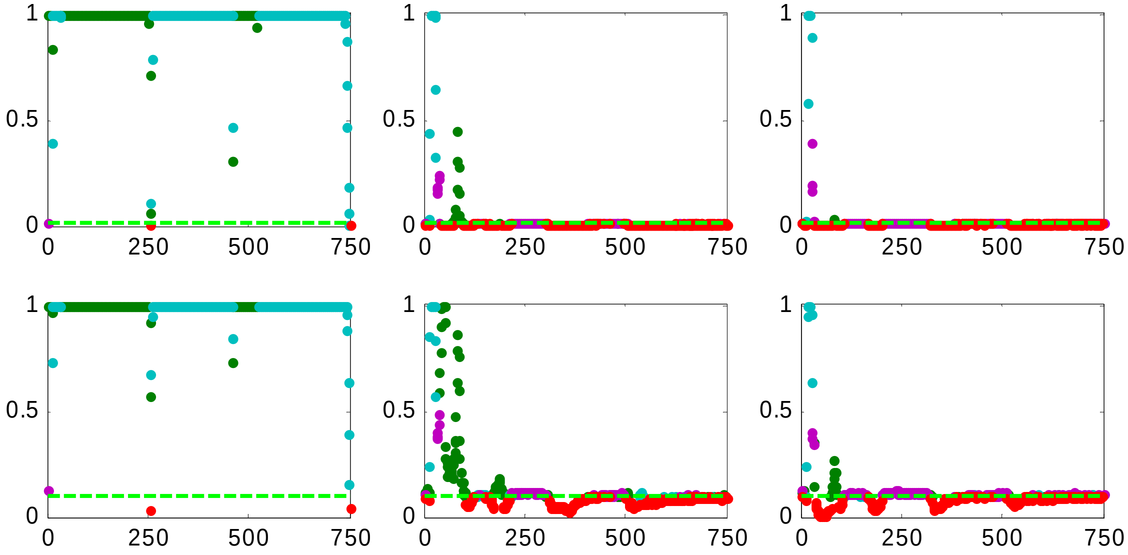

Figure 5-30: P$_D$ of <u>beam</u> structure <u>H</u> <u>phase</u> with 1% (upper row) and 10% (lower row) of pre-set P$_{FA}$ threshold. Left to right columns: 0, 1% and 10% *NSR* contamination.

Then consider hypothesis test with plate structural assessment, which has been characterized in Figure 4-18. Similar to aforementioned beam structure, Figure 5-31 plots the transfer functions with respect to their magnitude and phase, with subscript $_d$ denoting the damaged situation.

Tolerance of 1% and 10% of P$_{FA}$ is preset, with the same noise contamination configuration. Figures 5-32 to 5-35 plot the optimal P$_D$ for each detector with the same color convention.

Again, this lab scaled test does not provide as clean data as simulation supplies, so for the external noise free condition, there is generally good detection quality, but not as good as the hypothesis test for beam simulation. For this structure, magnitude and phase of FRF have better detection robustness suffering to noise, while the P_D of magnitude and phase for transmissibility is overall poor for those contaminated cases. Similar to beam structure, there is more appearance of Case #3 for phase detection than magnitude.

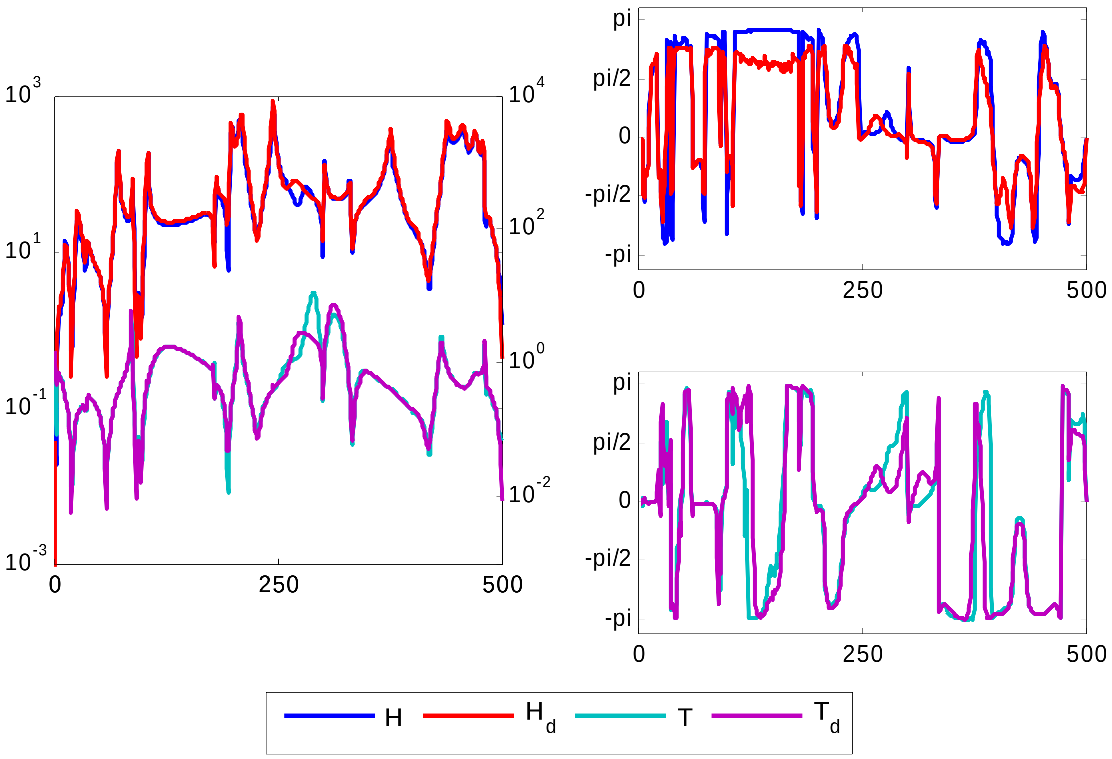

Figure 5-31: magnitude (left) and phase (right) of transfer functions of plate structure, baseline and damaged conditions.

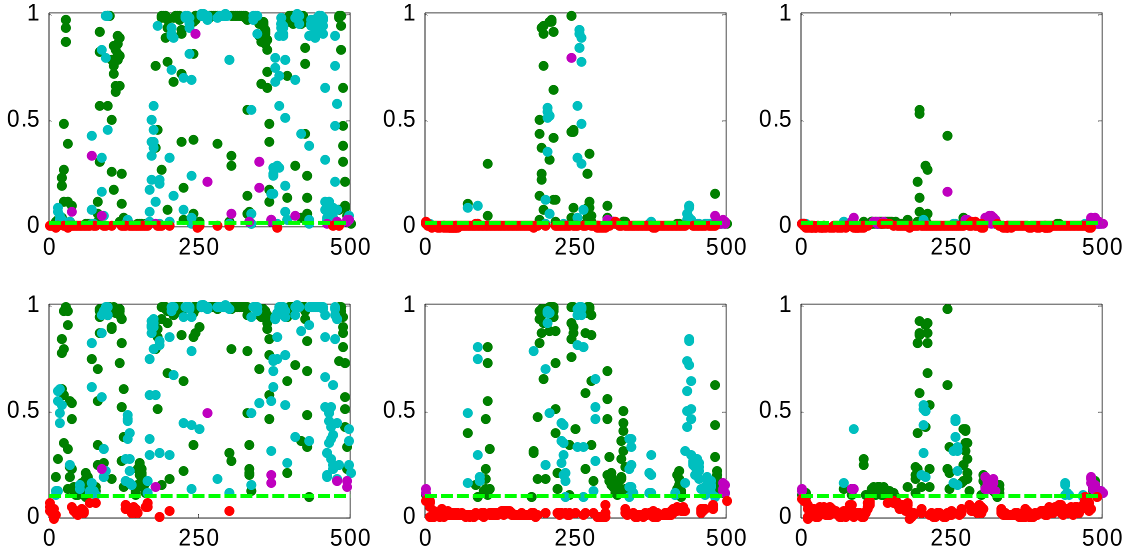

Figure 5-32: P_D of plate structure T magnitude with 1% (upper row) and 10% (lower row) of pre-set P_{FA} threshold. Left to right columns: original data, 1% and 10% *NSR* artificial noise contamination.

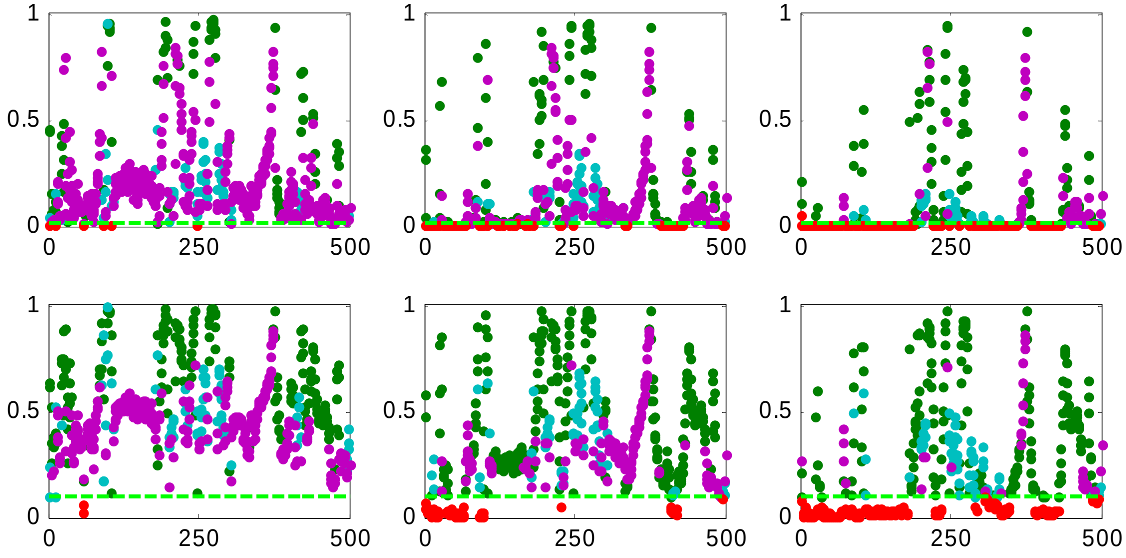

Figure 5-33: P_D of plate structure H magnitude with 1% (upper row) and 10% (lower row) of pre-set P_{FA} threshold. Left to right columns: original data, 1% and 10% *NSR* artificial noise contamination.

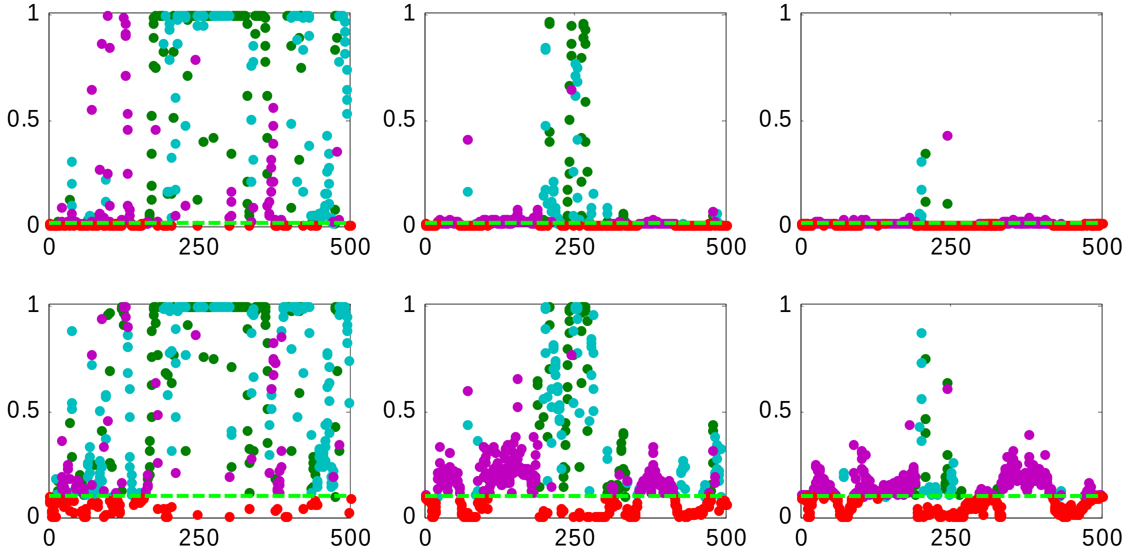

Figure 5-34: P_D of plate structure T phase with 1% (upper row) and 10%(lower row) of pre-set P_{FA} threshold. Left to right columns: original data, 1% and 10% *NSR* artificial noise contamination.

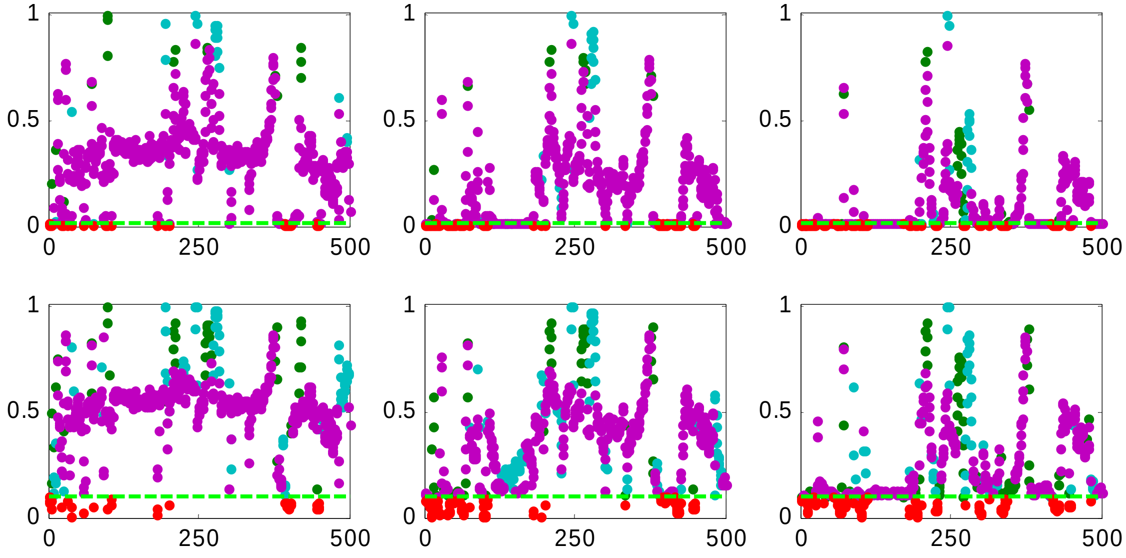

Figure 5-35: P_D of plate structure H phase with 1% (upper row) and 10%(lower row) of pre-set P_{FA} threshold. Left to right columns: original data, 1% and 10% *NSR* artificial noise contamination.

5.3.3. Summary

In this section, hypothesis testing for damage detection in both beam and plate structures have been investigated, using both transmissibility and FRF, both magnitude and phase. Consistent conclusions can be made, referring to ROC analysis in section 5.2: external noise degrades the detectability and for the frequency lines with good local $SNR(\omega)$, P_D is always good no matter transmissibility or FRF, magnitude or phase. For different conditions, there are some detection cases with less sensitivity and even very poor performance. Figure5-36 specifically illustrates good detection in Case #3 and poor detection problem of Case #4. Cumulative probability density (CDF) are plotted on the right column, from which there is a weak difference in the lower right plot corresponding to a tiny Kolmogorov–Smirnov distance, and the upper right CDF with big distance thus more confidence to reject null hypothesis.

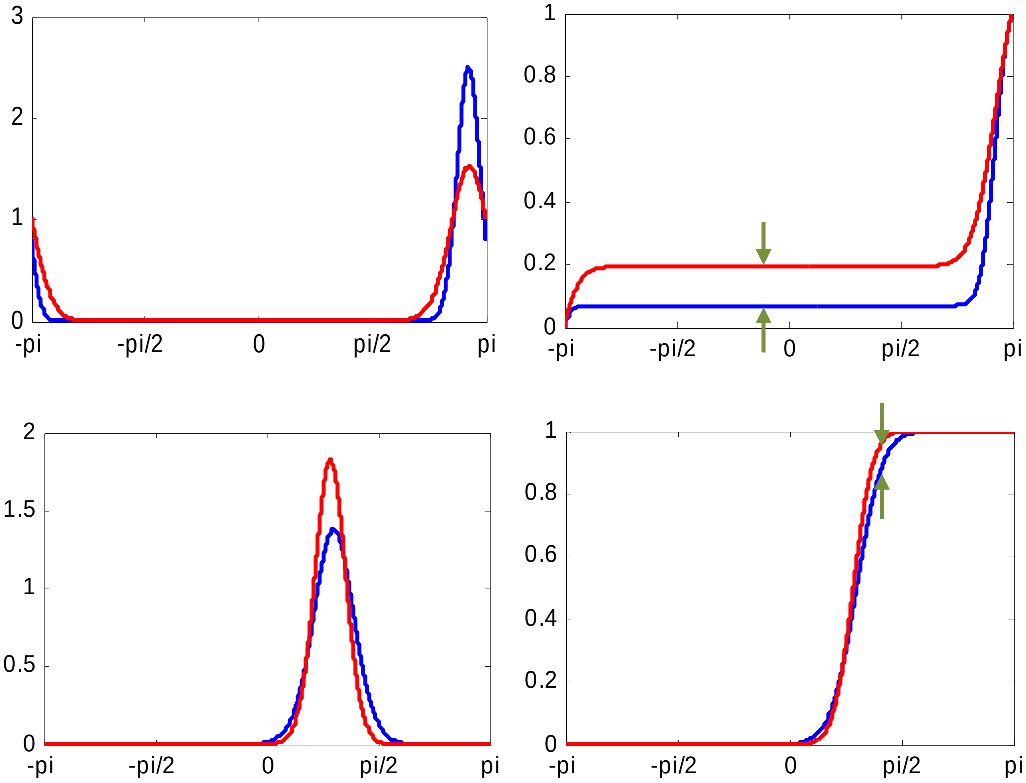

Figure 5-36: example distributions for baseline and damaged phase statistics. Left: PDF; right: CDF; upper row: good separation (Case #3); lower row: poor separation (Case #4)

This chapter, in part, has been published in *Proc. SPIE 7984*, Zhu Mao and Michael Todd, 2011. The title of this paper is "Statistical quantification of the uncertainty in transmissibility feature for structural condition binary classification". The dissertation author was the primary investigator and author of this paper. A portion of this chapter has been published in *Proceedings of the 8th International Workshop on Structural Health Monitoring*, Zhu Mao and Michael Todd, 2011. The title of this paper is "Uncertainty Quantification in Transmissibility-Derived Features Used for Fault Detection". The dissertation author was the primary investigator and author of this paper. A portion of this chapter has been published in *Proceedings of IMAC, Society for Experimental Mechanics Series, Volume 29*, Zhu Mao and Michael Todd, 2012. The title of this paper is “Rapid Structural Condition Assessment Using Transmissibilities with Quantified Confidence for Decision Making”. The dissertation author was the primary investigator and author of this paper. A portion of this chapter has been submitted for publication in *The Proceedings of the ASME 2012 Conference on Smart Materials, Adaptive Structures and Intelligent Systems, SMASIS 2012-7935*, Zhu Mao and Michael Todd, 2012. The title of this paper is “The quantification of uncertainty in SHM features derived from frequency response estimation”. The dissertation author was the primary investigator and author of this paper.

6. Conclusions and Future Research

Due to the intensive time consumption of current maintenance and operation costs in structural status evaluation, more and more research has been done towards a fast damage identification and real-time structural health monitoring (SHM), by which the time/economic cost could be dramatically reduced. Motivated by the structural rapid state awareness demanding, this dissertation adopts vibration-based inspections and deploys statistical significance detection in order to identify the possible structural defects.

6.1. Conclusions

Power spectral measurements are of the most useful category for structural health monitoring, because of the clear physical interpretation and easy-accessibility through fast Fourier Transform. For various SHM applications, optimal features are always anticipated to characterize structural status, and those features are selected to be sensitively and specifically indicating structural parameter change and therefore the type I and type II error can be both minimized as possible. This dissertation quantifies the uncertainty existed in power spectral SHM features and enhances decision-making capabilities in damage identification.

Firstly, this dissertation proposes two transmissibility-based features for a rapid structural state awareness, specifically fastener loosening identification. A contrived cubical finite element (FE) model is established through which transmissibilities with different excitations are extracted. Paradigmatic damages are applied onto FE model illustrating a good detection capability via change of transmissibilities.

For realistic SHM strategies, random excitation is often applied for stationary baseline training, and in this situation, multiple algorithms of transmissibility and frequency response function (FRF) evaluations are compared, with respect to their accuracy and compatibility of test conditions. These estimators are unavoidably subject to noise and uncertainties from different sources, and estimation of features will be a random variable falling into certain distribution. This makes the optimal feature selection more demanding, because under this circumstance, some of the feature estimations are highly overlapped between baseline and damaged data sets, and a trade-off between sensitivity and specificity is consequently inevitable. Statistical models for different features by different estimators are presented in this dissertation, so as to quantify the uncertainty and significance in feature estimations, and all the uncertainty quantification (UQ) models are validated through Monte-Carlo testing with data obtained from both simulation and real laboratory experimental data. Outlier-based metrics, outlier percentage and root-mean-square error, are proposed to quantitatively assess the accuracy of UQ models. To validate UQ models in a more stringent condition, artificial noise is added to contaminate feature estimations, and very good consistency between the prediction and Monte-Carlo results is also observed, revealing the robustness of proposed models.

Probability density functions of FRF/transmissibility estimations are derived in this dissertation, for both magnitude and phase. With uncertainty fully characterized by means of the proposed UQ models, statistical significance detection techniques are implemented, which in the context of SHM, is used in hypothesis testing for damage detection. In each of the feature evaluations, the performance comparison is proceeded under the condition of best trade-off between sensitivity and specificity, adopting receiver operating characteristics (ROC). Consequently, with the significance level provided by the statistical models established, there is a quantitative understanding of the estimations and quantified confidence for decision-making that relies on the estimations. Suggestion of good detection quality is given after comparing different estimators and noise contaminated condition, with respect to area under curve (AUC) of ROC.

Finally, research of probability of detection is studied by varying the level of false alarm tolerance, and detection problems are classified into four categories regarding mean-shift and variation-change dominated types. Detection qualities through different features are classified and compared.

6.2. Future research

Relevant future work in this area will include further investigation of detectors, especially for damage localization detectors. Propagation of predicted transmissibility/FRF uncertainties to other features selected for various specific applications will be studied. Tailored algorithms will be considered in the fields of online structural health monitoring with certainty requirements according to the applications. Probabilistic damage prognosis research is anticipated to be carried out via a Bayesian model selection/updating process, where decision boundaries on user end are optimized and performance metrics such as “probability of detection” are of prime importance.

References

[1] Charles Farrar, Keith Worden, An introduction to structural health monitoring, Phil. Trans. R. Soc. A (2007) 365, 303–315

[2] Keith Worden, Charles Farrar, Graeme Manson, Gyuhae Park, The fundamental axioms of structural health monitoring, Proc. R. Soc. A (2007) 463, 1639–1664

[3] Doebling, S. W., Farrar, C. R., Prime, M. B., Shevitz D. W., Damage identification and health monitoring of structural and mechanical systems from changes in their vibration characteristics: a literature review. Los Alamos National Laboratory report LA-13070-MS, 1996

[4] Hoon Sohn, Charles R. Farrar, Francois M. Hemez, Devin D. Shunk, Daniel W. Stinemates, and Brett R. Nadler, A Review of Structural Health Monitoring Literature 1996-2001, Los Alamos National Laboratory Report, LA-13976-MS, 2003

[5] Randall, B. R., State of the art in monitoring rotating machinery-part 1, Sound Vibrat. 38, 14–21, 2004

[6] Randall, B. R., State of the art in monitoring rotating machinery-part 2. Sound Vibrat. 38, 10–17, 2004

[7] Michael I Friswell, Damage identification using inverse methods, Phil. Trans. R. Soc. A, 15-vol. 365, 2007

[8] C. R. Farrar and N. Lieven "Damage Prognosis: The Future of Structural Health Monitoring," Philosophical Transactions of the Royal Society A, 365, February, 2007, pp.623-632.

[9] Peter C. Chang, Alison Flatau, and S. C. Liu Review Paper: Health Monitoring of Civil Infrastructure, Structural Health Monitoring, September 2003 2: 257-267,

[10] Jinping Ou and Hui Li, Structural Health Monitoring in mainland China: Review and Future Trends, Structural Health Monitoring, May 2010 9: 219-231

[11] Andrew D. Dimarogonas, Vibration of cracked structures: A state of the art review, Engineering Fracture Mechanics Volume 55, Issue 5, November 1996, Pages 831–857

[12] Wei-Xin Ren and Guido De Roeck, Structural Damage Identification using Modal Data.I: Simulation Verification, Journal of Structural Engineering, Vol. 128, No. 1, January 2002, pp. 87-95

[13] Z.Q. Lang, Z.K. Peng, A novel approach for nonlinearity detection in vibrating systems, Journal of Sound and Vibration 314 (2008) 603–615

[14] Z.K. Peng, Z.Q. Lang, F.L. Chu, Numerical analysis of cracked beams using nonlinear output frequency response functions, Computers and Structures 86 (2008) 1809–1818

[15] K. Worden, G. Manson, N.R.J. Fieller, Worden K, Manson G, Fieller NRJ, Damage detection using outlier analysis, Journal of Sound and Vibration, 229(3)(2000) 647-667.

[16] T.J. Johnson, D.E. Adams, Transmissibility as a differential indicator of structural damage, Transactions of the ASME: Journal of Vibration and Acoustics, 124(2002) 634-641.

[17] M. Modares and J. Mohammadi, Asset Management of Structures Using Hybrid Structural Health Monitoring and Structural Uncertainty Analysis Procedure Proceedings of the ICVRAM 2011 and ISUMA 2011 Conferences

[18] Ajoy Kumar Das and Achintya Haldar, Structural Health Assessment using only Noise-Contaminated Responses, Proceedings of the ICVRAM 2011 and ISUMA 2011 Conferences, 2011 Hyattsville, MD

[19] S Kabashima, T. Ozaki, N. Takeda, Damage detection of satellite structures by optical fiber with small diameter, Proceedings of SPIE Vol. 3985 (2000)

[20] Seth Stovack Kessler, Piezoelectric-Based In-Situ Damage Detection of Composite Materials for Structural Health Monitoring Systems, DOCTORATE OF PHILOSOPHY thesis, Department of Aeronautics and Astronautics, MASSACHUSETTS INSTITUTE OF TECHNOLOGY, 2002

[21] E. H. Clayton, Y. Qian, O. Orjih, S. J. Dyke, A. Mita, C. Lu, “Off-the-Shelf Modal Analysis: Structural Health Monitoring with Motes,” In proceedings of the 24th International Modal Analysis Conference (IMAC-XXIV), St. Louis, MO, January 29 – February 2, 2006

[22] Timothy J. Johnson, Rebecca L. Brown, Douglas E. Adams, Mark Schiefer, Distributed structural health monitoring with a smart sensor array, Mechanical Systems and Signal Processing, Volume 18, Issue 3, May 2004, Pages 555-572

[23] E. H. Clayton, S. J. Dyke, and C. Lu, MONITORING INFRASTRUCTURAL HEALTH: IN-SITU DAMAGE DETECTION AND LOCALIZATION UTILIZING DISTRIBUTED SMART SENSOR TECHNOLOGY 4th World Conference on Structural Control and Monitoring

[24] Lynch, J. P. and Loh, K. J., A Summary Review of Wireless Sensors and Sensor Networks for Structural Health Monitoring, Shock and Vibration Digest, Sage Publications, 38(2): 91-128, 2006

[25] Michael D. Todd and Eric B. Flynn, A Bayesian Experimental Design Approach for Structural Health Monitoring, Proceedings of the XIV International Symposium on Dynamic Problems of

Mechanics (DINAME 2011), Brazil, 2011

[26] L. Ljung, Perspectives on System Identification, Annual Reviews in Control Volume 34, Issue 1, pp.1-12, 2010

[27] L. Ljung, Aspects on the system identification problem, Signal Processing, 4(1982) 445-456.

[28] R. Brincker, L. Zhang, P. Andersen, Modal identification of output-only systems using frequency domain decomposition, Smart Materials and Structures, 10(2001) 441-445.

[29] Jonas Sjöberg, Qinghua Zhang, Lennart Ljung, Albert Benveniste, Bernard Delyon, Pierre-Yves Glorennec, Håkan Hjalmarsson and Anatoli Juditsky, Nonlinear black-box modeling in system identification: a unified overview, Automatica, Vol 31(12), 1995, Pages 1691–1724

[30] Bart Peeters and Guido De Roeck, Stochastic System Identification for Operational Modal Analysis: A Review, J. Dyn. Sys., Meas., Control, 123, 659 (2001)

[31] S.W. Doebling, C.R. Farrar, M.B. Prime, A summary review of vibration-based damage identification methods, The Shock and Vibration Digest, 30(2) (1998) 91-105.

[32] Cawley, P. 'Defect location in structures by vibration technique', PhD thesis, Mechanical Engineering Department, Bristol University, 1978

[33] Wei Fan and Pizhong Qiao, Vibration-based damage Identification Methods: A Review and Comparative Study, Structural Health Monitoring first published on April 20, 2010

[34] Brandon J. Arritt , Steven J. Buckley, Jeffrey M. Ganley, Jeffry S. Welsh, Benjamin K. Henderson, M. Eric. Lyall, Andrew D. Williams, Jeffrey C. Prebble, John DiPalma, Greg Mehle, Roopnarine, Development of a Satellite Structural Architecture for Operationally Responsive Space, Proc. of SPIE Vol. 6930, 69300I, (2008)

[35] Irene Yachbes, Roopnarine, Shazad Sadick, Brandon Arritt, Rapid Assembly of Spacecraft Structures for Operationally Responsive Space, AIAA/6th Responsive Space Conference 2008, Los Angeles, CA

[36] Derek Doyle, Andrei Zagrai, Brandon Arritt, and Hakan Çakan, Damage Detection in Bolted Space Structures, Journal of Intelligent Material Systems and Structures February 2010 21: 251-264

[37] Brandon J. Arritt, Amrita Kumar, Steven Buckley, Robert Hannum, Jeffry Welsh, Shawn Beard, Xinlin Qin and Peter Wegner, "Responsive satellites and the need for structural health monitoring", Proc. SPIE 6531, 653109 (2007)

[38] Arritt, B.J., Robertson, L.M., Williams, A.D., Henderson, B.K., Buckley, S.J., Ganley, J.M., Welsh, J.S., Ouyang, L., Beard, S., Clayton E. H., Todd, M.D., Doyle D., Zagrai, A., "Structural

Health Monitoring; an Enabler for Responsive Satellites," Proceeding of the 49th Structures, Structural Dynamics, and Materials Conference (SDM), Schaumburg, Illinois, April 7-10, 2008.

[39] Active ultrasonic joint integrity adjudication for real-time structural health monitoring, Clayton, Erik H.; Kennel, Matthew B.; Fasel, Timothy R.; Todd, Michael D.; Stabb, Mark C.; Arritt, Brandon J. Proceedings of the SPIE, Volume 6935, pp. 69350M-69350M-11 (2008).

[40] Fasel, T.R., Todd, M.D., Clayton, E.H., Stabb, M.D., Park, G. "Bolted Joint Damage Assessment using Chaotic Probes," Proceedings of IMAC-XXVI, A Conference & Exposition on Structural Dynamics,February 4- 7 2008, Orlando, FL

[41] C. Devriendt, G. Steenackers, G. De Sitter, P. Guillaume, From operating deflection shapes towards mode shapes using transmissibility measurements, Mechanical Systems and Signal Processing, 24(2010) 665-677.

[42] C. Devriendt, P. Guillaume, Identification of modal parameters from transmissibility measurements, Journal of Sound and Vibration, 314(2008) 343–356.

[43] A.M.R. Ribeiro, J.M.M. Silva, N.M.M. Maia, On the generalisation of the transmissibility concept, Mechanical systems and Signal Processing, 14(2000) 29-35.

[44] J.E. Mottershead, On the zeros of structural frequency response functions and their sensitivities, Mechanical Systems and Signal Processing, 12(1998) 591-597.

[45] J. He, Y.-Q. Li, Relocation of anti-resonance of a vibratory system by local structural changes, Modal Analysis: the International Journal of Analytical and Experimental Modal Analysis, 10(1995) 224-235.

[46] C. Devriendt, P. Guillaume, The use of transmissibility measurements in output-only modal analysis, Mechanical systems and Signal Processing, 21 (2007) 2689-2696.

[47] T.J. Johnson, Analysis of Dynamic Transmissibility as a Feature for Structural Damage Detection, M.S. Thesis, Purdue University, 2001.

[48] R.L. Brown, D.E. Adams, Equilibrium point damage prognosis models for structural health monitoring, Journal of sound and Vibration, 262(2003) 591-611.

[49] K. Worden, Structural fault detection using a novelty measure, Journal of Sound and Vibration, 201(1997) 85-101.

[50] D. Afolabi, An anti-resonance technique for detecting structural damage, Proceedings of the 5th International Modal Analysis Conference, (1987) 491-495.

[51] K. Worden, G. Manson, D.J. Allman, Experimental validation of a structural health monitoring methodology, Part I: novelty detection on a laboratory structure, Journal of Sound and Vibration,

259(2003) 323-343.

[52] G. Manson, K. Worden, D.J. Allman, Experimental validation of a structural health monitoring methodology, Part II: novelty detection on a GNAT aircraft, Journal of Sound and Vibration, 259(2003) 345-363.

[53] G. Manson, K. Worden, D.J. Allman, Experimental validation of a structural health monitoring methodology. Part III: damage location on an aircraft wing. Journal of Sound and Vibration 259 (2003) 365–385.

[54] H. R. Kess, D.E. Adams, Investigation of operational and environmental variability effects on damage detection algorithms in a woven composite plate, Mechanical Systems and Signal Processing, 21(2007) 2394-2405.

[55] G. Plessis, B. Lallemand, T. Tison, P. Level, Fuzzy modal parameters, Journal of Sound and vibration (2000) 233(5), 797-812

[56] S. Adhikari, M.I. Friswell, K. Lonkar, A. Sarkar, Experimental case studies for uncertainty quantification in structural dynamics, Probabilistic Engineering Mechanics 24 (2009) 473-492

[57] K. Worden, G. Manson, T.M. Lord, M.I. Friswell, Some observations on uncertainty propagation through a simple nonlinear system, Journal of Sound and Vibration 288 (2005) 601-621

[58] B.R. Mace, K. Worden, G. Manson, Uncertainty in structural dynamics, Journal of Sound and Vibration 288 (2005) 423-429

[59] T.L. Lew, A.B. Spencer, F. Scarpa, K. Worden, A. Rutherford, F. Hemez, Identification of response surface models using genetic programming, Mechanical Systems and Signal Processing 20 (2006) 1819-1831

[60] H.-R. Bae, R.V. Grandhi, R.A. Canfield, An approximation approach for uncertainty quantification using evidence theory, Reliability Engineering and System Safety 86 (2004) 215-225

[61] T.E. Fricker, J.E. Oakley, N.D. Sims, K. Worden, Probabilistic uncertainty analysis of an FRF of a structure using Gaussian process emulator, Mechanical Systems and Signal Processing 25 (2011) 2962-2975

[62] A. Manan, J.E.Cooper, Prediction of uncertain frequency response function bounds using polynomial chaos expansion, Journal of Sound and Vibration 329 (2010) 3348-3358

[63] G. Manson, K. Worden, Frequency response functions for uncertain nonlinear systems, Materials Science Forum Vols. 440-441 (2003) pp 37-44

[64] J.R. Fonseca, M.I. Friswell, J.E. Mottershead, A.W. Lees, Uncertainty identification by the maximum likelihood method, Journal of Sound and Vibration 288 (2005) 587-599

[65] D.L. Wei, Z.S. Cui, J. Chen, Uncertainty quantification using polynomial chaos expansion with points of monomial cubature rules, Computers and Structures 86 (2008) 2102-2108

[66] J. Li, J.-B. Chen, The probability density evolution method for dynamic response analysis of non-linear stochastic structures, International Journal for Numerical Methods in Engineering 65 (2006) 882-903

[67] L. Cui, Z. Lu, Q. Wang, Parametric sensitivity analysis of the importance measure, Mechanical Systems and Signal Processing, 28 (2012) 482-491

[68] S.G. Pierce, K. Worden, A. Bezazi, Uncertainty analysis of a neural network used for fatigue lifetime prediction, Mechanical Systems and Signal Processing 22 (2008) 1395-1411

[69] T. Zhou, Model uncertainty in frequency response based system identification, Systems & Control Letters 32 (1997) 121-133

[70] Z. Mao, M.D. Todd, A model for quantifying uncertainty in the estimation of noise-contaminated measurements of transmissibility, Mechanical Systems and Signal Processing 28 (2012) 470-481

[71] T.J. Johnson, D.E. Adams, Transmissibility as a differential indicator of structural damage, Trans. ASME: J. Vibr. Acoust. 124 (2002) 634-641.

[72] Scott W. Doebling, François M. Hemez, Overview of Uncertainty Assessment for Structural Health Monitoring Proceedings of the 3rd International Workshop on Structural Health Monitoring, September 17-19, 2001, Stanford University, Stanford, California

[73] Rik Pintelon and Mei Hong, Asymptotic Uncertainty of Transfer-Function, Estimates Using Nonparametric Noise Models, IEEE TRANSACTIONS ON INSTRUMENTATION AND MEASUREMENT, VOL. 56, NO. 6, DECEMBER 2007 2599,

[74] Douwe K. de Vries, Paul M.J. van den Hof, Quantification of uncertainty in transfer function estimation: a mixed probabilistic-worst-case approach, Automatica, Volume 31, Issue 4, April 1995, Pages 543-557, ISSN 0005-1098, 10.1016/0005-1098(95)98483-M.

[75] Johan Karlsson, Tryphon T. Georgiou, Uncertainty Bounds for Spectral Estimation, arXiv:1201.4469v1 [cs.SY] 2012

[76] M.W. Trethewey, Separation of time variant vibration sources by short time coherent output power, Mechanical Systems and Signal Processing 25 (2011) 644-656

[77] N.R. Goodman, Measurement of Matrix Frequency Response Functions and Multiple

Coherence Functions, Measurement Analysis Corp., Tech. Report. AFFDL-TR-65-56, June 1965.

[78] N. R. Goodman, Statistical analysis based on a certain multivariate complex Gaussian distribution (an introduction), the Annals of Mathematical Statistics, 34(1963) 152-177.

[79] J.S. Bendat, A.G. Piersol, Random Data: Analysis and Measurement Procedures (2nd Edition), John Wiley & Sons, New York, 1986

[80] J. S. Bendat, A.G. Piersol, Engineering Applications of Correlation and Spectral Analysis, 2nd Edition, John Wiley & Sons, New York, 1993.

[81] J. S. Bendat, Statistical errors in measurement of coherence function and input/output quantities, Journal of Sound and Vibration, 59(1978) 405-421.

[82] T. Schultz, M. Sheplak, L.N. Cattafesta III, Application of multivariate uncertainty analysis to frequency response function estimates, Journal of Sound and Vibration, 305(2007) 116-133.

[83] Michael W. Vanik, A Bayesian probabilistic approach to structural health monitoring. PhD thesis, Earthquake Engineering Research Laboratory, California Institute of Technology(1997)

[84] M. W. Vanik, J. L. Beck and S. K. Au, Bayesian Probabilistic Approach to Structural Health Monitoring, Journal of Engineering Mechanics, Vol. 126, No. 7, July 2000, pp. 738-745

[85] Raphael T. Haftka, Fuh-Gwo Yuan and Nam-Ho Kim, Probability Based Integration of Structural Health Monitoring into the aging aircraft sustainment program, AFOSR report, GRANT NUMBER FA9550-07-1-0018

[86] You Ling, Sankaran Mahadevan, Integration of structural health monitoring and fatigue damage prognosis, Mechanical Systems and Signal Processing, Volume 28, April 2012, Pages 89-104.

[87] S.S. Kulkarni and J.D. Achenbach, Structural Health Monitoring and Damage Prognosis in Fatigue, Structural Health Monitoring March 2008 7: 37-49

[88] A Probabilistic Approach to Damage Localization in Structural Health Monitoring, master thesis of North Carolina State University by Hussein Said Harb, 2005

[89] M. Bassevillea, L. Mevel, M. Goursat, Statistical model-based damage detection and localization: subspace-based residuals and damage-to-noise sensitivity ratios, Journal of Sound and Vibration 275 (2004) 769 – 794

[90] Jenkel, C.; Graf, W.; Pannier, S.; Sickert, J.-U.: Structural health monitoring under consideration of uncertain data. In: 7. LS-DYNA Forum 2008, Bamberg. Kap. F-I, pp. 1-10

[91] S. Sankararaman, S. Mahadevan. Bayesian methodology for diagnosis uncertainty quantification

and health monitoring. Structural Control and Health Monitoring, 1 JUL 2011

[92] P.D. Welch, The use of Fast Fourier Transform for the estimation of power spectra: a method based on time averaging over short, modified periodograms, IEEE Trans. Audio Electroacoustics, 15(1967) 70-73

[93] N. L. Johnson, S. Kotz, Distributions in Statistics - Continuous Univariate Distributions, Vol. 2, John Wiley & Sons, New York, 1970

[94] M. Hagedorn, P.J. Smith, P.J. Bones, R.P. Millane, D. Pairman, A trivariate chi-squared distribution derived from the complex Wishart distribution, Journal of Multivariate analysis, 97(2006) 655-674

[95] E.C. Fieller, The distribution of the index in a normal bivariate population, Biometrika, 24(3-4) (1932): 428-440

[96] Steven M. Kay, Fundamentals of Statistical Signal Processing, Vol II - Detection Theory, Prentice Hall, 1998

[97] M.R. Spiegel, J.J. Schiller, R.A. Srinivasan, Probability and Statistics, 3rd edition, McGraw-Hill Companies Inc., 2009